TUNNEL MOS HETEROSTRUCTURE FIELD EFFECT TRANSISTOR FOR RF

SWITCHING APPLICATIONS

A Dissertation

by

IMAN REZANEZHAD GATABI

Submitted to the Office of Graduate Studies of
Texas A&M University
in partial fulfillment of the requirements for the degree of

DOCTOR OF PHILOSOPHY

~~Approved by:~~

Chair of Committee,   Harlan Rusty Harris
Committee Members,   Chin Bing Su
                      Gregory H. Huff
                      Sreeram Vaddiraju
Head of Department,   Chanan Singh

~~May~~August 2013

Major Subject: Electrical Engineering

Copyright 2013 Iman Rezanezhad Gatabi

ABSTRACT

GaN RF switches are widely used in today's communication systems. With digital communications getting more and more popular nowadays, the need for improving the performance of involved RF switches is inevitable. Designing low ON-state resistance GaN switches are exceedingly important to improve the switch insertion loss, isolation and power loss. Moreover, considerations need to be taken into account to improve the switching speed of the involved GaN HEMTs.

In this dissertation, a new GaN HEMT structure called "Tunnel MOS Heterostructure FET (TMOSHFET)" is introduced which has lower ON-state resistance and faster switching speed compared to conventional AlGaN/GaN HEMTs. In the switch ON process, the channel of this device is charged up by electron tunneling from a layer underneath the channel as opposed to typical AlGaN/GaN HEMTs in which electron injection from the source is charging up the channel. The tunneling nature of this process together with the shorter travel distance of electrons in TMOSHFET provide for a faster switching speed.

In order to understand the tunneling mechanisms in TMOSHFET, the fabrication of AlGaN/GaN Schottky Barrier Diodes (SBDs) with various AlGaN thicknesses is demonstrated on Si (111) substrate. The impacts of SF_6 dry etching on the trap density and trap state energy of AlGaN surface are investigated using the G_P/ω- ω method. Various tunneling mechanisms at different biases are then characterized in samples and compared with each other.

To improve the source and drain resistances in TMOSHFET, a model is generated to optimize the 2DEG density and electric field in AlGaN/GaN heterostructure based on Al mole fraction, AlGaN thickness and the thickness of SiN passivation layer and it is experimentally verified by non-contact Hall 2DEG density measurements. The spontaneous and piezoelectric polarizations together with strain relaxation have been implemented into the model, taking into account the annealing effects. From the experimental data on obtained parameters, the operation and device parameterization of the TMOSHFET is outlined and design considerations to improve the device R_{ON}-V_{BR} figure of merit are discussed.

DEDICATION

To my parents ...

Your love and support will always be remembered.

ACKNOWLEDGEMENTS

I would like to extend my sincere appreciation to my advisor, Dr. Harris, for all of his contributions of time and ideas. He offered me a lot of valuable guidance and sufficient freedom of surfing for research. Without his support and help throughout my studies at Texas A&M, it would have been impossible for me to accomplish this project and complete my dissertation. During these years, I have learned a lot from him and I am very grateful that he trusted me and provided me the opportunity of joining his group.

I want to express my gratitude to my committee members, Dr. Vaddiraju, Dr. Huff and Dr. Su, for their guidance and support throughout the course of this research. They have offered me insightful advices and valuable guidance during my research. Special thanks go to Dr. Edwin L. Piner of Texas State University and Dr. Mark Holtz of Texas Tech University for their significant contributions and helps.

Thanks also go to my friends and colleagues and the department faculty and staff for making my time at Texas A&M University a great experience. There are several people that could be mentioned for their assistance in my work and in their friendship. I want to thank Jung Hwan Woo, Derek. W. Johnson, Mary R. Coan, Jae Woo Suh, Feyza Berber and Michael Babb for their helps and friendship during these years.

Finally, I would like to thank my parents from the bottom of my heart for their encouragements throughout my life.

NOMENCLATURE

q	Magnitude of electron charge
E_g	Bandgap energy
n_i	Intrinsic electron density
ε_r	Relative electric permittivity
ε_0	Electric permittivity of vacuum
μ_n	Mobility of electrons
E_c	Critical breakdown electric field
v_{sat}	Saturation velocity of electrons
Θ_K	Thermal conductivity
R_{ON}	ON-state resistance
C_{OFF}	OFF-state capacitance
V_{BR}	Breakdown voltage
E_{SP}	Spontaneous electric field
E_{PE}	Piezoelectric electric field
E_P	Total polarization electric field
P_{SP}	Spontaneous polarization
P_{PE}	Piezoelectric polarization
P_P	Total polarization
I_D	Drain current
V_D	Drain voltage

V_G	Gate voltage
G_P	Parallel conductance
ω	Radial frequency
ε_j	Components of the strain field
m_e	Electron mass
V_{th}	Threshold voltage
R_C	Contact resistance
D_T	Trap density
τ_T	Trap state time constant
σ_T	Trap state's capture cross-section
v_t	Carriers' average thermal velocity
N_c	Density of states in the conduction band
E_T	Trap state energy
T	Temperature
h	Plank constant
J_{TAT}	Trap assisted tunneling current density
m_{AlGaN}	Electron mass in AlGaN
k	Boltzmann constant
n	Diode ideality factor
J_{PF}	Poole-Frenkle emission current density
J_{FN}	Fowler-Nordheim tunneling current density
m^*	Effective mass of electron

A^* Effective Richardson constant

TABLE OF CONTENTS

Page

LIST OF FIGURES

Formatted: Indent: Left: 0", Hanging: 0.8"

xii

xiii

xiv

Formatted: Indent: Hanging: 0.8"

xvi

LIST OF TABLES

CHAPTER I

INTRODUCTION

Electronic switches play a crucial role in today's power electronics and communication industries. High speed semiconductor devices are key components in communication systems as they can handle analog and digital signals at high frequencies. In applications such as satellite transmitters with on board switching systems, reconfigurable phase shifter in phase array antennas and transmitting stations for cellular phones, there is a high demand for devices that can deliver high power in GHz range frequencies.

From conventional silicon-based switches to today's modern wide bandgap transistors, the search is ongoing to provide devices that are faster and more energy-efficient. The frequency range and power handling capability of silicon based switching transistors are limited due to the material-dependent parameters such as mobility, saturation velocity, critical breakdown electric field and inversion layer charge density. Therefore, new materials and device configurations need to be implemented to meet demands for high frequency and high power switching applications.

Wide bandgap semiconductors and particularly Gallium Nitride (GaN) are gaining a lot of attention for high speed and high power switching applications due to their large critical breakdown electric fields, high mobility and high saturated electron velocity [1, 2]. GaN has a relatively large saturation velocity and peak electron velocity,

wide bandgap and better thermal stability compared to Silicon and Gallium Arsenide [3]. Table 1 compares some material parameters of GaN with other semiconductors [4].

Table 1. Physical properties of different semiconductors

Material	Si	4H-SiC	GaN	AlN	Diamond
E_g (eV)	1.1	3.26	3.39	6.1	5.45
n_i (cm^{-3})	1.5e10	8.2e-9	1.9e-10	~10^{-31}	1.6e-27
ε_r	11.8	10	9	8.4	5.5
μ_n (cm^2/Vs)	1350	700	900	1100	1900
E_c (10^6 V/cm)	0.3	3	3.3	11.7	5.6
v_{sat} (10^7 cm/s)	1	2	2.5	1.8	2.7
Θ_K (W/cmK)	1.5	4.5	1.3	2.5	20

As indicated in this table, the critical breakdown electric field (E_c) of GaN is more than 10 times larger than that of Si, providing for operation at large voltages. Moreover, GaN has an electron saturation velocity (v_{sat}) which is 2.5 times larger than that of Si which provides for a large current handling capability. The large critical breakdown electric field combined with a high saturation velocity makes GaN-based devices suitable for high power and high frequency switching applications.

In addition to higher electron saturation velocity and larger critical breakdown electric field, electrons in GaN based High Electron Mobility Transistors (HEMTs) form a Two Dimensional Electron Gas (2DEG), the density of which can exceed 10^{13} cm^{-2}.

2

This high density of electrons in the channel can provide for a very large maximum achievable ON-state current in GaN HEMTs. Moreover, the undoped electron pass in GaN HEMTs results in less impurity scattering and a higher mobility which further increases the maximum ON-state current and switching frequency of the device.

The need for improving the characterictics of GaN switches

RF switches are widely used in modern communication systems. Further advancement in digital communication systems is impossible without design and implementation of high-performance RF switches. Figure 1 illustrates the configuration of a Single-Pole Single-Through (SPST) RF switch and its equivalent circuits when the switch is open and closed.
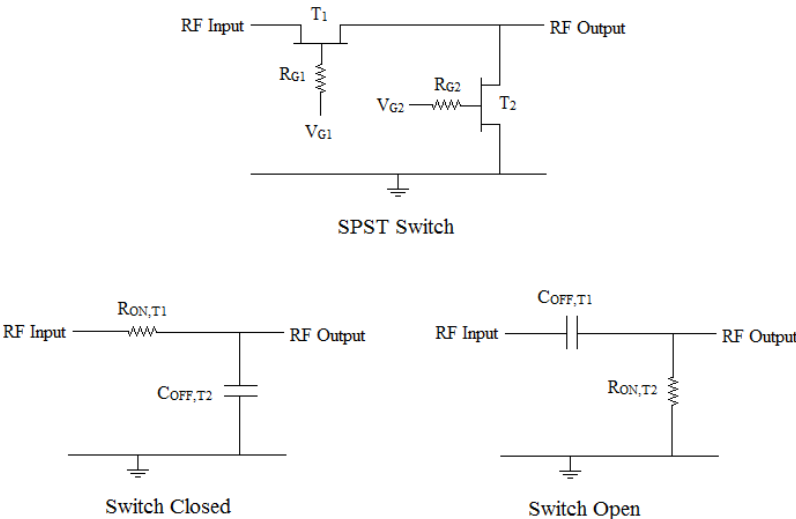
Figure 1. The configuration of a Single-Pole Single-Through (SPST) RF switch and its equivalent circuits when the switch is open and closed.

3

When the transistor T_1 is ON and T_2 is OFF, the path between the input and output is connected and the switch is closed. On the other hand, when T_1 is OFF and T_2 is ON, the output is grounded and the switch is open. Due to R_{ON} of T_2 and C_{OFF} of T_1, some portion of the input signal appears at the output even when T_1 is OFF. The magnitude of the input signal that gets coupled across an open circuit is called isolation. The value of isolation in electronic switches should be larger than 20 dB in order for the switch to be suitable for implementation in communication systems. The isolation is improved by decreasing the ON-state resistance of T_2. A bad isolation can cause cross-talk where the signal of an unwanted input appears at the output of a switch bank (Figure 2).
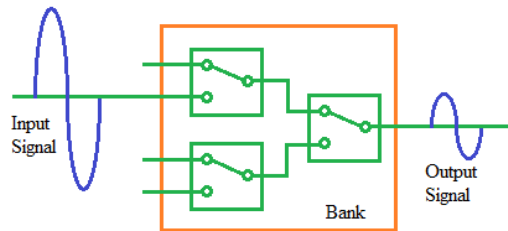
Figure 2. Cross-talk in a switch bank.

When the T_1 is ON and T_2 is OFF, a portion of the input signal is grounded due to the R_{ON} of T_1 and C_{OFF} of T_2. The loss of signal power from input to output in an electric switch is called insertion loss. The value of insertion loss for an RF switch should be smaller than 0.5 dB for implementation in communication systems. This can be achieved by decreasing the R_{ON} of T_1. Therefore, implementing lower ON-state resistance transistors in RF switches improves both isolation and insertion loss.

4

In addition to improving the insertion loss and isolation, decreasing R_{ON} is desired to reduce the power loss of switches. This is critically important both in power electronics and RF applications as low ON-state resistance switches provide energy efficient circuits. In an AlGaN/GaN HEMT, the ON-state resistance can be reduced by decreasing the gate to drain length. However, decreasing the gate to drain distance also reduces the breakdown voltage (V_{BR}) and there is a trade-off between R_{ON} and V_{BR}. Figure 3 illustrates the R_{ON}-V_{BR} relationships of experimentally reported literature data for AlGaN/GaN HEMTs [5-16] and the theoretical limit for GaN-based devices.
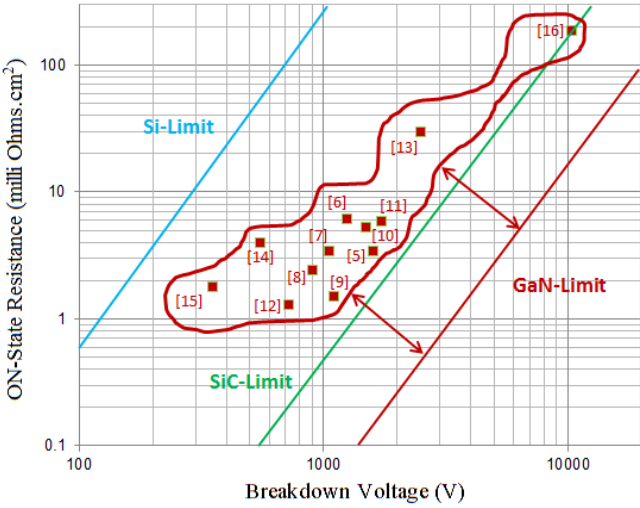
Figure 3. The R_{ON}-V_{BR} relationships of the experimentally reported literature data for AlGaN/GaN HEMTs [5-16] and the introduced theoretical limits for Si, SiC and GaN devices.

As shown in this figure, in order to achieve lower ON-state resistances, the breakdown voltage needs to be sacrificed. Moreover, the reported R_{ON}-V_{BR} values for AlGaN/GaN

5

HEMTs are far away from the introduced GaN limit line. Therefore, it is important to optimize the design parameters in order to improve the R_{ON}-V_{BR} Figure of Merit (FOM).

Lower ON-state resistance is also desirable to increase the switching speed of the device. In devices with shorter gate to drain distances, the gate length is the most important factor that defines the switching frequency. However, as the gate to drain length increases, the output voltage swing will be limited due to RC time constant of the drain terminal. Therefore, the device design should be optimized to achieve higher switching frequencies.

Synopsys of this dissertation

In this dissertation, three approaches are discussed to address the previously mentioned issues and achieve a lower ON-state resistance switch:

First, the structure of Tunnel MOS Heterostructure FET (TMOSHFET) is introduced and its performance is simulated using Synopsys-Sentaurus software. The switch ON process in this device is done by tunneling of electrons from a layer underneath the channel as opposed to electron injection from the source into the channel in typical AlGaN/GaN HEMTs. Since the nature of this process is tunneling and electrons are traveling a shorter distance to charge up the channel, the switch ON process will be faster compared to GaN HEMTs with the same gate lengths. Moreover, the charges underneath the gate form two parallel sheets which act like two resistances in parallel with each other, decreasing the overall ON-state resistance.

In order to decrease the source and drain resistances, a model is developed to optimize the 2DEG density in an AlGaN/GaN heterostructure based on AlGaN

6

thickness, Al mole fraction and the thickness of SiN passivation layer. The spontaneous and piezoelectric polarizations together with strain relaxation are taken into account to calculate the 2DEG density and electric fields. The Al mole fraction, AlGaN thickness and passivation layer thickness are calculated to optimize the 2DEG density and electric field. In order to validate the model, SiN films with different thicknesses are grown on AlGaN/GaN heterostructure using Plasma Enhanced Chemical Vapor Deposition (PECVD) method. Then, samples are annealed at different temperatures and the 2DEG density is measured using the non-contact Hall measurement technique. The parameters used in the model are then calibrated using the experimental data.

The R_{ON}-V_{BR} FOM of AlGaN/GaN HEMTs is calculated using the parameters obtained from the first section of the project. The goal of this part is to optimize the design parameters in order to improve the FOM and push the R_{ON}-V_{BR} data closer to the GaN limit line (Figure 3). The density of surface traps density at AlGaN/passivation layer interface and trap state energy are incorporated into simulations as they influence the breakdown voltage and ON-state resistance. The electric field distribution in the device together with I_D-V_D characteristics are simulated for different Al mole fractions and AlGaN thicknesses to find the breakdown voltage and ON-state resistance. The corresponding R_{ON}-V_{BR} characteristics are then generated for different Al mole fractions, AlGaN thicknesses and trap densities at AlGaN/passivation layer interface, allowing for FOM optimization based on these parameters.

Finally, the proposed tunneling process in the TMOSHFET is demonstrated in an AlGaN/GaN heterostructure on Si (111) substrate. Ni/Au Schottky contacts on recess

7

etched AlGaN are fabricated and characterized to prove the existence of tunneling current from underlying GaN into the top AlGaN layer. The implementation of a dry etch recipe for AlGaN recess etch and its effects on the trap density in the AlGaN layer are investigated using the G_P/ω versus ω method. The fabrication process of these Schottky Barrie Diodes (SBDs) with different AlGaN thicknesses is described and the analysis of I-V characteristics to characterize the tunneling currents is discussed.

CHAPTER II

III-NITRIDE HIGH ELECTRON MOBILITY TRANSISTORS

Introduction

In this chapter, III-nitride semiconductors are introduced and their physical properties are outlined. The spontaneous and piezoelectric polarizations together with the strain due to the lattice mismatch between the layers are discussed. The formation of a Two Dimensional Electron Gas (2DEG) at the interface of AlGaN/GaN heteostructure due to the polarization electric fields is described and its properties are compared with electrons in the inversion layer of MOS structures. The structure of an AlGaN/GaN High Electron Mobility Transistor (HEMT) is then introduced and its fabrication process and principle of operation are discussed and compared with that of a MOSFET.

III-nitride semiconductors

III-nitride semiconductors refer to Gallium Nitride (GaN), Aluminum Nitride (AlN), Indium Nitride (InN) and their alloys (InGaN, AlGaN and InAlN). Their crystal lattices comprise bonds between a group III element and nitrogen (group V). So, nitrogen gives an electron to the group III element and as the results, nitrogen is positively charged and the group III element is negatively charged. This generates a built-in electric field in the semiconductor which is called spontaneous electric field. Figure 4 illustrates the GaN crystal lattice.
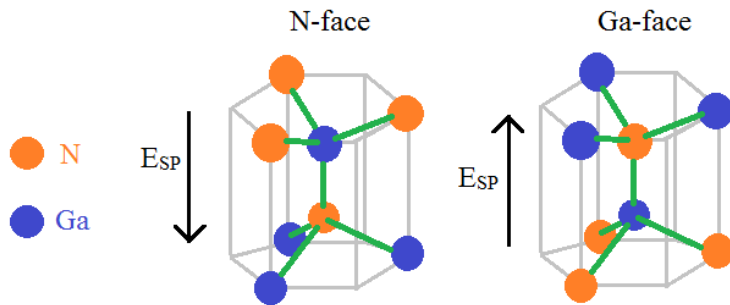
Figure 4. The lattices of N-face and Ga-face gallium nitride.

As shown in this figure, depending on whether the GaN is Ga-faced or N-faced, the direction of the spontaneous electric field will be different. Figure 5 illustrates the bandgaps and lattice constants of III-nitride materials and their alloys [17].
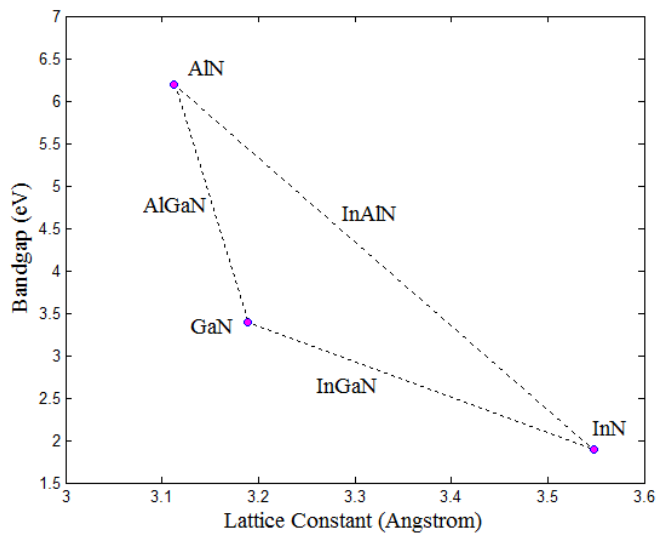
Figure 5. The lattice constants and bandgaps of III-nitride semiconductors and their alloys.

In this figure, it is assumed that the lattice constant and bandgap energy of III-N alloys change linearly with the variation of the mole fraction of group III element. Having a lattice constant of 3.112 Å, AlN is fairly lattice matched with Si (111) and it can be directly grown on that. Since Si is cheap, it can be used as the preferred substrate in applications where substrate leakage is not a significant issue. For higher power applications and in order to decrease substrate leakage, SiC and sapphire substrates may be used. For the case of Si (111) substrate, if there is a need to have a GaN layer (in AlGaN/GaN HEMTs for example), the transition from AlN to GaN is done through the deposition of several AlGaN layers with Al mole fraction decreasing from the bottom to top (Figure 6Figure 6).
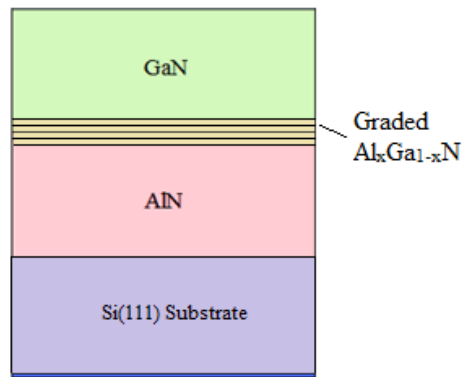
Figure 6. Growth of III-N on Si (111) substrate.

These graded AlGaN layers help relieving the strain caused due to the lattice mismatch between the layers, resulting in a lower dislocations and trap densities in upper films. More details on III-nitride growth on Si (111) substrate are described in reference [18].

AlGaN/GaN heterostructures and two dimensional electron gas

If an AlGaN layer is grown on a Ga-face GaN, it is strained due to the lattice mismatch between two layers and is subjected to piezoelectric polarization. This piezoelectric polarization together with the spontaneous polarization of AlGaN drive the electrons in donor-like surface traps of AlGaN surface toward AlGaN/GaN interface, leaving behind positively-charged empty surface traps at AlGaN surface [19, 20]. The electrons that are driven due to the polarization electric fields are accumulated in the GaN side of AlGaN/GaN interface due to the higher bandgap of AlGaN relative to GaN (Figure 5). The accumulated electrons at AlGaN/GaN interface are called Two Dimensional Electron Gas (2DEG). Figure 7 illustrates the formation of 2DEG in AlGaN/GaN heterostructure together with AlGaN/GaN band diagram.
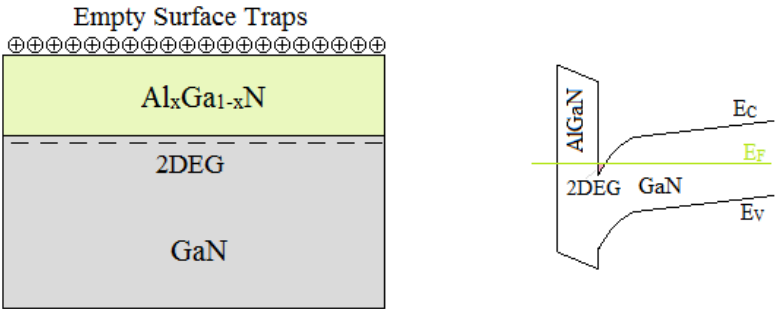
Figure 7. AlGaN/GaN heterosructure and its band diagram.

The density of electrons in 2DEG can exceed 10^{13} cm^{-2} which is much larger than the one in the inversion layer of an n-channel MOSFET. Moreover, since the GaN layer is not doped, electrons in 2DEG experience less impurity scattering which provides for a higher mobility. This high mobility together with the high 2DEG density provides for a large current handling capability in AlGaN/GaN based devices.

AlGaN/GaN High Electron Mobility Transistors (HEMTs)

Figure 8 shows the structure of a typical AlGaN/GaN HEMT which can be fabricated on Si (111), SiC or sapphire substrates.
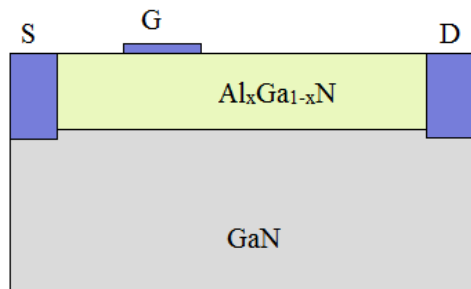
Figure 8. A typical AlGaN/GaN HEMT.

The gate to drain distance is usually longer than gate to source distance to gradually drop the larder drain bias along drain to gate length. The drain electrode can either be Ohmic or Schottky. Different metal stacks like Ti/Al/Ni/Au or Ta/Al/Ta can be used to form Ohmic source and drain contacts. The gate can be a Schottky contact or a typical high-k/metal stack. In a silicon MOSFET, the gate electrode is usually formed first and the source and drain regions are implanted through a gate self-aligned process. However, in

13

AlGaN/GaN HEMTs, source and drain metals can be evaporated before the gate contact metal. After patterning source and drain metals through a lift-off process, they are annealed so that the metal can diffuse into AlGaN and form Ohmic contact with GaN layer. The gate contact can therefore be formed after source and drain annealing.

Figure 9 illustrates the principle of operation of a typical AlGaN/GaN HEMT.
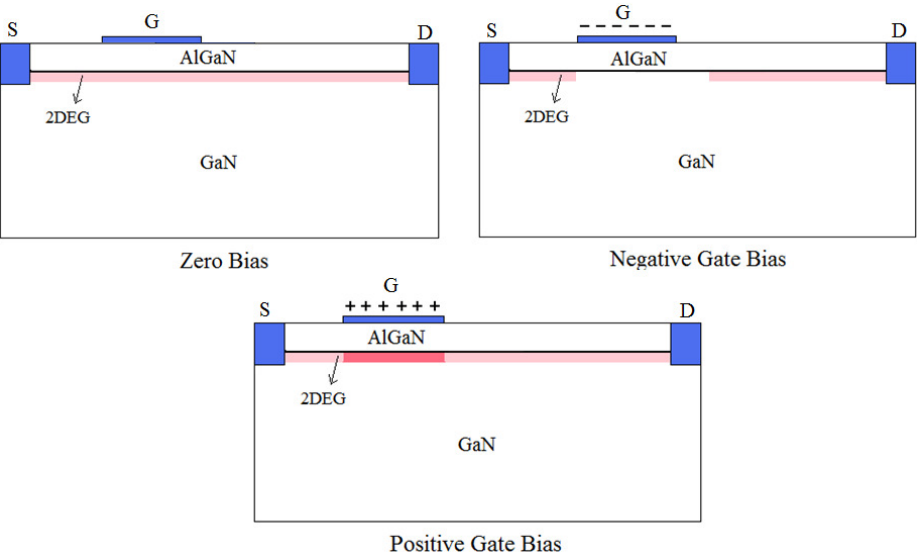
Figure 9. The principle of operation of a typical AlGaN/GaN HEMT.

At the zero gate bias, the 2DEG exists in GaN side of the AlGaN/GaN interface from the source all the way to the drain. Therefore the device is ON at the zero gate bias. Applying a large enough negative gate bias depletes the electrons underneath the gate, providing a discontinuity in 2DEG path from the source to the drain. So, the device switches OFF for large enough negative gate biases. By applying a positive gate bias,

more electrons are accumulated underneath the gate which provides for a lower channel resistance and a higher ON-state current.

Information provided in this chapter was an introduction to III-N semiconductors, AlGaN/GaN heterostructure and HEMTs. More detailed discussions regarding the surface passivation and 2DEG engineering together with improving AlGaN/GaN HEMTs FOM will be provided in chapter IV.

CHAPTER III

TUNNEL MOS HETEROSTRUCTURE FET (TMOSHFET)

Introduction

In this chapter, the configuration of the Tunnel MOS Heterostructure FET (TMOSHFET) is introduced and its performance is simulated using Synopsys-Sentaurus software. The switch ON process in this device through a tunneling mechanism and the way it improves the turn ON delay are discussed. Formation of a double layer 2DEG underneath the gate region is described and its effect on reducing the device R_{ON} is demonstrated using the simulation data. Finally, considerations that should be taken into account to improve the device ON-state resistance and Figure of Merit are described which will be discussed in details in the next chapter.

The structure and principle of operation of TMOSHFET

Figure 10 illustrates the structure of the TMOSHFET.
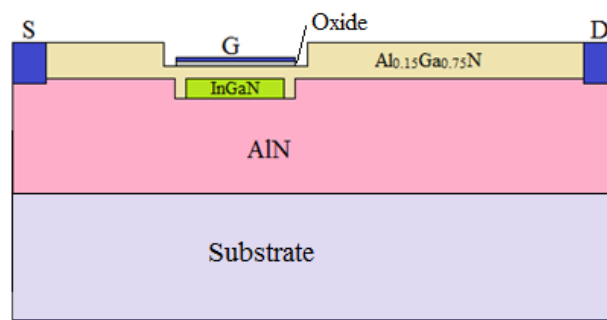
Figure 10. The structure of TMOSHFET.

As shown in this figure, the device comprises of an AlN layer on a substrate which can be Si (111), sapphire or SiC. This AlN is recessed underneath the gate region where the InGaN layer is re-grown to form the charge supplying layer. A top AlGaN layer with low Al mole fraction is grown and etched in the gate region followed by the formation of the gate dielectric and metal contact on top of the gate region. Figure 11 shows the 2DEG charge in the device for zero and positive gate biases.
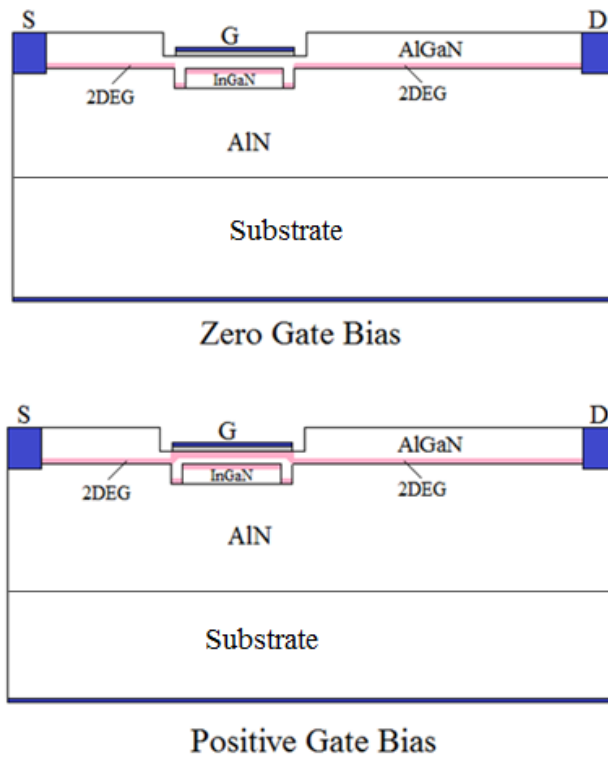
Figure 11. The 2DEG charge in TMOSHFET for zero and positive gate biases.

As shown in this figure, at the zero gate bias and in the gate region, the 2DEG is at the InGaN side of AlGaN/InGaN interface due to the lower bandgap of InGaN relative to AlGaN (Figure 5). In source and drain regions, however, the 2DEG is formed at the AlGaN side of AlGaN/AlN junction because AlGaN's bandgap is smaller than AlN's (Figure 5). This provides a discontinuous electron path between source and drain electrodes and therefore, the device is OFF at zero gate bias.

Since the AlGaN underneath the gate is thin, applying a positive gate bias causes the 2DEG in the InGaN layer to tunnel into the AlGaN layer and charges up the channel. This provides a continuous electron path between source and drain electrodes and the device switches ON. In typical AlGaN/GaN HEMTs (and FETs in general), charging up the channel and the device switch ON process is done by carrier injection from the source into the channel. These injected carriers have to travel the channel length from source all the way to the drain to switch ON the device. Therefore, the turn ON delay is directly proportional to the gate length. However, in TMOSHFET structure, charging up the channel and the turn ON process is done by electron tunneling from the bottom InGaN layer into AlGaN and electrons are traveling a much shorter distance. This, together with the tunneling nature of this process provides for a fast switching speed.

The band diagram and electron density of the TMOSHFET shown in Figure 10 are simulated with the Synopsys-Sentaurus software. Piezoelectric and spontaneous polarizations are implemented into the simulation, taking into account the strain relaxation. Figure 12 illustrates the electron density and conduction band diagram in the gate region at zero gate bias.

18
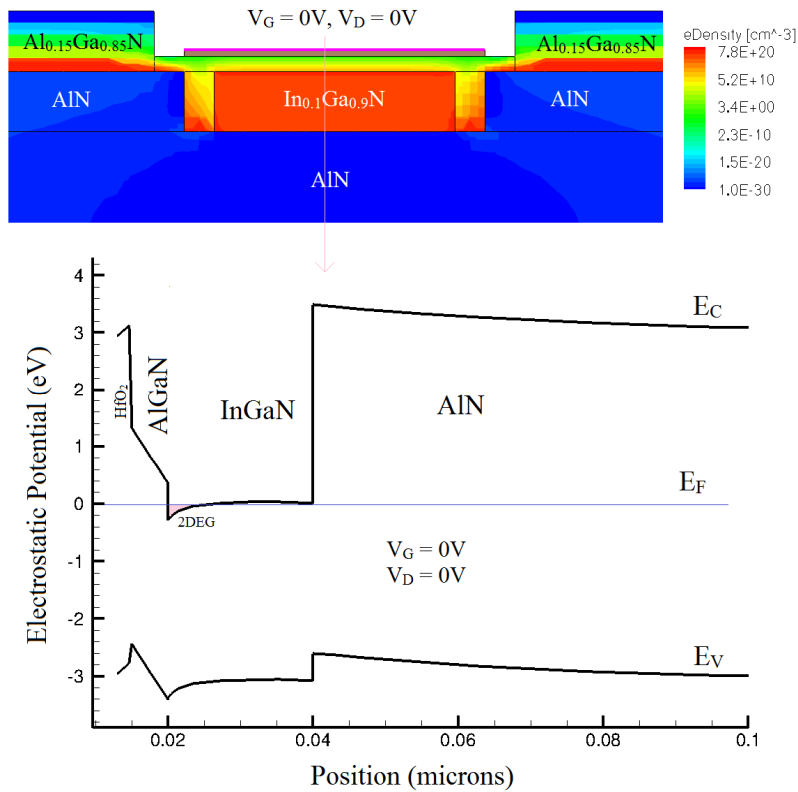
Figure 12. The electron density and band diagram of TMOSHFET at zero gate bias.

Here, the source and drain electrodes are grounded and HfO_2 is used as the gate oxide. As shown in this figure, 2DEG is formed at the InGaN side of AlGaN/InGaN interface at the zero gate bias. In the source and drain regions, however, the 2DEG is formed at the AlGaN side of the AlGaN/AlN interface due to the lower bandgap of AlGaN compared to AlN. The discontinuity in electron path from the source to the drain causes barriers in conduction bands at the gate edges as shown in Figure 13.
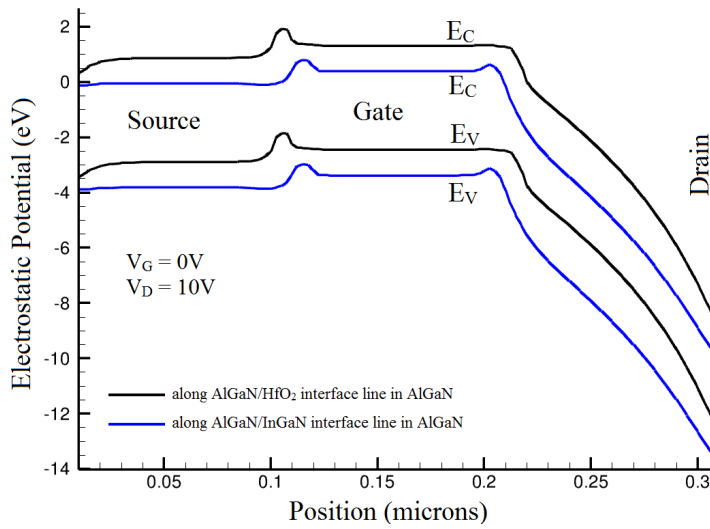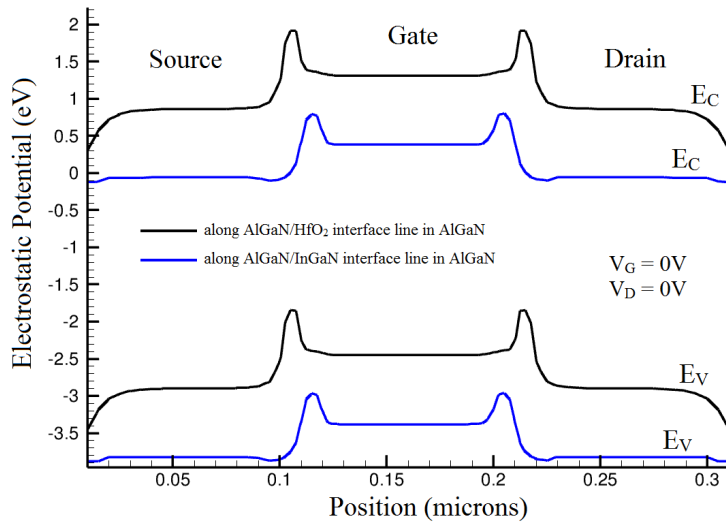
Figure 13. The zero-gate bias band diagrams along AlGaN/HfO$_2$ and AlGaN/InGaN interfaces in AlGaN for zero and positive drain biases.

The barriers in the conduction band prevent electron transport from the channel into the drain region at positive drain voltage, resulting in the partial depletion of the drain region (Figure 14).
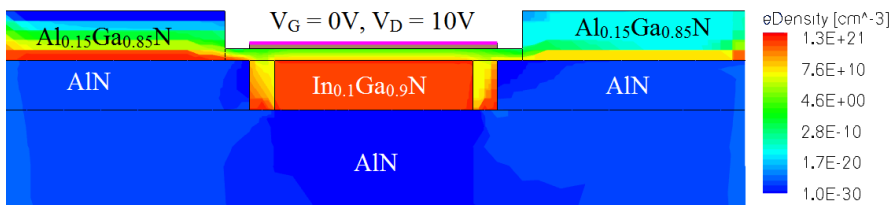
Figure 14. The electron density in TMOSHFET at the zero gate bias and the drain bias of 10V.

Therefore, there is no significant current flow between source and drain terminals at the zero gate bias and the device will be OFF.

Applying a positive gate bias bends the conduction band of the AlGaN layer, making it aligned with that of InGaN. As a result, electrons can tunnel from InGaN into the top AlGaN layer and create a charge sheet at the AlGaN/oxide interface. This completes the electron path between source and drain electrodes and the device switches ON. Figure 15 illustrates the electron density and conduction band diagram in the gate region of TMOSHFET at positive gate bias.
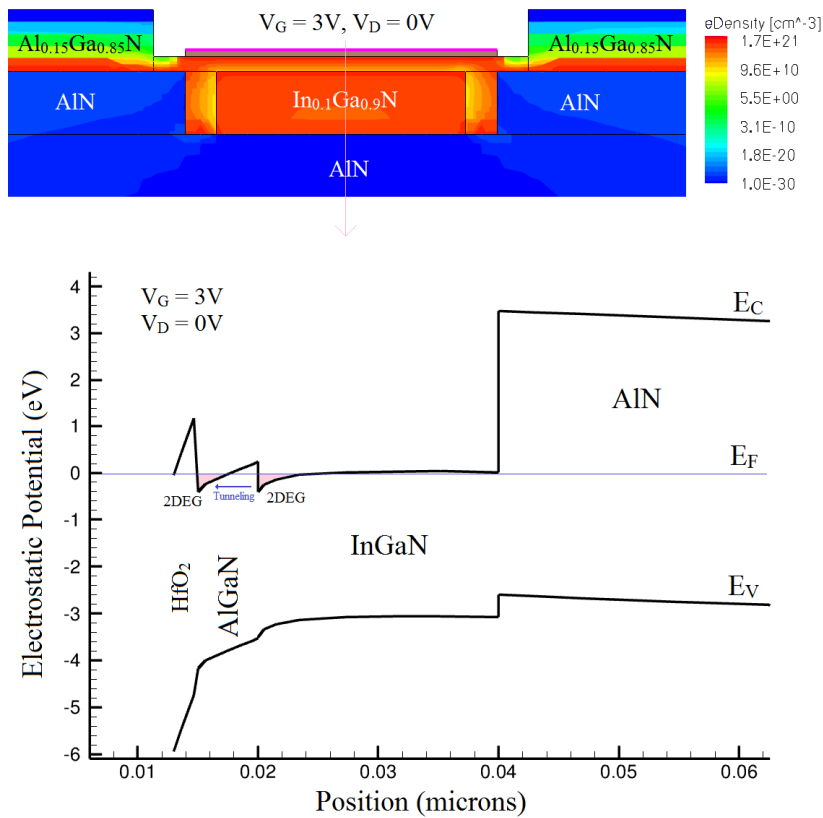
Figure 15. The electron density and band diagram of the TMOSHFET at positive gate bias.

Once the channel is charged up, the barriers in conduction band along the AlGaN (Figure 13) are removed, providing for electron flow from the source to the drain. This is well reflected in Figure 16 where it shows the band diagrams at the positive gate bias for both positive and zero drain biases.
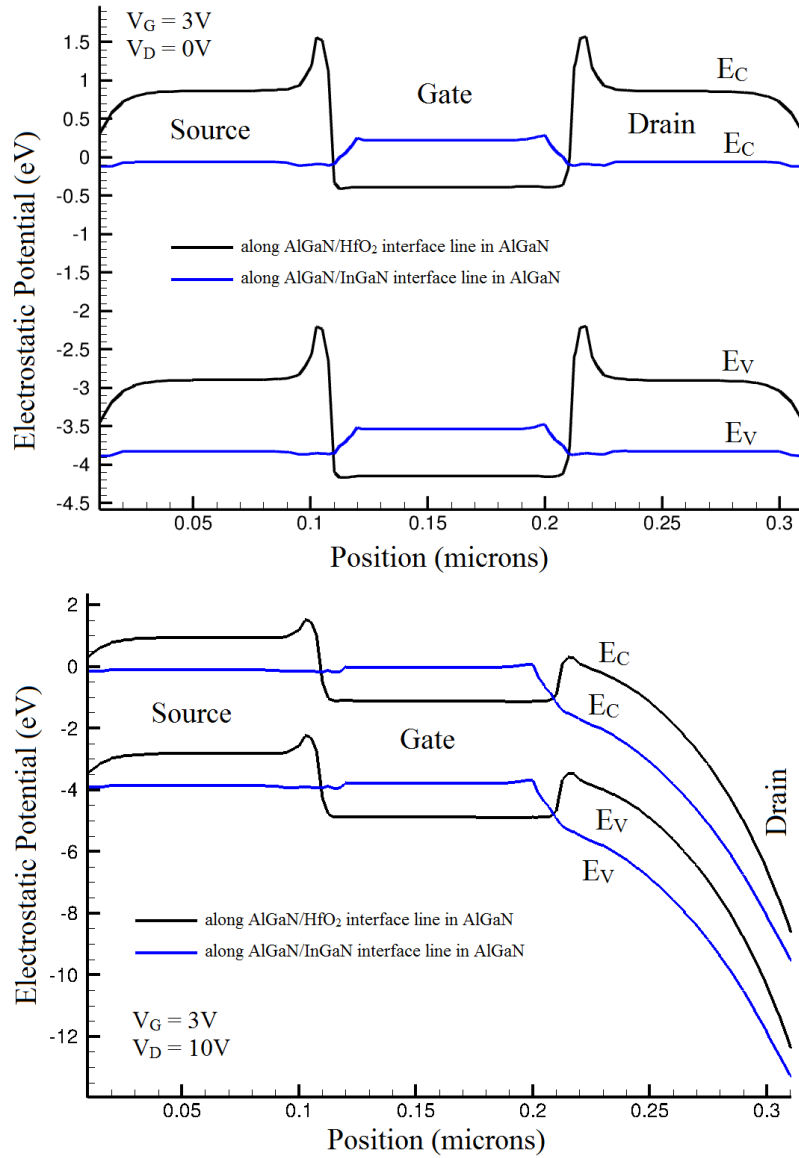
Figure 16. The band diagrams along AlGaN/HfO₂ and AlGaN/InGaN interfaces in AlGaN for zero and positive drain biases and for a gate bias of 3V.

In the turn ON process, electrons are traveling a very short distance (AlGaN thickness) through a tunneling process and this makes the switch ON mechanism much faster than a typical field effect transistor. In typical FETs, charging up the channel and the device switch ON process is done by carrier injection from the source into the channel. These injected carriers should travel the channel length from source all the way to the drain to switch ON the device. Therefore, the turn ON delay is directly proportional to the gate length.

At the ON state, the gate region comprises of two parallel 2DEG charge sheets (Figure 17).
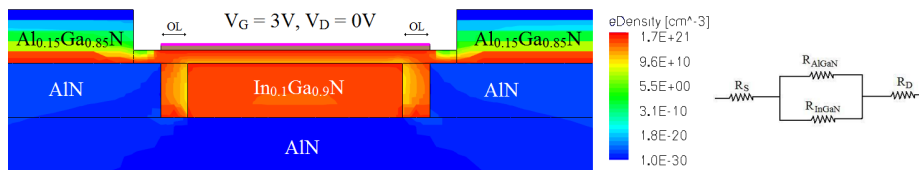
Figure 17. The equivalent source to drain resistance of TMOSHFET.

These parallel sheet charges act like two parallel resistors to reduce the overall channel resistance. In lower voltage applications where the gate length is comparable with the gate to drain length, the total ON-state resistance is reduced due to the existence of these two charge sheets.

However, small positive threshold voltages are reported in GaN HEMTs with recess-etched gates, typical AlGaN/GaN HEMTs have negative threshold voltages. As shown in TMOSHFET structure of Figure 10, the InGaN layer underneath the gate is

embedded between two AlGaN regions along the horizontal axis. These regions cause discontinuities in 2DEG path between source and drain electrodes at zero gate bias which results in a positive threshold voltage. Figure 18 shows the simulated I_D-V_G characteristic of the device.
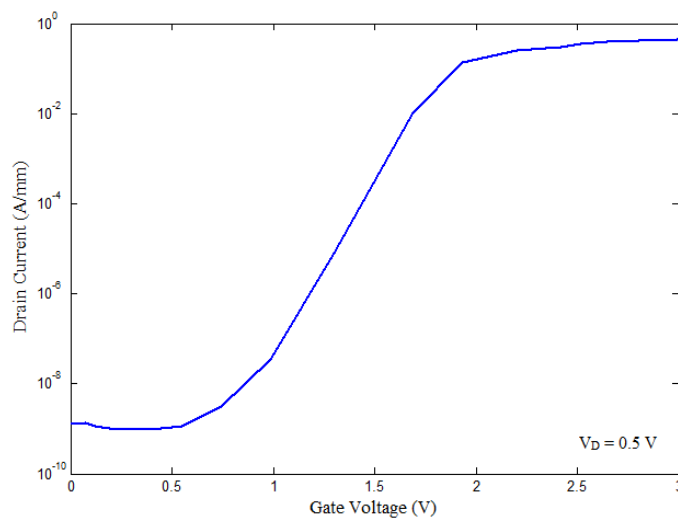
Figure 18. The simulated I_D-V_G of TMOSHFET shown in Figure 10Figure 10.

The "Formatted: Font: Not Bold" is a margin comment/annotation.

The positive threshold voltage is due to the existence of AlGaN regions between InGaN and AlN which make discontinuity in 2DEG pass from source to drain at the zero gate bias.

Figure 19 and Figure 20 illustrate the simulated current gain versus frequency plots of the TMOSHFET shown in Figure 10 for different gate lengths and L_{GD}.
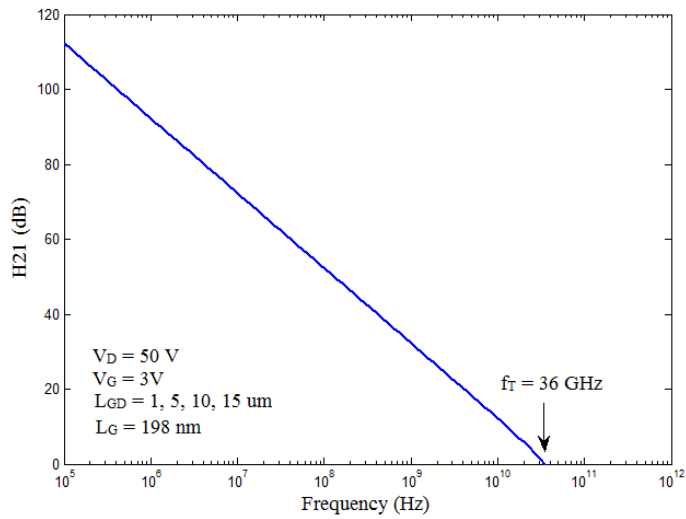
Figure 19. The current gain versus frequency plots of TMOSHFET shown in Figure 10Figure 10 for different gate to drain distances and the extracted cutoff frequency.
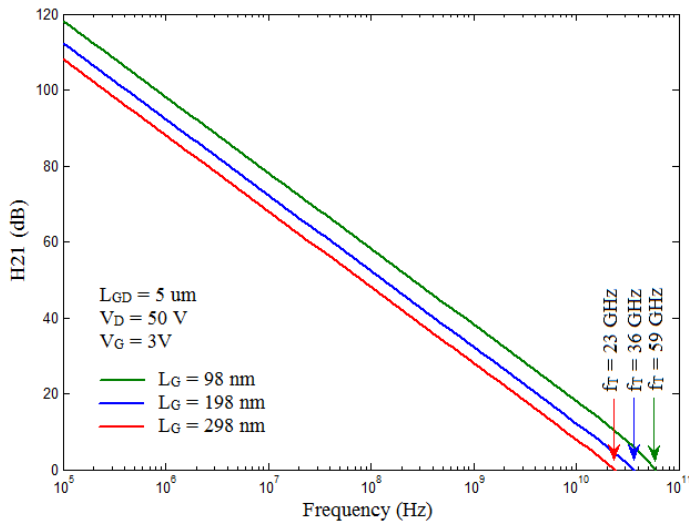
Figure 20. The current gain versus frequency plots of TMOSHFET shown in Figure 10Figure 10 for different gate lengths and the extracted cutoff frequencies.

As shown in these figures, the cutoff frequency increases by decreasing the gate length. However, increasing the gate to drain distance does not have a significant effect on the cutoff frequency. This is due to the fact that the gate capacitance and input conductance are more dominant than the gate to drain capacitance and conductance in defining the cutoff frequency. The cutoff frequency of the device is directly proportional to the modulation efficiency of the gate that quantifies the ability of the gate to quantify the drain current without modulating the fixed charges. A better electron confinement in the channel underneath the gate improves the modulation efficiency. For the case of TMOSHFET, since the electrons that are tunneled from the bottom InGaN layer into the top AlGaN channel are highly confined in the triangular quantum well of AlGaN, the cutoff frequency is improved.

Considerations to fabricate TMOSHFET

Several considerations need to be taken into account to fabricate the TMOSHFET structure. The 2DEG density in source and drain regions need to be optimized based on device parameters to reduce the R_{ON} and improve the device R_{ON}-V_{BR} figure of merit. AlGaN surface passivation should be implemented to make the device more stable in different environmental conditions and improve the device FOM. The 2DEG density optimization and effects of surface passivation on electric field, 2DEG density and FOM will be investigated in the next chapter.

In addition to 2DEG design and surface passivation, low resistance Ohmic contacts are needed in source and drain regions to increase the ON-state current and reduce the overall source to drain resistance. Moreover, a dry etch recipe should be

implemented to recess-etch the gate region to make the AlGaN layer thin enough for increasing the tunneling current. This etch recipe should not increase the trap density at the AlGaN surface significantly to prevent mobility degradation. Demonstration of low-resistance Ohmic contacts to GaN and implementation of an appropriate dry etch recipe and its effects on AlGaN surface traps will be discussed in chapter V.

CHAPTER IV

SURFACE PASSIVATION AND 2DEG ENGINEERING

Introduction

In order to decrease the source and drain resistances in TMOSHFET and achieve an optimized breakdown voltage, the 2DEG density and electric fields in the device should be optimized based on different device parameters and dimensions of different layers. Lower source and drain resistances can be achieved by decreasing the gate to drain length, however, the breakdown voltage would be sacrificed. Therefore, a model should be developed to correlate the 2DEG density, R_{ON} and breakdown voltage of the device to device parameters.

In this chapter, the impacts of AlGaN surface passivation on the 2DEG density, AlGaN polarization electric field and the R_{ON}-V_{BR} FOM of an AlGaN/GaN HEMT are investigated. A model is developed to optimize the 2DEG density based on AlGaN thickness, Al mole fraction and the thickness of SiN passivation layer. The spontaneous and piezoelectric polarizations together with strain relaxation are taken into account to calculate the 2DEG density and electric fields. The Al mole fraction, AlGaN thickness and passivation layer thickness are calculated to optimize the 2DEG density and electric field. In order to validate the model, SiN films with different thicknesses are grown on AlGaN/GaN heterostructure using the Plasma Enhanced Chemical Vapor Deposition (PECVD) method. Then, samples are annealed at different temperatures and the 2DEG density is measured using the non-contact Hall measurement technique. The measured

29

data are then compared with what are predicted by the model. The parameters used in the model are then calibrated using the experimental data.

The R_{ON}-V_{BR} FOM of AlGaN/GaN HEMTs is simulated using the parameters obtained from the introduced model. The density of surface traps at the AlGaN/passivation layer interface and the trap state energy are incorporated into simulations as they influence the breakdown voltage and ON-state resistance. The electric field distribution in the device together with I_D-V_D characteristics are simulated for different Al mole fractions and AlGaN thicknesses to find the breakdown voltage and ON-state resistance. The corresponding R_{ON}-V_{BR} characteristics are then generated for different Al mole fractions, AlGaN thicknesses and trap densities at AlGaN/passivation layer interface, allowing for FOM optimization based on these parameters.

Piezoelectric and spontaneous polarizations

If a thin film is grown on a substrate with different lattice constant, the grown layer is strained and is subject to the piezoelectric polarization [21], which is represented by

$$P_i^p = \sum e_{ij}\varepsilon_j , \tag{1}$$

where ε_j $(j=1,...,6)$ are the components of the strain field and e_{ij} $(i=1,2,3$ & $j=1,...,6)$ are the piezoelectric constants of the strained layer. When AlGaN is epitaxially grown on GaN, the AlGaN will be under biaxial tension and the strain field is written as [21]

$$\hat{\varepsilon} =[\varepsilon_1,\varepsilon_2,\varepsilon_3,0,0,0] , \tag{2}$$

30

where $\varepsilon_1 = \varepsilon_2 = (a_{GaN} - a_{AlGaN}) / a_{AlGaN}$ and $\varepsilon_3 = (c_{GaN} - c_{AlGaN}) / c_{AlGaN} = -2c_{11}.\varepsilon_1 / c_{33}$, in which (a_{GaN}, c_{GaN}) and (a_{AlGaN}, c_{AlGaN}) are the lattice constants of GaN and AlGaN, respectively, and c_{ij} are the elastic stiffness constants of AlGaN. Therefore, the piezoelectric tensor of wurtzite crystals is represented as [22]

$$\hat{e} = \begin{bmatrix} 0 & 0 & 0 & 0 & e_{15} & 0 \\ 0 & 0 & 0 & e_{14} & 0 & 0 \\ e_{31} & e_{31} & e_{33} & 0 & 0 & 0 \end{bmatrix}. \tag{3}$$

From Eqs.1, 2 and 3, the piezoelectric polarization is calculated as

$$P^p = \hat{e}.\hat{\varepsilon} = [0, 0, 2e_{31}\varepsilon_1 + e_{33}\varepsilon_3]. \tag{4}$$

Eq.4 shows that for an AlGaN layer grown on GaN, the piezoelectric induced electric field is along the z-axis. Therefore the z-component of the piezoelectric polarization is written as [23],

$$P_{PE,AlGaN} = P_z^p = 2e_{31}\varepsilon_1 + e_{33}\varepsilon_3 = 2\times\frac{a_{GaN} - a_{AlGaN}}{a_{AlGaN}}(e_{31} - e_{33}\frac{c_{13}}{c_{33}}), \tag{5}$$

where:

$$a_{GaN} = 3.189\times10^{-10}(m) \quad [24] \tag{6}$$

$$a_{Al_xGa_{1-x}N} = x.a_{AlN} + (1-x)a_{GaN} = (-0.077x + 3.189)\times10^{-10}(m) \quad [24] \tag{7}$$

$$e_{33} = 0.73x + 0.73(C/m^2) \quad [25] \tag{8}$$

$$e_{31} = -0.11x - 0.49(C/m^2) \quad [26] \tag{9}$$

$$c_{33} = (-32x + 405)\times10^9(Pa) \quad [27] \tag{10}$$

$$c_{13} = (5x + 103)\times10^9(Pa). \quad [28] \tag{11}$$

31

P_{PE} is a function of aluminum mole fraction (x) of AlGaN as shown by this set of equations. The piezoelectric polarization is also a function of AlGaN thickness, d, due to the model proposed by Blakeslee [29]. Their study shows that for any Al mole fraction of x, strain relaxation, $r(x)$, and reduction in piezoelectric polarization need to be taken into account for AlGaN thicknesses above the critical thickness. In this case, $P_{PE,AlGaN}$ is represented as [23]

$$P_{PE,AlGaN} = 2\times[1-r(x)]\times\frac{a_{GaN}-a_{AlGaN}}{a_{AlGaN}}(e_{31}-e_{33}\frac{c_{13}}{c_{33}}),\qquad(12)$$

in which the strain relaxation is described by

$$r(x) = \frac{a_{AlGaN,strained}-a_{GaN}}{a_{AlGaN,relaxed}-a_{GaN}}.\qquad(13)$$

Here, $a_{AlGaN,strained}$ and $a_{AlGaN,relaxed}$ are the lattice constants of the strained and relaxed AlGaN respectively. The parameter $a_{AlGaN,strained}$ should to be measured experimentally. Due to the study performed by Ambacher et. al. [23], for an AlGaN thickness of 30nm, the degree of relaxation, $r(x)$, increases linearly for Al mole fractions larger than 0.35. Assuming the same rate of change of $r(x)$ in its linear regime for different thicknesses of AlGaN, $r(x)$ is written as

$$r(x) = \begin{cases} 0 & : \quad 0 \le x \le x_1 \\ \min[3.5\times(x-x_1),1] & : \quad x_1 \le x \le 1 \end{cases},\qquad(14)$$

where x_1 is the Al mole fraction corresponding to the critical thickness of AlGaN in Blakeslee model [23, 29]. The values of x_1 for different AlGaN thicknesses could be extracted from figure 4 of reference [23] ($x_1 = 0.7$, 0.47, 0.38, 0.36, and 0.33 for AlGaN critical thicknesses of 10, 20, 30, 40, and 50 nm, respectively).

In addition to piezoelectric polarization, there is spontaneous polarization due to the crystal structure of III-nitride semiconductors as discussed in chapter II. The spontaneous polarization of GaN is -0.029 C/m^2 [23], however, the reported values for AlN spontaneous polarization ranges from -0.036 C/m^2 to -0.081 C/m^2 [30-33]. Assuming a value of -0.058 C/m^2 for AlN spontaneous polarization, the spontaneous polarization of AlGaN is calculated as

$$P_{SP,AlGaN} = x.P_{SP,AlN} + (1-x)P_{SP,GaN} = -0.029x - 0.029(C/m^2).$$ (15)

The mentioned value for AlN spontaneous polarization is selected so that the model best matches the experimental data.

The total macroscopic polarization of AlGaN layer in the absence of external electric field is the sum of spontaneous polarization $P_{SP,AlGaN}$ and the piezoelectric polarization represented by Eq.12.

$$P_{P,AlGaN} = P_{SP,AlGaN} + P_{PE,AlGaN}.$$ (16)

Since GaN layer is usually thick (thicker than 1 um), it is totally relaxed and the piezoelectric polarization of the GaN is zero. So, in GaN layer, there is just the spontaneous polarization which is equal to -0.029 C/m^2 [23].

PECVD SiN passivation and 2DEG density

The as-grown AlGaN/GaN heterostructure has some positive charge on the AlGaN surface from surface states or absorbed ions [34, 35] in response to the negative polarization charge. These positive charges are sensitive to surface treatments and atmospheric conditions [34-37]. The AlGaN surface is typically passivated with silicon nitride to resolve the surface state issues. Moreover, the passivated AlGaN/GaN

33

heterostructure exhibits a relatively higher 2DEG density and lower electric field, which are desirable for high voltage and high power applications.

While PECVD α−SiN passivation of AlGaN/GaN devices has been investigated in the literature [38-40], no clear design and fabrication methodology has been proposed to improve the properties of the AlGaN/GaN heterostructures. Moreover, there has not been a study of the effects of passivated AlGaN/GaN post annealing on 2DEG density. Therefore, detailed analytical and experimental studies need to be performed to optimize the 2DEG density and electric field in passivated AlGaN/GaN heterostructures by choosing appropriate design parameters (α−SiN and AlGaN thicknesses, Al mole fraction and annealing conditions).

As described in chapter 1, the 2DEG is formed at the GaN side of AlGaN/GaN interface due to the piezoelectric and spontaneous polarizations. The 2DEG charge density for the unpassivated case is described by [34, 35, 41]

$$\sigma_s = \frac{P_{SP,AlGaN} + P_{PE,AlGaN} - P_{SP,GaN} - c_{AlGaN} \cdot \psi}{1 + c_{AlGaN} \dfrac{\pi \hbar^2}{q^2 m^*}}, \tag{17}$$

where q is the electron charge, $m^* = 0.22 m_e$ (m_e is electron mass) and $\psi = \phi_b - \Delta E_c$. Here, ϕ_b is the AlGaN surface potential, ΔE_C is the conduction band offset at the AlGaN/GaN interface and c_{AlGaN} is the AlGaN capacitance per unit area:

$$\phi_b = 1.3x + 0.84 (eV) \text{ [42]}, \tag{18}$$

$$\Delta E_C = 1.2x + 0.7x^2 (eV) \text{ [43, 44] and} \tag{19}$$

34

$$c_{AlGaN} = \frac{\varepsilon_0 \varepsilon_{AlGaN}}{d}. \tag{20}$$

In Eq.20, ε_0 is the electric permittivity of vacuum, d is AlGaN thickness and ε_{AlGaN} is the dielectric constant of AlGaN represented by [23]

$$\varepsilon_{AlGaN} = -0.3x + 10.4. \tag{21}$$

Figure 21 illustrates the conduction band diagrams of α−SiN passivated and unpassivated AlGaN/GaN heterostructures [34, 35, 41]. (© 2013 IEEE).
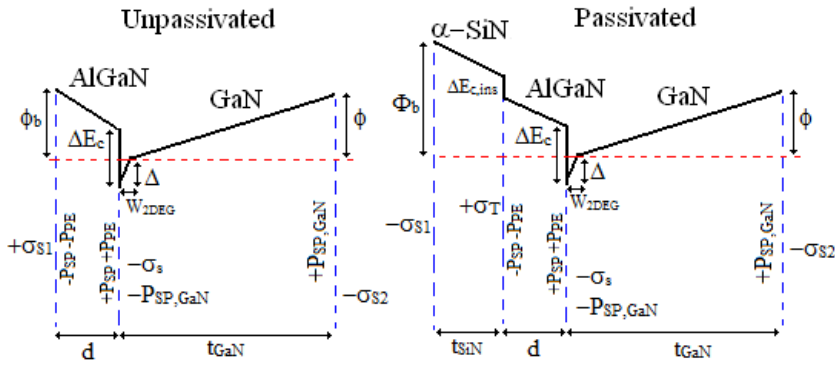
Figure 21. The conduction band diagrams of α−SiN passivated and unpassivated AlGaN/GaN heterostructures.

It has been demonstrated that AlGaN surface passivation results in an increase in 2DEG density. If we assume α-Si_xN_y as the passivating dielectric, the 2DEG charge density is described by [34, 35, 41] (© 2013 IEEE)

$$\sigma_{s,passivated} = \frac{P_{SP,AlGaN} + P_{PE,AlGaN} - P_{SP,GaN} - c_B \cdot \Psi_p}{1 + c_B \dfrac{\pi \hbar^2}{q^2 m^*}}, \tag{22}$$

35

in which c_B is the series combination of AlGaN and α-Si$_x$N$_y$ capacitances and $\Psi_p = \Phi_b -$ $\Delta E_c - \Delta E_{c,ins}$. Here, $\Delta E_{c,ins}$ is the conduction band offset at AlGaN/α-Si$_x$N$_y$ interface and Φ_b is the α-Si$_x$N$_y$ surface potential (Figure 21). Therefore,

$$\frac{1}{c_B} = \frac{1}{c_{AlGaN}} + \frac{1}{c_{SiN}} = \frac{d}{\varepsilon_0 \varepsilon_{AlGaN}} + \frac{t_{SiN}}{\varepsilon_0 \varepsilon_{SiN}}, \qquad (23)$$

where t_{SiN} is the thickness of the α-Si$_x$N$_y$ layer. In Eqs.17 and 22, to reach a more accurate calculation, the strain relaxation was taken into account to determine the piezoelectric polarization of AlGaN. Therefore, the 2DEG densities with and without surface passivation are calculated versus Al mole fraction for different AlGaN thicknesses (Figure 22) [41] (© 2013 IEEE).
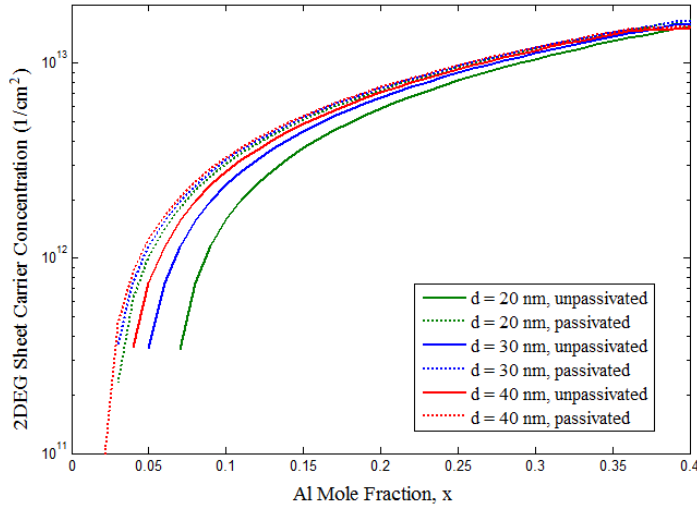
Figure 22. The 2DEG density at AlGaN/GaN interface versus Al mole fractions (*x*) for different AlGaN thicknesses, *d*. Dashed lines: With 30 nm α−SiN surface passivation. Solid lines: Without surface passivation.

36

It should be noted that for Al mole fractions larger than *x = 0.22*, the 2DEG density is at or above 10^{13} cm^{-2}. The 2DEG density is also increased by increasing the AlGaN thickness and it is improved significantly by surface passivation. While large Al mole fractions are desirable to reach higher 2DEG densities, growing crack-free AlGaN films with very large Al mole fractions on GaN is not feasible from the fabrication standpoint [41] (© 2013 IEEE).

Electric field calculations in AlGaN/GaN heterostructures

In addition to achieving a higher 2DEG density, it is preferable to design the AlGaN/GaN heterostructures with a lower internal electric field in order to improve the breakdown voltage. For the as grown case, the electric field in AlGaN ($E_{AlGaN,unpassivated}$) is equal to the total band bending of AlGaN divided by AlGaN thickness. Therefore,

$$E_{AlGaN,unpassivated} = \frac{\phi_b + \Delta - \Delta E_C}{d}, \tag{24}$$

where ϕ_b and ΔE_C are represented by Eqs.18 and 19 respectively and Δ is calculated as [34, 35, 41] (© 2013 IEEE)

$$\Delta = \frac{\sigma_s \pi \hbar^2}{q^2 m^*}, \tag{25}$$

To calculate the electric field of passivated AlGaN, Gauss' law is applied at the AlGaN/GaN interface :

$$\begin{aligned} \varepsilon_0 \varepsilon_{GaN} \cdot E_{SP,GaN} + \varepsilon_0 \varepsilon_{AlGaN} \cdot E_{AlGaN,passivated} = \\ P_{SP,AlGaN} + P_{PE,AlGaN} - P_{SP,GaN} - \sigma_{s,passivated} \end{aligned}, \tag{26}$$

37

where $E_{SP,GaN}$ is the spontaneous polarization induced electric field in the GaN side of AlGaN/GaN interface. $E_{SP,GaN}$ is approximately equal to Δ / W_{2DEG} where W_{2DEG} is the effective width of the 2DEG which is a function of the 2DEG charge density [45]. Therefore, the total polarization electric fields in the AlGaN layer with and without surface passivation are calculated through Eqs. 24 and 26 (Figure 23) [41] (© 2013 IEEE).
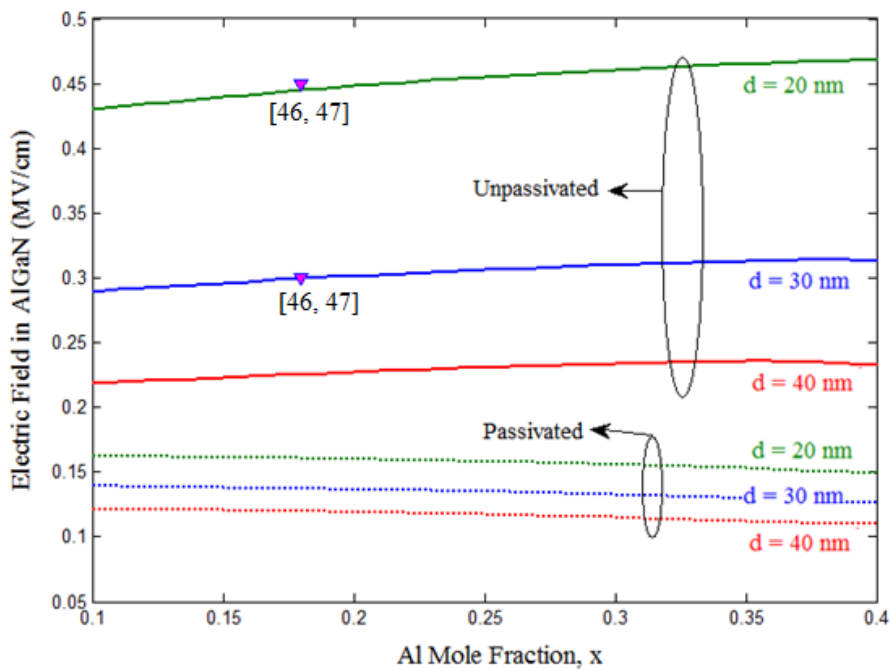
Figure 23. The total polarization electric fields in $Al_xGa_{1-x}N$ layer grown on GaN versus aluminum mole fractions (x) for different AlGaN thicknesses, d. Dashed lines: With 30 nm α-Si_xN_y surface passivation. Solid lines: Without surface passivation. The experimentally measured literature data are included as reference.

The surface passivation reduces the electric field significantly. Moreover, the electric field is increased by decreasing the AlGaN thickness in both passivated and unpassivated cases. The calculated electric fields for unpassivated structures are consistent with the most recent experimentally measured data [46, 47].

Figure 24 illustrates the effects of the α–SiN thickness on electric field of AlGaN layer for different Al mole fractions and AlGaN thicknesses [41] (© 2013 IEEE).
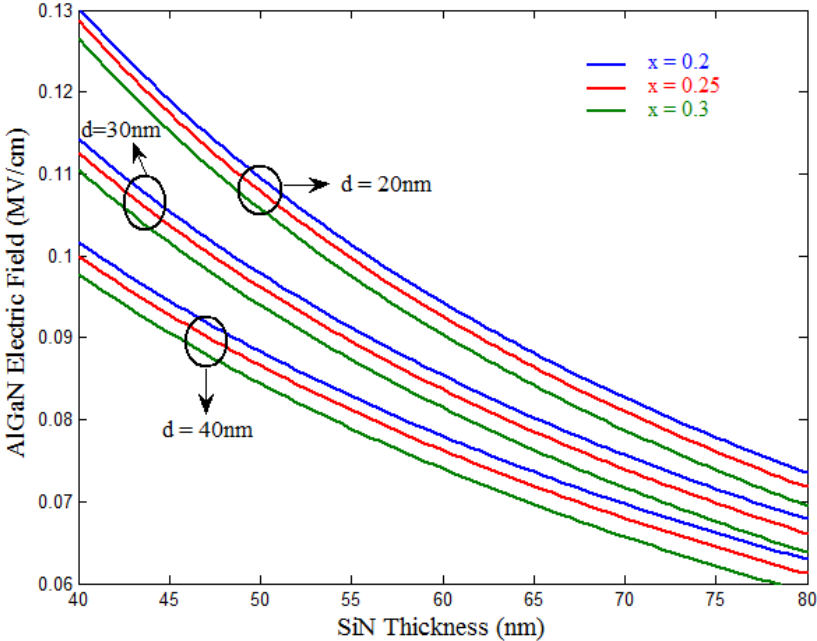
Figure 24. The electric field in $Al_xGa_{1-x}N$ layer grown on GaN versus the thickness of α–SiN passivation layer for different aluminum mole fractions (x) and AlGaN thicknesses, d.

As shown in this figure, the electric field in AlGaN layer is decreased by increasing the α−SiN passivation layer thickness. Moreover, the electric field is decreased by increasing AlGaN thickness.

The 2DEG density change due to the variation of α−SiN film thickness, Al mole fraction and AlGaN thickness alters the mobility, affecting the ON state resistance in HEMTs. The variation of Hall mobility for different 2DEG densities has been studied in literature [48, 49].

Experimental measurement of 2DEG in passivated AlGaN/GaN heterostructures

In order to investigate the validity of the proposed model, different α−SiN thicknesses were grown on an $Al_{0.25}Ga_{0.75}N$/GaN heterostructure on Si (111) substrate with an AlGaN thickness of 17.5 nm. First, samples were held in diluted HCl solution for 10 minutes to remove the native oxide (The HCl:H_2O ratio was 1:10). α−SiN layers were deposited with an Oxford PlasmaLab 80Plus PECVD system. The SiH_4 and N_2 flow rates were 120 and 900 sccm, respectively, with a table temperature of 350 °C and an RF power of 60 W. The 2DEG density was measured using Lehighton Model 1605 non-contact Hall mobility measurement system, where multiple measurements and averaging were implemented to obtain more statistically significant data. Figure 25 illustrates the measured 2DEG densities for different passivation layer thicknesses [41] (© 2013 IEEE).

40
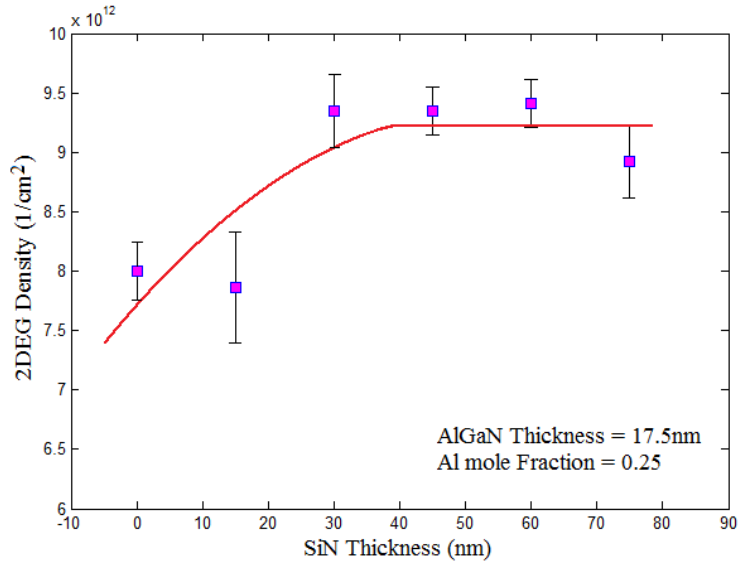
Figure 25. The experimentally measured 2DEG density of as-grown PECVD α−SiN passivated $Al_{0.25}Ga_{0.75}N$/GaN heterostructure versus α−SiN thickness.

The 2DEG density initially increases with increasing α−SiN layer thickness and eventually saturates for thicknesses greater than 40 nm, denoting the necessary passivation layer thickness to achieve the optimum 2DEG density for Al mole fraction of 0.25 and AlGaN thickness of 17.5 nm.

To investigate the effects of post-annealing on 2DEG density, an MTI OTF 1200-X Rapid Thermal Processing (RTP) system was used to anneal the sample with α−SiN passivation layer thickness of 60 nm. The samples were first held at 450 °C for 1 minute to stabilize the temperature and reduce the risk of possible sample cracking due to rapid temperature change. The temperature was then increased to the target value with a rise time of 15 seconds. Nitrogen was used as the ambient gas and the chamber

pressure was set to 30 Torr. Figure 26 illustrates the 2DEG density variation for different annealing times and temperatures [41] .
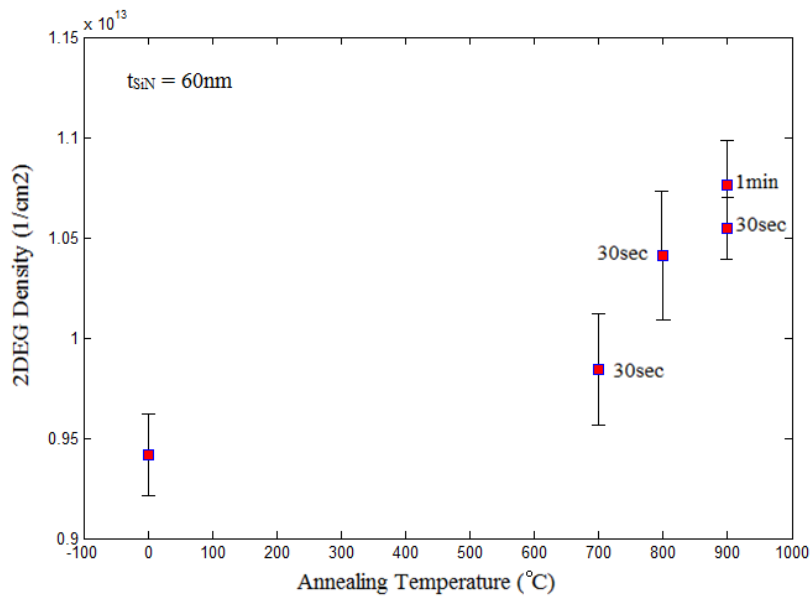
Figure 26. The experimentally measured 2DEG density of PECVD α−SiN passivated $Al_{0.25}Ga_{0.75}N$/GaN heterostructure for different annealing times and temperatures. The α−SiN and AlGaN thicknesses were 60 and 17.5 nm, respectively.

Annealing the sample after α−SiN deposition improves the 2DEG density. The increase in 2DEG density is due to the reduction of trap density at α−SiN/AlGaN interface as reported for Al_2O_3/GaN interface in the literature [50-52].

The 2DEG densities are calculated using the proposed model for the unannealed samples with different SiN thicknesses. Figure 27 compares the experimentally

measured 2DEG density illustrated in Figure 25 with the calculated values based on the

proposed model [41] (© 2013 IEEE).
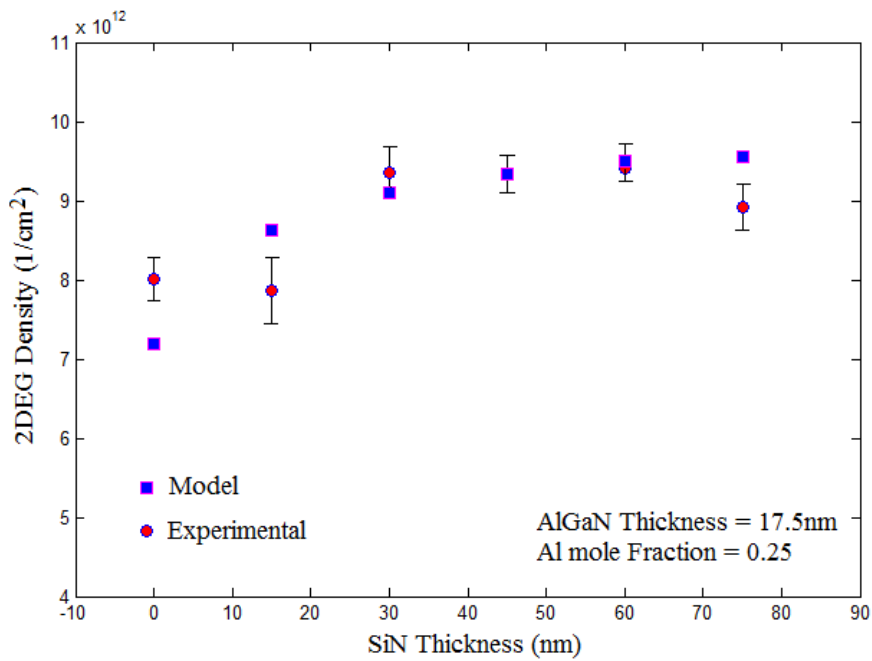
Figure 27. The calculated and experimentally measured 2DEG density of as-grown
PECVD $\alpha-$SiN passivated $Al_{0.25}Ga_{0.75}N/GaN$ heterostructure versus $\alpha-$SiN thickness.
The AlGaN thickness was 17.5 nm.

The calculated 2DEG densities correspond well with the experimental data. The model

accurately predicts the 2DEG density increase with increasing $\alpha-$SiN thickness, and the

saturation that occurs for $\alpha-$SiN thicknesses greater than 40 nm [41] (© 2013 IEEE).

Surface passivation and breakdown

Analyses have been performed in the literature to describe the impact of material parameters on semiconductor devices performance [53, 54]. According to these studies, in devices with uniformly doped drift region, the smallest ON-state resistance occurs when the drift regions depletion layer punch-through occurs to the heavily doped substrate simultaneously with breakdown. Therefore, to optimize R_{ON}, the doping concentration of the drift region should be selected such that the drift region and depletion layer widths are equal to each other at breakdown [53, 54]. In this situation, the voltage is supported in the depletion layer with a linear electric field distribution which peaks right at the junction. The peak value is equal to the critical electric field (E_{crit}) at breakdown [53, 54]. Therefore, the power device figure of merit is represented as

$$FOM = \frac{V_{BR}^2}{R_{ON}} = \frac{1}{4} \times \varepsilon \cdot \mu \cdot E_{crit}^3 , \qquad (27)$$

where ε and μ are the electric permittivity and mobility of the semiconductor. Using Eq.27, the R_{ON}-V_{BR} limits of different materials are derived as illustrated in Figure 3Figure 3 [55, 56]. As shown in this figure, all reported literature data for GaN HEMTs are far away from the introduced GaN limit. The ON state resistances of the experimentally reported data are almost more than an order of magnitude larger than that suggested by the introduced GaN limit. The reason can be explained by the use of a FOM developed for devices with uniformly doped drift regions. It should not be applied to AlGaN/GaN HEMTs in which the drift region is usually intrinsic and there is no

44

doped junction. Moreover, Eq.27 does not take into account the polarization electric fields of III-Nitride semiconductors which add to the bias-induced electric field. The existence of polarization electric fields together with the undoped drift region cause the breakdown to occur at much lower voltages than what is predicted by Eq.27. An appropriate figure of merit must be developed for AlGaN/GaN HEMTs to allow device designers latitude in higher voltage design. To calculate the FOM of AlGaN/GaN HEMTs, 2DEG density and AlGaN surface passivation together with polarization electric fields and strain relaxation need to be taken into account.

In order to obtain the power device figure of merit, the breakdown mechanism in AlGaN/GaN HEMTs needs to be analyzed. Figure 28Figure 28 illustrates a typical AlGaN/GaN HEMT at its OFF state.
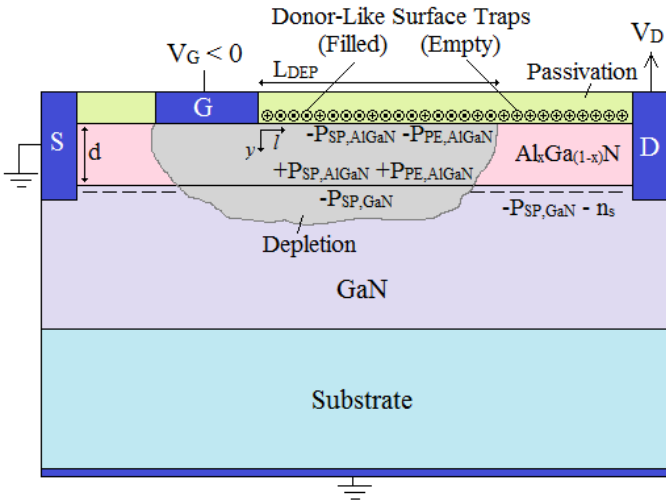
Figure 28. A typical AlGaN/GaN HEMT at its OFF state.

45

In this figure, $P_{SP,AlGaN}$ and $P_{SP,GaN}$ are the spontaneous polarizations of AlGaN and GaN respectively, $P_{PE,AlGaN}$ is the piezoelectric polarization of AlGaN and n_s is the 2DEG density [41] (© 2013 IEEE). Depending on the passivation layer properties and growth conditions, some donor-like surface traps remain unpassivated at the AlGaN/passivation layer interface as illustrated in Figure 28Figure 28. The density of surface traps could be larger than 1.5e13 cm^{-2} [57]. A portion of these donor-like surface traps are filled due to electron injection from the gate, resulting in the partial depletion of gate to drain region [58]. The density of the filled surface traps and the depletion length depend on the gate and drain biases, trap density and trap state energy.

In order to investigate the effects of trap density at AlGaN/passivation layer interface on R_{ON} and V_{BR}, the two dimensional potential distribution in AlGaN needs to be calculated. If the drain side of the gate edge is selected as the origin of coordinates (Figure 28Figure 28), the Poisson equation implies that [58]

$$\frac{\partial^2 V(l,y)}{\partial l^2} + \frac{\partial^2 V(l,y)}{\partial y^2} = \frac{-q \cdot \rho}{\varepsilon_0 \varepsilon_{AlGaN}},$$
(28)

where $V(l,y)$ is the electrostatic potential at (l,y) coordinates, q is the electron charge, ρ is the charge density, ε_0 is the electric permittivity of the vacuum and ε_{AlGaN} is the relative electric permittivity of AlGaN. Simulation results with Synopsys-Sentaurus software for different device parameters indicate that the potential distribution along y-axis in AlGaN is linear. Therefore the second term of Eq.28 is equal to zero. Applying Eq.28 to the depletion region and along the line $y = 0$ results in

$$\left. \frac{\partial^2 V(l,y)}{\partial l^2} \right|_{y=0} = \frac{q \cdot (P_{PE,AlGaN} + P_{SP,AlGaN} - D_T + D_{T,Filled}(l))}{\varepsilon_0 \varepsilon_{AlGaN}}, \qquad (29)$$

in which D_T is the donor-like trap density at AlGaN/GaN interface and $D_{T,Filled}(l)$ is the density of traps that are filled due to charge injection from the gate. The potential distribution along the line $y = 0$ in AlGaN can be approximated by a parabolic function as [59]

$$V(l,0) = a_n \cdot l^n + \ldots + a_2 \cdot l^2 + a_1 \cdot l + a_0. \qquad (30)$$

Substituting Eq.30 into Eq.29 and evaluating Eq.29 at $l = 0$ (gate edge), a_2 is represented as

$$a_2 = \frac{q \cdot (P_{PE,AlGaN} + P_{SP,AlGaN} - D_T + D_{T,Filled}(0))}{2\varepsilon_0 \varepsilon_{AlGaN}}. \qquad (31)$$

a_2 is the second-order derivative (curvature) of the horizontal potential distribution at the gate edge. As indicated in Eq.31, a_2 is a function of D_T and $D_{T,Filled}$ at the gate edge. This is well-reflected in Figure 29 where it shows the simulated potential distribution along AlGaN/passivation layer interface in a device with the gate to drain distance of 2 um for various trap densities.
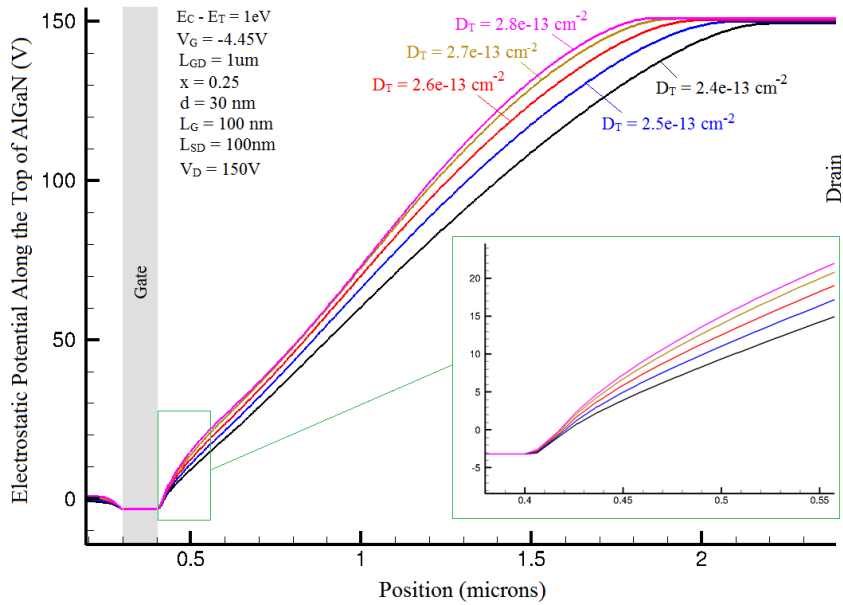
Figure 29. The electrostatic potential in AlGaN side of the AlGaN/passivation layer interface of the structure shown in Figure 28~~Figure 28~~ with a gate to drain distance of 2 um, Al mole fraction of 0.25 and AlGaN thickness of 30 nm for different donor-like surface trap densities. The trap state energy was set 1eV below AlGaN conduction band.

Larger trap densities provide more negative a_2 at the gate edge and the potential distribution becomes linear (curvature = 0) by decreasing the trap density. The slopes of these plots represent the horizontal components of the electric field along AlGaN/passivation layer interface. As shown in Figure 29~~Figure 29~~, decreasing the trap density reduces the horizontal electric field at the gate edge. This results in a reduction in the total electric field peak at the gate edge both in AlGaN and GaN layers, improving the breakdown voltage of the device (Figure 30~~Figure 30~~ and Figure 31~~Figure 31~~).

48
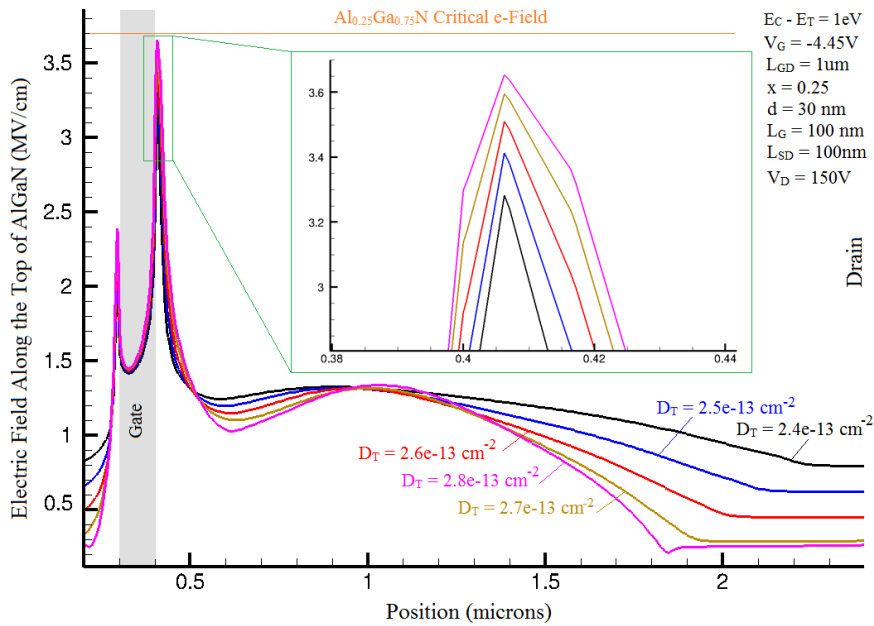
Figure 30. The total electric field in AlGaN side of the AlGaN/passivation layer interface of the structure shown in Figure 28Figure 28 with a gate to drain distance of 2 um, Al mole fraction of 0.25, drain bias of 150V and AlGaN thickness of 30 nm for different donor-like surface trap densities. The trap state energy was set 1eV below AlGaN conduction band. The peak electric field is decreased by decreasing the trap density.

Formatted: Font: Not Bold

Figure 31. The total electric field in GaN side of the AlGaN/GaN interface of the structure shown in Figure 28~~Figure 28~~ with a gate to drain distance of 2 um, Al mole fraction of 0.25, drain bias of 150V and AlGaN thickness of 30 nm for different donor-like surface trap densities. The trap state energy was set 1eV below AlGaN conduction band. The peak electric field is decreased by decreasing the trap density.

Therefore, the breakdown voltage of the device is increased with a better surface passivation which reduces the density of donor-like surface trap at AlGaN/passivation layer interface. The increase in the breakdown voltage by decreasing the surface trap density has also been reported in the literature [60].

However decreasing the trap density at AlGaN/passivation layer interface improves the breakdown voltage, it degrades the ON-state resistance. Figure 32~~Figure 32~~ illustrates the I_D-V_D characteristics of the device simulated in Figure 31~~Figure 31~~ at the zero gate bias.
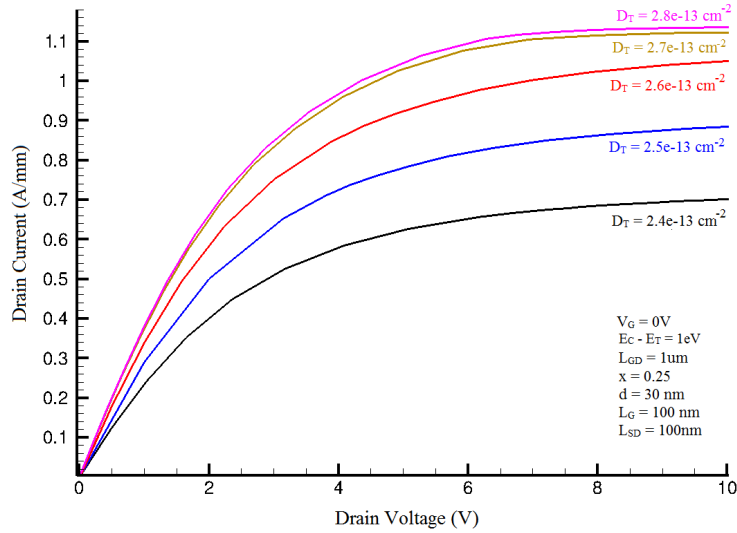
Figure 32. The I_D-V_D characteristics of the structure shown in Figure 28Figure 28 with a gate to drain distance of 2 um, Al mole fraction of 0.25 and AlGaN thickness of 30 nm for different donor-like surface trap densities. The trap state energy was set 1eV below AlGaN conduction band. The ON-state resistance is increased by decreasing the surface trap density.

As shown in this figure, the ON-state resistance is increased by decreasing the AlGaN/passivation layer interface trap density. This is due to charge injection from the gate into some empty traps at the ON-state, resulting in the reduction of 2DEG density. Therefore, there is a tradeoff between the breakdown voltage and ON-state resistance.

Surface passivation and R_{ON}-V_{BR} FOM

In order to obtain the FOM of AlGaN/GaN HEMTs, the breakdown voltage and ON-state resistance of device need to be determined for different trap densities, gate to drain distances, Al mole fractions and AlGaN thicknesses. To do so, the 2D electric field distributions of HEMTs with different design parameters have been simulated for various drain biases. The breakdown voltage of the device is defined as the drain bias at which the peak electric field value is equal to the critical breakdown electric field. Assuming a GaN critical breakdown electric field of 2.4 MV/cm, the critical breakdown electric field of AlGaN for Al mole fractions less than 0.5 is proportional to its bandgap energy to the power of 2.5 [61]. Therefore, the critical breakdown electric field of AlGaN for different Al mole fractions of x is written as

$$E_{c,AlGaN} = 0.11(E_g)^{2.5} = 0.11(2.5x + 3.45)^{2.5} (MV/cm),\qquad(32)$$

in which E_g is the bandgap energy of AlGaN. Taking into account these considerations, the breakdown voltage of the structure shown in Figure 28Figure 28 is simulated for an AlGaN thickness of 30 nm, Al mole fraction of 0.2 and different gate to drain distances (Figure 33Figure 33).

52
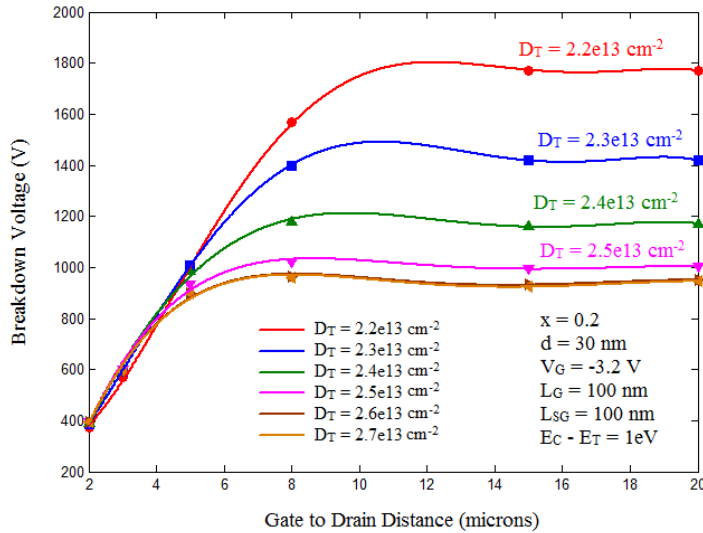
Figure 33. The breakdown voltage of the structure shown in Figure 28~~Figure 28~~ versus the gate to drain spacing for an Al mole fraction of 0.2, AlGaN thickness of 30 nm and different donor-like surface trap densities. The trap state energy was set 1eV below AlGaN conduction band.

The breakdown voltage increases by increasing the gate to drain distance and it eventually saturates. The gate to drain distance at which the breakdown voltage starts to saturate and the saturation value are functions of trap density, trap state energy, Al mole fraction and AlGaN thickness. As illustrated in Figure 33~~Figure 33~~, decreasing the donor-like trap density (i.e. better AlGaN surface passivation), improves the breakdown voltage of the device. The change in breakdown voltage by using different passivation layers has also been reported in the literature. It is shown that SiN-passivated AlGaN/GaN HEMTs exhibit different breakdown voltages than SiO_2-passivated HEMTs [8]. $\alpha-$AlN passivated AlGaN/GaN HEMTs with breakdown voltages larger than 10 kV were recently reported [16].

53

Figure 34Figure 34 illustrates the ON-state resistance versus the gate to drain distance

for devices simulated in Figure 33Figure 33.
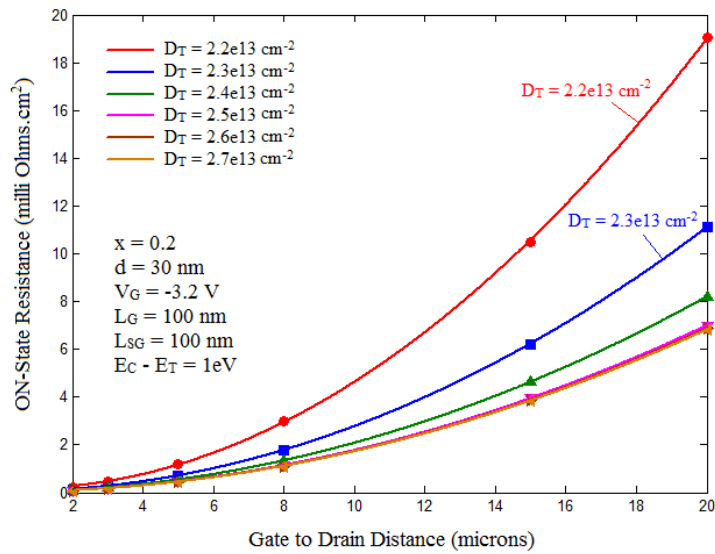
Figure 34. The ON-state resistance of the structure shown in Figure 28Figure 28 versus the gate to drain spacing for an Al mole fraction of 0.2, AlGaN thickness of 30 nm and different donor-like surface trap densities. The trap state energy was set 1eV below AlGaN conduction band energy.

As shown in this figure, the ON-state resistance is increased by decreasing the trap

density.

In order to obtain the FOM of the devices simulated in Figure 34Figure 34, the

ON-state resistance is sketched versus the breakdown voltage (Figure 35Figure 35).
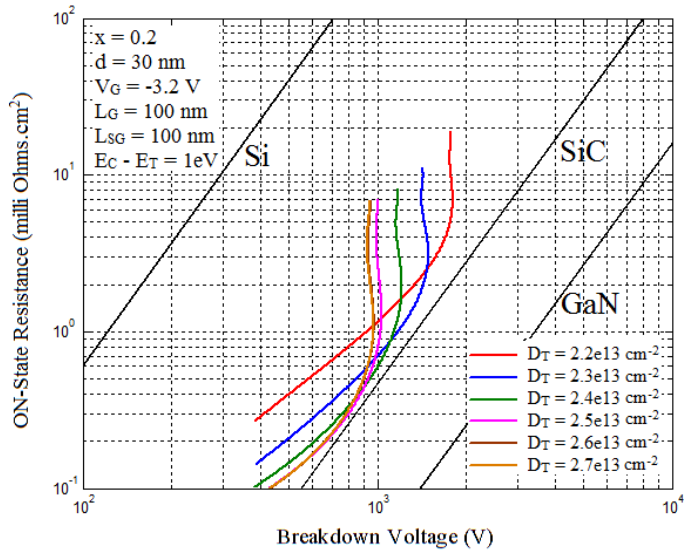
Figure 35. The R_{ON}-V_{BR} characteristics of the device shown in Figure 28Figure 28 with an Al mole fraction of 0.2, AlGaN thickness of 30 nm and different donor-like surface trap densities. The trap state energy was set 1eV below AlGaN conduction band.

The R_{ON}-V_{BR} characteristics are near or above SiC limit line and they are far away from the previously introduced GaN limit. This describes the reason why the experimentally reported data in the literature are not close to the GaN limit line as shown in Figure 3Figure 3.

In order to obtain the R_{ON}-V_{BR} characteristics for different Al mole fractions (x) and AlGaN thicknesses (d), the threshold voltage needs to be calculated for different x and d. If ϕ_b is the effective Schottky gate barrier and ΔE_C is the conduction band discontinuity at AlGaN/GaN interface (Eq.19), the threshold voltage of the device is represented as [62]

55

$$V_{th} = \phi_b - \Delta E_C - \frac{P_{SP,AlGaN} + P_{PE,AlGaN} - P_{SP,GaN}}{\varepsilon_0 \cdot \varepsilon_{AlGaN}} \cdot d , \qquad (33)$$

in which $P_{SP,AlGaN}$ and $P_{SP,GaN}$ are the spontaneous polarizations of AlGaN and GaN respectively and $P_{PE,AlGaN}$ is the piezoelectric polarization of AlGaN. The $P_{SP,AlGaN}$, $P_{SP,GaN}$ and $P_{PE,AlGaN}$ are calculated for different Al mole fractions and AlGaN thicknesses taking into account the strain relaxation [41] (© 2013 IEEE). Therefore, the threshold voltage of the device is calculated for different Al mole fractions and AlGaN thicknesses, allowing for the simulation of V_{BR}-R_{ON} characteristics for different x and d as illustrated in Figure 36Figure 36 and Figure 37Figure 37 [41] (© 2013 IEEE).
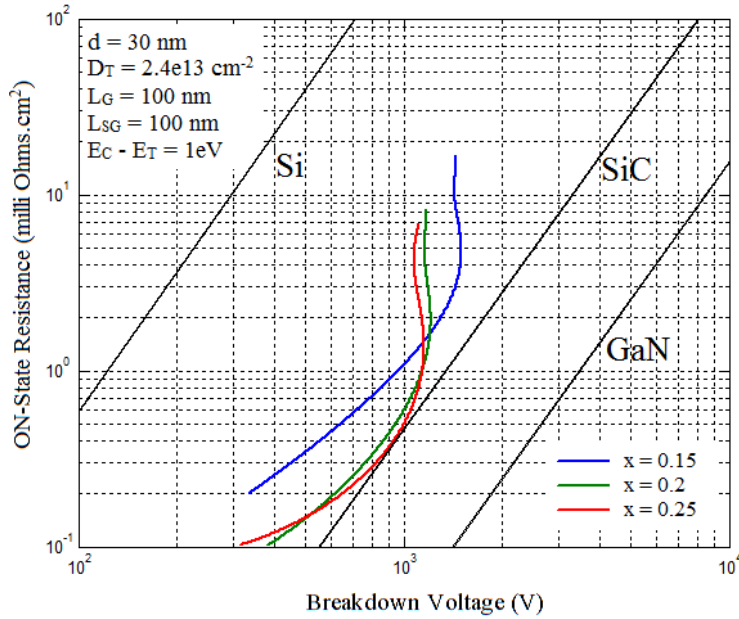
Figure 36. The R_{ON}-V_{BR} characteristics of the device shown in Figure 28Figure 28 with an AlGaN thickness of 30 nm, AlGaN/passivation layer trap density of 2.4e13 cm^{-2} and

56

different Al mole fractions. The trap state energy was set 1eV below AlGaN conduction band.
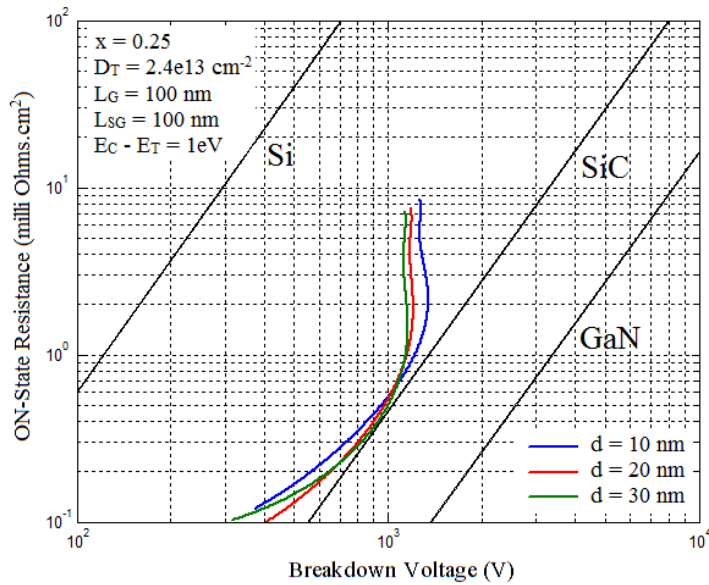
Figure 37. The R_{ON}-V_{BR} characteristics of the device shown in Figure 28~~Figure 28~~ with an Al mole fraction of 0.25, AlGaN/passivation layer trap density of 2.4e13 cm^{-2} and different AlGaN thicknesses. The trap state energy was set 1eV below AlGaN conduction band energy.

As shown in Figure 36~~Figure 36~~ and Figure 37~~Figure 37~~, decreasing x and d allows for

achieving higher breakdown voltages, however, it degrades the ON-state resistance due

to the reduction in 2DEG density [41] (© 2013 IEEE). For larger x and d, no significant

differences are seen in R_{ON}-V_{BR} characteristics as the 2DEG density saturates by

increasing d and x [41] (© 2013 IEEE).

In previous simulations, we did not consider the effects of field plate as it has been

intensively studied in the literature [63-65]. Different field plate configurations and

57

dimensions will change both R_{ON} and V_{BR}, resulting in different FOMs. In addition to field plate, the implementation of resurf in drain region can improve the breakdown voltage and affect R_{ON} [13].

In the proposed model in this chapter, we have used the AlGaN/GaN heterostructure as it is commercially available. However, the drain region of the TMOSHFET is an AlGaN/AlN heterostructure instead of AlGaN/GaN. The model can be extended to AlGaN/AlN if the AlN material parameters are used instead of GaN parameters. Therefore, the proposed model can be used to design the drain region of TMOSHFET.

Figure 38Figure 38 illustrates the OFF-state electrostatic potential along the drain region of the TMOSHFET structure shown in Figure 10Figure 10 with a gate to drain distance of 10 um at different drain biases and Figure 39Figure 39 shows the corresponding electric field profile.

Formatted: Font: 12 pt

Formatted: Font: 12 pt

Formatted: Font: 12 pt
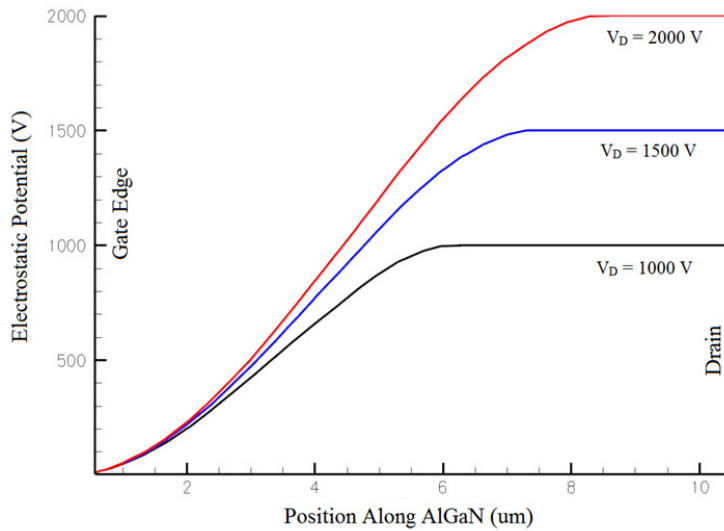
Figure 38. The OFF-state electrostatic potential along the drain region of the TMOSHFET structure shown in Figure 10Figure 10 with a gate to drain spacing of 10 um at different drain biases of V_D.
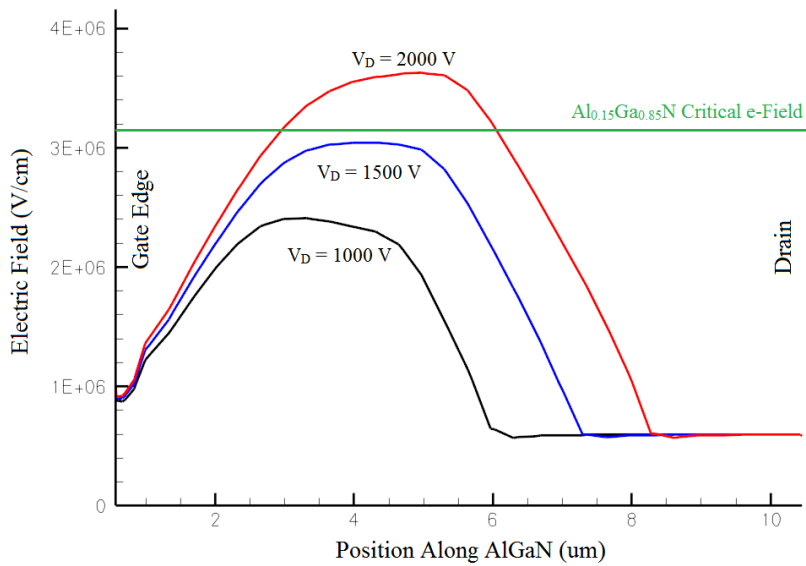
Figure 39. The OFF-state total electric field along the drain region of the TMOSHFET structure shown in Figure 10Figure 10 with a gate to drain spacing of 10 um at different drain biases of V_D.

The breakdown voltage of the device for different gate to drain biases can be extracted by simulating the electric field along the drain as shown in Figure 39Figure 39. To find the ON-state resistance, the I_D-V_D plots need to be simulated for different gate to drain distances. Figure 40Figure 40 shows the I_D-V_D plots for a gate to drain distance of 10 um.

L_{GD} = 10 um

V_G = 3 V

V_G = 2.9 V

V_G = 2.8 V

V_G = 2.7 V

V_G = 2.6 V

V_G = 2.5 V

V_G = 2 V
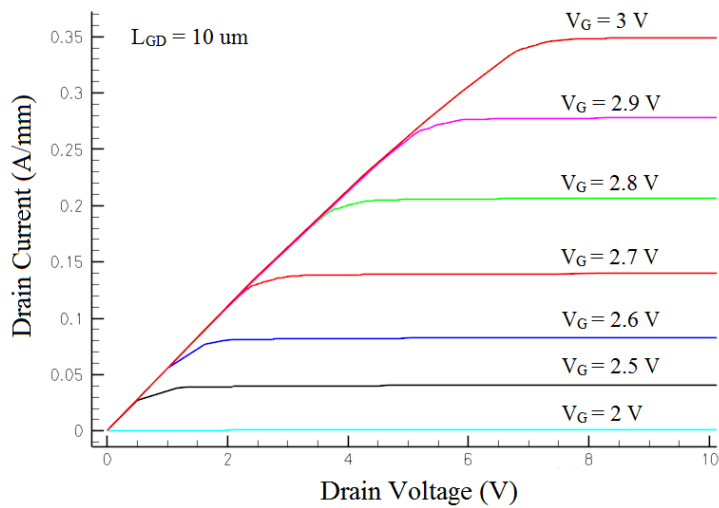
Figure 40. The I_D-V_D characteristics of the TMOSHFET structure shown in Figure 10Figure 10 with a gate to drain spacing of 10 um.

Therefore, the R_{ON}-V_{BR} FOM of the TMOSHFETs can be obtained for different gate to drain spacing. Figure 41Figure 41 compares the R_{ON}-V_{BR} FOM of the TMOSHFET of

60

Figure 10Figure 10 with different gate to drain spacing with those of the experimentally

reported AlGaN/GaN HEMTs in the literature.
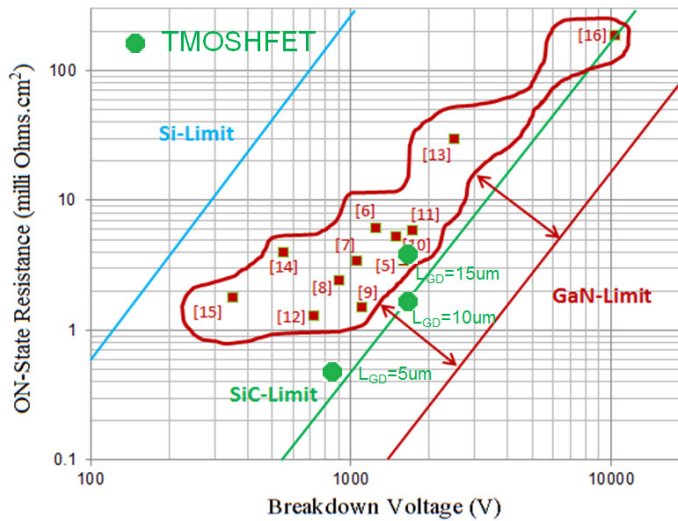
Figure 41. The R_{ON}-V_{BR} FOMs of the TMOSHFET structure shown in Figure 10Figure 10 with different gate to drain spacing. The experimentally reported literature data for AlGaN/GaN HEMTS are included.

Increasing the gate to drain distance improves the Breakdown voltage of TMOSHFET

and it eventually gets saturated. As shown in Figure 41Figure 41, significant

improvements in FOM are achieved in TMOSHFETs with L_{GD} of 5 and 10 nm

compared to the AlGaN/GaN HEMTs.

61

CHAPTER V

TUNNELING MECHANISMS IN ALGAN/GAN SBD

Introduction

In this chapter, the tunneling current in the gate region of TMOSHFET is demonstrated using an AlGaN/GaN heterostructure. AlGaN/GaN Schottky Barrier Diodes (SBDs) with different AlGaN thicknesses are fabricated and their I-V and G-V plots are analyzed. To do so, first the Ti/Al/Ni/Au Ohmic contacts to AlGaN/GaN heterostructures are realized and characterized. Then, a dry etch recipe is used to etch the AlGaN to achieve SBDs with various AlGaN thicknesses. The effects of this dry etch on the trap density of AlGaN are investigated using G_P-ω/ω method. By analyzing the current-voltage characteristics of SBDs with various AlGaN thicknesses, different tunneling mechanisms (Poole-Frenkel, Fowler-Nordheim and etc.) in samples are realized and compared with each other.

Ti/Al/Ni/Au Ohmic contact to GaN

To fabricate AlGaN/GaN SBDs, a low-resistance Ohmic contact should first be formed to the GaN. Ti/Al/Ni/Au Ohmic contact to GaN is investigated in the literature [66-68]. Titanium is used as the first metal since it can form TiN bonds with Nitrogen atoms of GaN. Then, a thick aluminum layer is used as the transition layer as it has a low resistance. The top Au layer is to prevent the oxidization of contact and Ni prevents Au diffusion into Al while annealing.

To fabricate the Ohmic contacts on our AlGaN/GaN sample, the sample is first

62

put in diluted HCl to remove the native oxide (the HCl:H_2O ratio was 1:10). Then 138 nm of α−SiN was deposited with the Oxford PlasmaLab 80Plus PECVD system. The SiH_4 and N_2 flow rates were 120 and 900 sccm, respectively, with a table temperature of 350 °C and an RF power of 60 W. In order to do the lift-off process, the sample is coated with Lift-Off Resist (LOR) for 40 sec at 2000 rpm. The acceleration and deceleration times of the spincoater were 0.2 sec. The sample is then baked on hot plate at 165 °C for 8 minutes. After that, AZ 5214 photoresist is coated on the wafer for 45 sec at 4500 rpm with the acceleration and deceleration times of 5 sec followed by 2 minutes of soft bake on the hot plate at 120 °C. Then, it is exposed to UV light to transfer the mask pattern using the Karl Suss MA6 mask aligner. The exposed regions are then developed in MF 312 photoresist developer for 1 minute followed by sample hard bake in 135 °C oven. To remove the SiN in opened windows, the sample is put in Buffered Oxide Etch (BOE) for 45 sec. The SEM image shows that 45 sec wet etch is enough to remove the entire 138 nm of PECVD SiN (Figure 42Figure 42). Then, Ti(30 nm)/Al(180 nm)/Ni(40 nm) are evaporated on the sample using the electron beam evaporation system. Right after taking out the sample from the e-beam evaporator chamber, 50 nm of gold is sputtered on the sample using the Hummer Sputter Coater. LOR and photoresists are stripped off using AZ 400T photoresist stripper and the sample is annealed at 165 °C for 30 sec using MTI OTF 1200-X Rapid Thermal Processing (RTP) system.

Formatted: Font: 12 pt
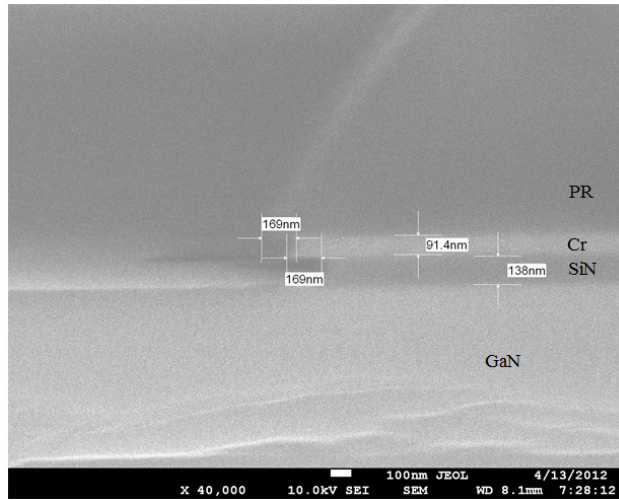
Figure 42. The cross-sectional SEM image of PECVD SiN on AlGaN/GaN after 45 sec BOE etching.

Figure 43Figure 43 shows the programmed temperature profile of RTP (green

line) and the actual chamber temperature (red line).
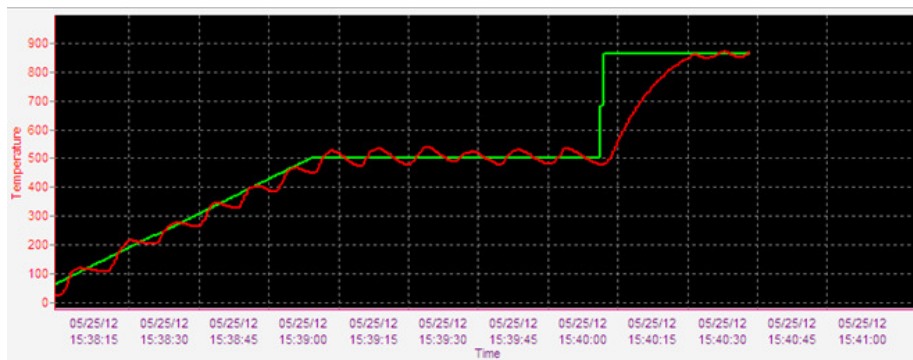
Figure 43. The programmed (green line) and actual (red line) RTP chamber temperatures.

As shown in this figure, the sample is kept at 500 °C for 1 minute before the 865 °C annealing to reduce the risk of sample cracking due to the fast temperature change. Figure 44Figure 44 shows the photo of fabricated contacts with different spacings before

and after annealing.

| Before Anneal | After Anneal |
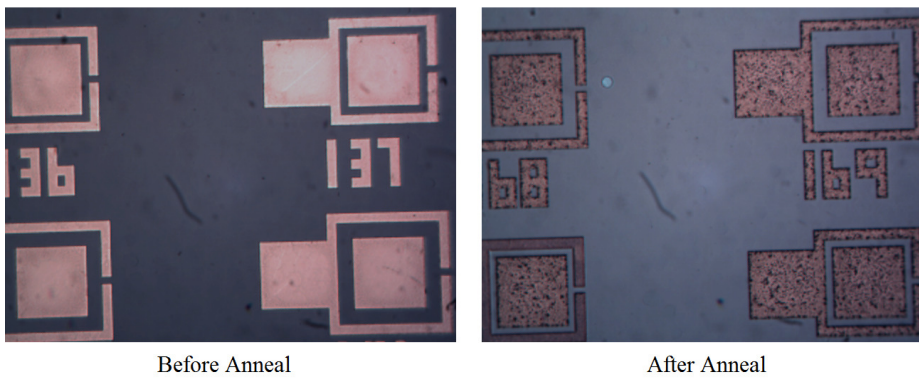
Figure 44. The fabricated Ti/Al/Ni/Au contacts to AlGaN/GaN heterostructure befor and after the annealing.

The appearance of black dots on the contacts after annealing is due to the intermixing of Al and Au [69].

The current-voltage characteristics of the fabricated contacts with different spacings are measured using HP 4145B Semiconductor Parameter Analyzer and illustrated in Figure 45Figure 45.
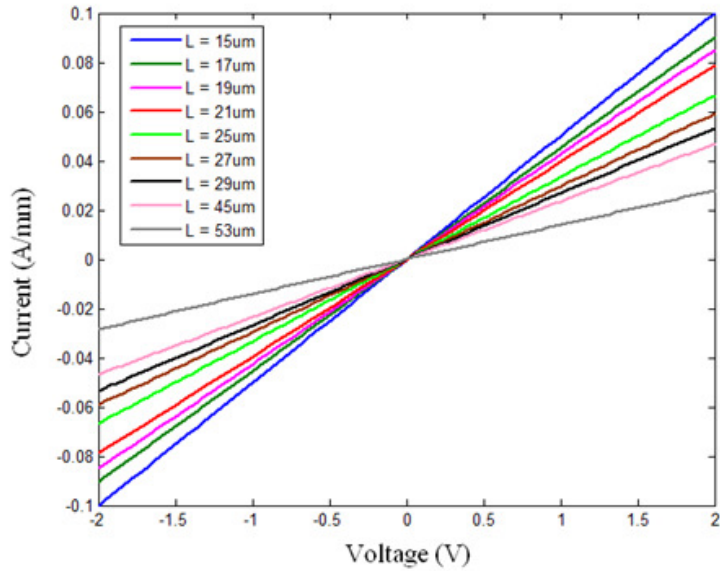
Figure 45. The current-voltage characteristics of Ohmic contacts with different spacing of L.

As shown in this illustration, the contacts are completely linear. The inverse slope of the I-V characteristic gives the resistance between the contacts which is the sum of two contact resistances (R_C) and the 2DEG resistance. The summation of contact resistances can be extracted from the intercept of the resistance versus L plot with the y-axis (Figure 46Figure 46).
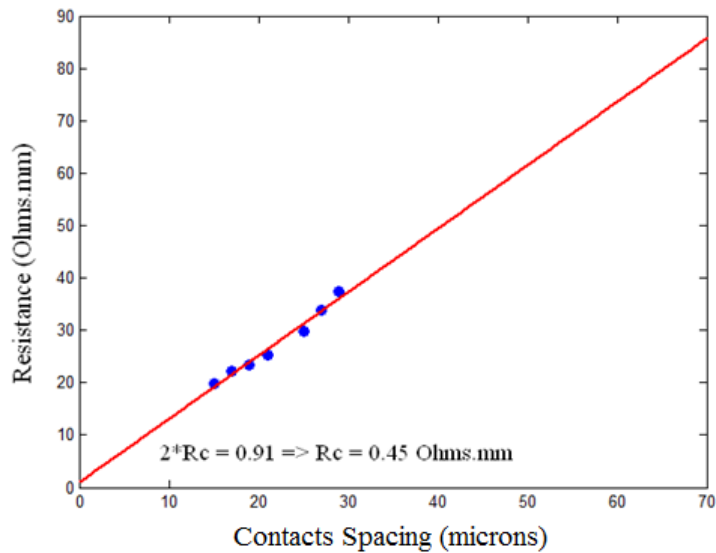
Figure 46. The measured resistance between the contacts versus contact spacing.

For the fabricated contacts, the contact resistance of 0.45 Ohms.mm is realized as shown in this figure.

SF$_6$ dry etching of AlGaN and its impacts on the trap density

To fabricate the gate region of TMOSHFET, the AlGaN should be etched as shown in Figure 10Figure 10. Chlorine and fluorine based dry etchings are usually used to etch the III-Nitride semiconductors [70-73]. We have used the dry etch recipe introduced in reference [73] to etch the AlGaN/GaN heterostructure using an Oxford PlasmaLab 100 Plus RIE system. First, the native oxide on the wafer is removed by putting the sample in diluted HCl solution with an HCl:DI ratio of 1:10. 138 nm of SiN is then grown on the sample using the PECVD system. After that, 100 nm of Cr was evaporated on the sample and patterned using lithography and Cr-1A etchant to act as

67

the hard mask for the dry etching. The Inductively Coupled Plasma (ICP) Reactive Ion Etching (RIE) is performed at SF_6 and Ar flow rates of 40 sccm and 10 sccm, respectively, with an ICP power of 200W at the temperature of 16 °C and a chamber pressure of 44 mTorrs. Figure 47Figure 47 and Figure 48Figure 48 show the cross-sectional SEM of the samples etched for 2:30 and 20 minutes with RF powers of 600 W and 400 W respectively. The AlGaN etch rates were 27 nm/min and 15 nm/min for RF powers of 600 W and 400 W respectively.
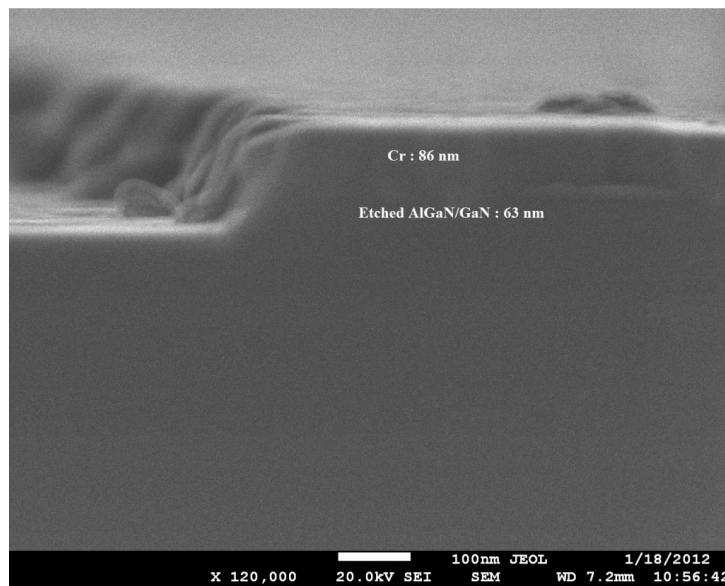
Figure 47. The cross-sectional SEM of the AlGaN/GaN heterostructure after 2:30 minutes of SF_6 dry etching with the RF power of 600 W.
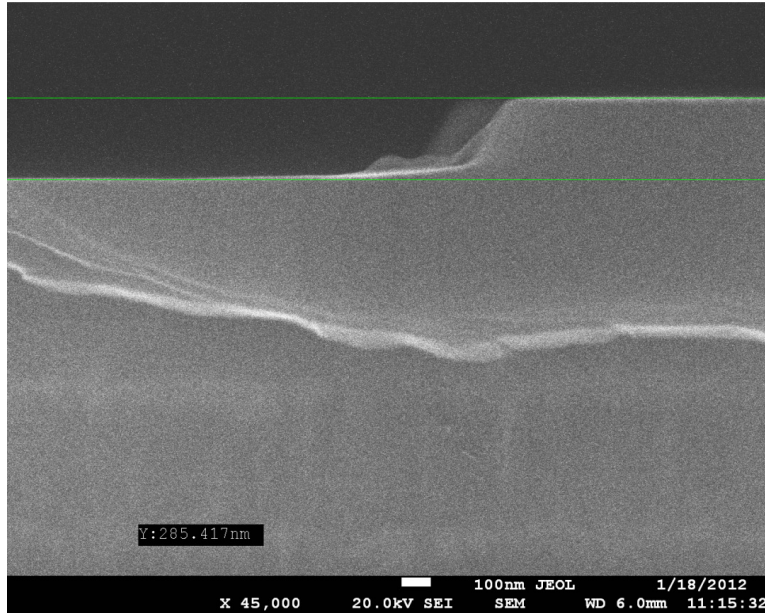
Figure 48. The cross-sectional SEM of the AlGaN/GaN heterostructure after 20 minutes of SF_6 dry etching with the RF power of 400 W.

To investigate the effects of dry etch on the trap density and time constant in AlGaN, SBDs with Ni/Au Schottky contacts on recess-etched AlGaN are fabricated and characterized. $Al_{0.26}Ga_{0.75}N$/GaN heterostructure on Si(111) substrate is used with an AlGaN thickness of 17.5 nm and a 2 nm cap GaN layer (Details of material growth are described in reference [18]). The native oxide on the sample is first removed by putting the sample diluted HCl for 10 minutes (HCl:DI ratio was 1:10). After that, 138 nm of SiN layer is grown on top of the wafer by Plasma Enhanced Chemical Vapor Deposition (PECVD) method using the Oxford PlasmaLab 80 Plus system. The SiH_4 and N_2 flow rates were 120 and 900 sccm, respectively, with an RF power of 60 W and table

69

temperature of 350 °C. Then, 100 nm of Cr is evaporated on SiN as the hard-mask for subsequent dry etching. The Cr and SiN are wet etched using Cr-1A and BOE at the Schottky contact region to create openings for the dry etch. Using the Oxford PlasmaLab 100 Plus RIE system, the AlGaN/GaN heterostructure is etched for 20 sec and 40 sec in two samples. The recipe was same as what mentioned earlier with an RF power of 400 W. The Cr hard-mask is then etched away and the SiN at the Ohmic region is removed using BOE. The LOR and AZ 5214 photoresist are coated and patterned using Karl Suss MA6 mask aligner to form Ohmic regions in subsequent lift-off process. The Ti(30 nm)/Al(100 nm)/Ni(40 nm) metal stack is evaporated on the sample using the e-beam evaporator followed by 50 nm Au sputtering. The Ohmic regions are formed using the lift-off process and the samples are annealed at 865 °C for 30 sec using the MTI OTF 1200-X Rapid Thermal Processing (RTP) system. Finally, 50 nm of Ni is evaporated followed by 50 nm Au sputtering and they are patterned by a lift-off process to form the Schottky contacts on the etched regions. Figure 49Figure 49 illustrates the fabrication process and Figure 50Figure 50 shows the cross-section and top views of the fabricated devices.
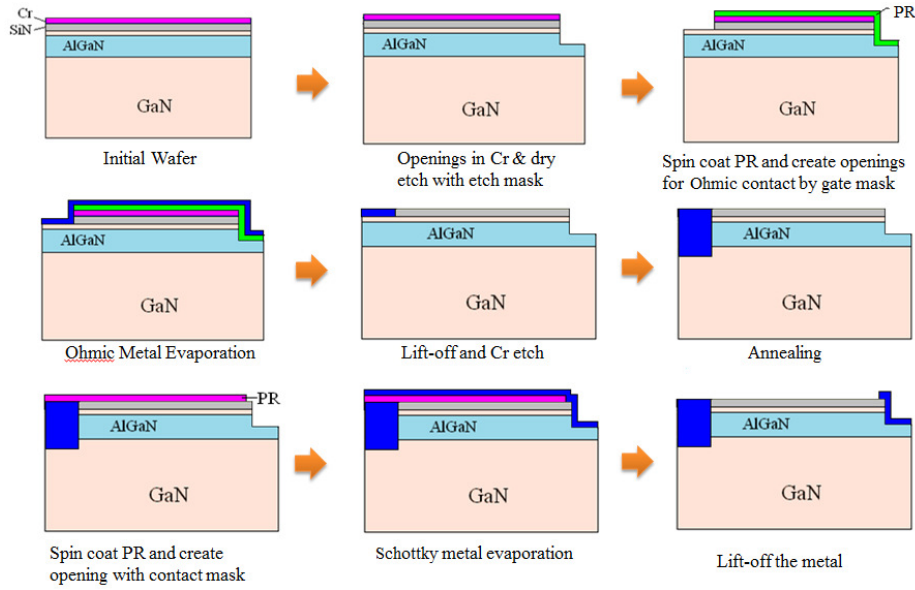
Figure 49. The fabrication process of AlGaN/GaN SBDs.
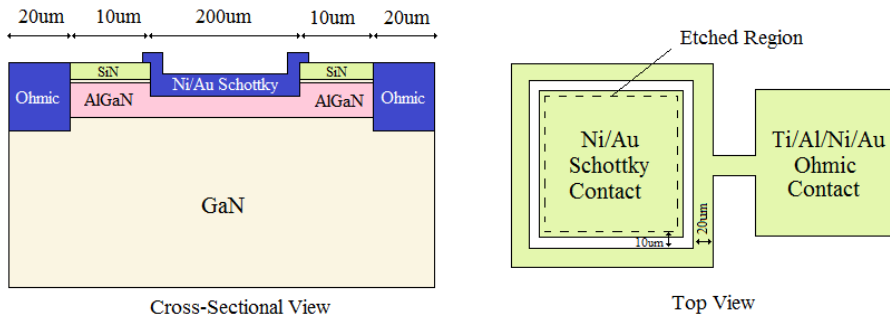
Figure 50. The cross-sectional and top views of fabricated AlGaN/GaN SBDs.

Figure 51Figure 51 illustrates a photo of the fabricated AlGaN/GaN SBD.
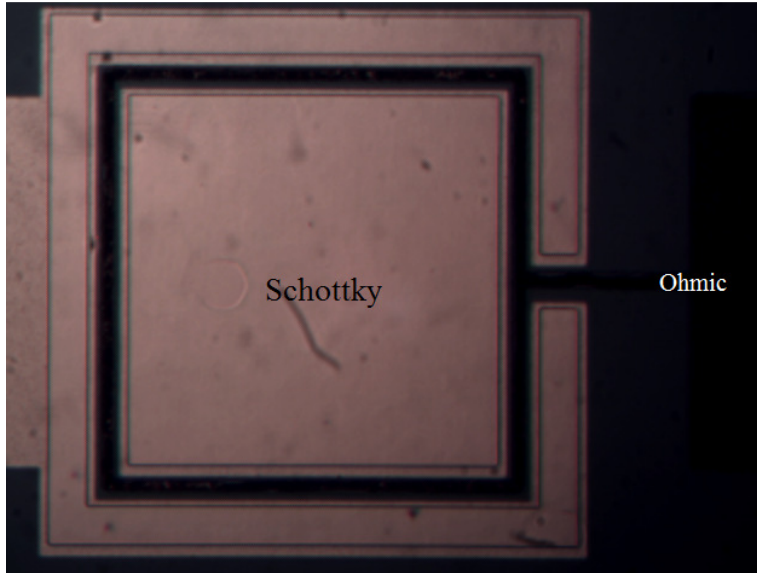
Figure 51. The photo of the fabricated AlGaN/GaN SBD.

The frequency dependent conductance measurement is implementd to characterize the trapping effects in semiconductor devices [52, 74-76]. The relationship between the parallel conductance (G_p) and the trap density (D_T) is expressed as [52, 74-76]

$$\frac{G_p}{\omega} = \frac{qD_T}{2\omega\tau_T} \ln[1 + (\omega\tau_T)^2],$$ (34)

where τ_T is the trap state time constant, ω is the radial frequency and q is the electron charge. D_T and τ_T are extracted by fitting Eq.34 to the experimental G_p/ω versus ω trace. To do so, the conductance-voltage characteristics of the fabricated devices were measured at different frequencies using an Agilent 4284A precision LCR Meter (Figure 52Figure 52).

72
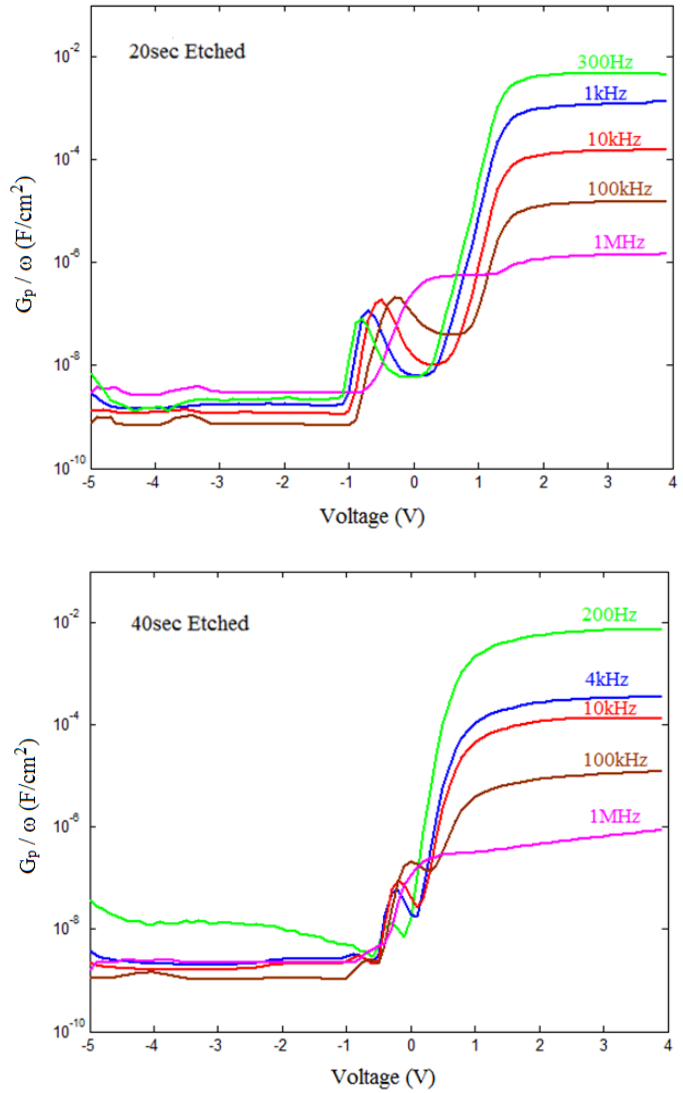
Figure 52. The measured G_P/ω traces versus the applied bias to the Schottky contact for the samples with 20 sec and 40 sec recess etches under Schottky contact.

73

The local maxima at small negative biases are due to the increased trap density at those voltages. The increase in the conductance at positive biases is due to the Ni-AlGaN Schottky diode switch ON rather than the change in trap density. So, Eq.34 can not be applied to calculate the trap density at positive biases.

Based on the measured G_p/ω versus voltage traces, the experimental G_p/ω versus ω plots are calculated and Eq.34 is fitted to the experimental data (Figure 53Figure 53 and Figure 54Figure 54).

Figure 53. The measured and fitted G_P/ω versus ω traces for the samples with 20 sec recess etch under the Schottky contact.
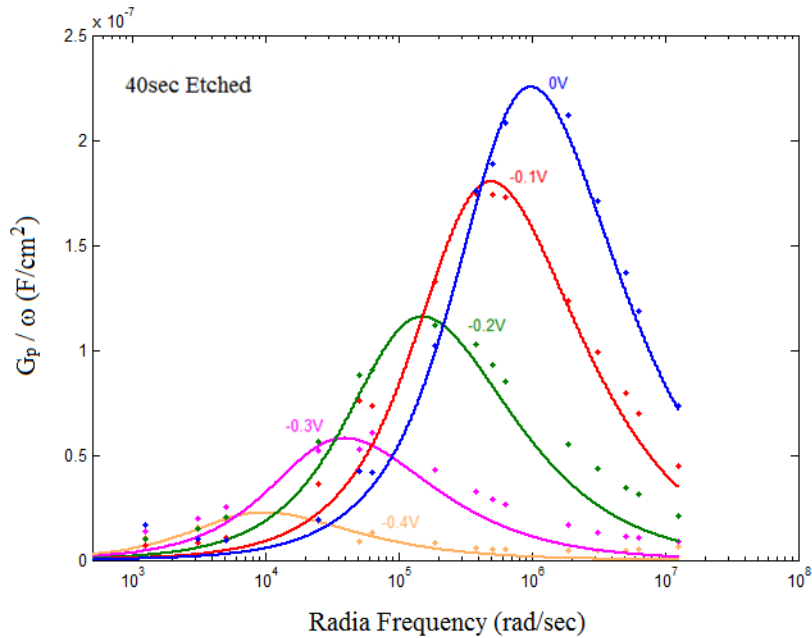
Figure 54. The measured and fitted G_P/ω versus ω traces for the samples with 40 sec recess etch under the Schottky contact.

The frequency range of the measured G_p/ω is limited due to the frequency range of the LCR meter. The experimental G_p/ω peaks are broader than the peaks predicted by equation for the case of 40 sec etched device and they are narrower for 20 sec etched device. The deviation of the experimental G_p/ω peaks from the ones predicted by Eq.34 is due to the time constant dispersions caused by surface potential fluctuations because of the nonuniformities in AlGaN charges and interface traps [75, 77].

Figure 55Figure 55 and Figure 56Figure 56 illustrate the extracted trap density and trap state time constant versus the applied bias for both samples.

> **Formatted:** Font: 12 pt
>
> **Formatted:** Font: 12 pt, Do not check spelling or grammar
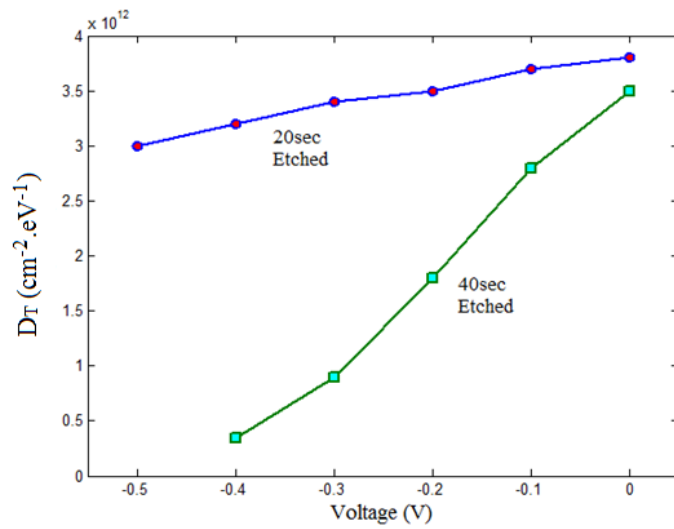
Figure 55. Trap density versus the applied voltage for the samples with 20 sec and 40 sec recess etches under Schottky contact.
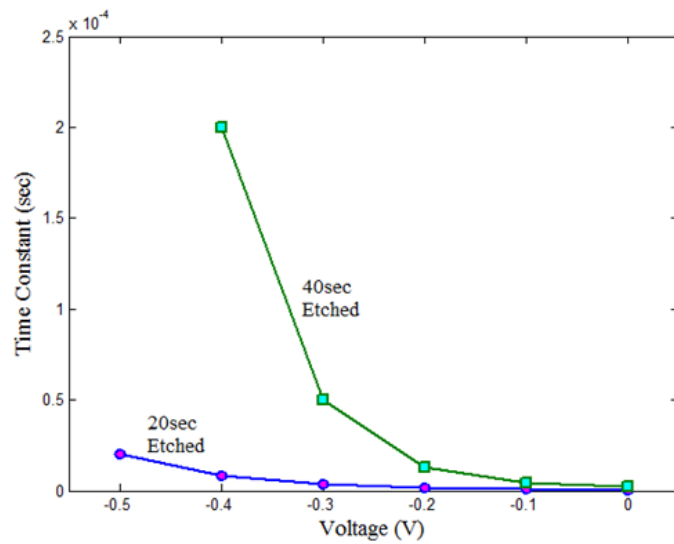
Figure 56. Trap state time constant versus the applied voltage for the samples with 20 sec and 40 sec recess etches under Schottky contact.

76

As shown in these figures, the sample with 20 sec recess etch exhibits a larger trap density and lower trap state time constant at a fixed voltage compared to the sample with 40 sec recess etch. Figure 56 demonstrates that the trap state time constant is an exponential function of the applied bias (i.e. the trap state energy). This exponential relationship between the trap state time constant and trap state energy is written as [74, 75]

$$\tau_T = (\sigma_T N_c v_t)^{-1} \exp(\frac{E_T}{kT}) , \qquad (35)$$

where σ_T is the trap state's capture cross-section, N_c is the density of states in the conduction band, v_t is the carriers' average thermal velocity, E_T is the trap state energy, k is the Boltzmann constant and T is the temperature. Considering $N_c = 4.3e14*T^{3/2}$, $\sigma_T = 3.4e\text{-}15$ cm^2 and $v_t = 2.6e7$ cm/s [74, 75], the trap state energy can be calculated from Eq.35. Figure 57Figure 57 illustrates the trap density versus the trap state energy below the conduction band for both samples.

Formatted: Font: 12 pt
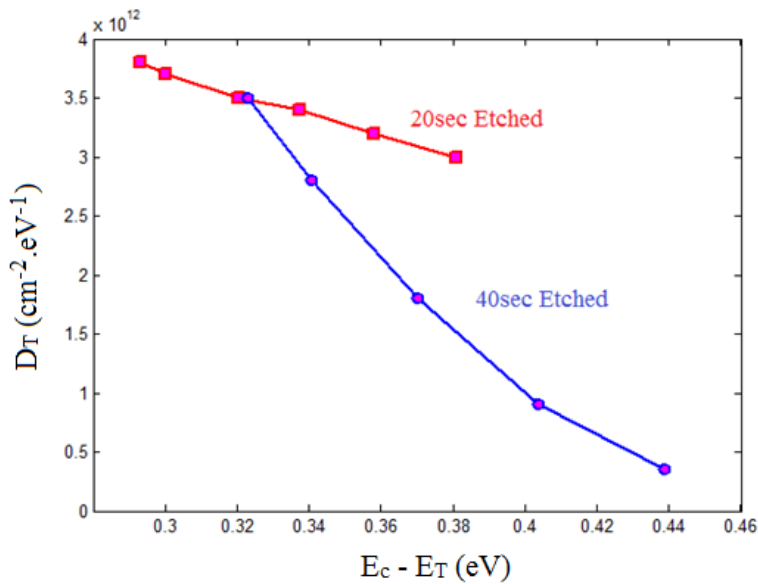
Figure 57. The trap density versus the trap state energy below the conduction band for the samples with 20 sec and 40 sec recess etches under Schottky contact.

As shown in this figure, the dry etch with the implemented recipe does not have a significant effect on the density of traps with energy states closer to the AlGaN conduction band. The states that are closer to the conduction band of AlGaN are the ones that contribute to the gate leakage current when the device is ON. Therefore, it is important to implement a dry etch recipe that does not change the density of these traps significantly.

Current mechanisms in recess-etched AlGaN/GaN SBDs

In AlGaN/GaN SBDs, several mechanisms can contribute to the total current of the Schottky junction. In SBDs with large AlGaN thicknesses, the forward current is dominated by the hole injection from the metal into the valence band of GaN due to the ionization of interface states [78]. The metal Fermi level is moved down toward the valence band of AlGaN at the positive bias, getting aligned with the valence band edge of GaN [78]. Therefore, the electrons in valence band of GaN are injected toward the metal which is equivalent to the hole injection from metal into the GaN. Figure 58 illustrates the band diagram of the AlGaN/GaN SBD under zero and positive biases [78].
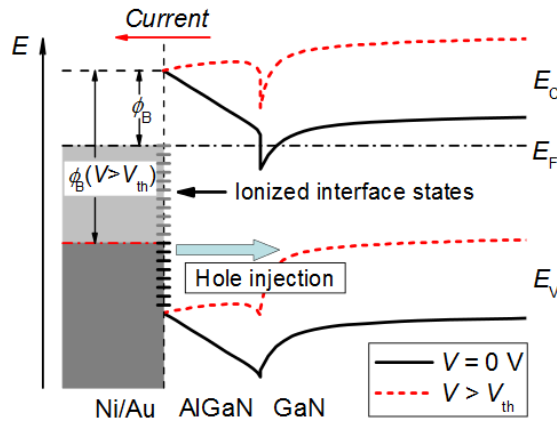
Figure 58. The band diagram of an AlGaN/GaN SBD under zero and positive biases [78].

Figure 59 illustrates the current voltage characteristics of an $Al_{0.3}Ga_{0.7}N/GaN$ SBD with an AlGaN thickness of 21.5 nm [79].
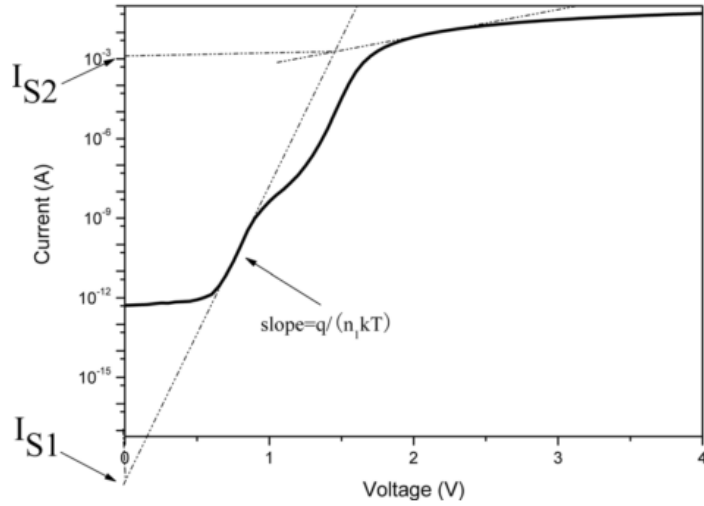
Figure 59. The forward bias current-voltage characteristic of an AlGaN/GaN SBD with an Al mole fraction of 0.3 and an AlGaN thickness of 21.5 nm [~~82~~79].

Since the AlGaN is relatively thick with an Al mole fraction of 0.3, the magnitude of electron tunneling current is negligible at lower biases due to the wide tunneling barrier. (In very large positive biases, however, the Fowler-Nordheim electron tunneling can contribute to the current due to smaller tunneling width which will be described later). Therefore, hole injection is the major current mechanism in this device. The amount of this current can be calculated through the following set of formula:

$$I_d = I_{S1} \exp[qV_1 / n_1 kT) - 1],$$ (36)

$$I_d = I_{S2} \exp[qV_2 / n_2 kT) - 1],$$ (37)

$$V_d = V_1 + V_2,$$ (38)

80

$$I_{S1} / S = A^* T^2 \exp(-q\phi_b / kT) \text{ and} \tag{39}$$

$$A^* = 4\pi q m^* k^2 / h^3 . \tag{40}$$

Here, S is the area of the Schottky contact and A^* is the effective Richardson constant, ϕ_b is the Ni-AlGaN barrier height, k is the Boltzmann constant, h is Plank constant, T is temperature, V_d is the voltage across the diode and I_d is the current flowing through the diode. I_{s1} and n_1 can be obtained from the intercept of the tangent line with y-axis and the slope of this line as shown in Figure 59. In our samples, however, the AlGaN is much thinner (8 nm and 14 nm for 40 sec and 20 sec etched samples respectively). Therefore electron tunneling currents can also contribute to the total current. In this case, the ideality factor, n_1, can not be obtained from the slope of the tangent line as illustrated in Figure 59 and the electron currents need to be taken into account.

In order to investigate the current mechanisms in the fabricated SBDs, the current-voltage characteristics of samples were measured using the HP 4145B semiconductor parameter analyzer. Figure 60 shows the I-V characteristics of both samples in linear y-axis scale.
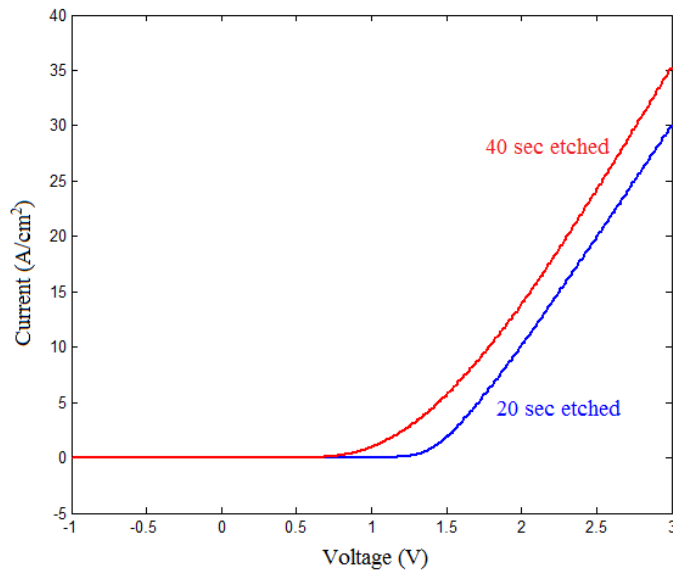
Figure 60. The current-voltage characteristics of SBDs with 20 sec and 40 sec recess etches under Schottky contact.

The turn ON voltage of the 20 sec etched sample is higher than the one for 40 sec etched sample due to the thicker AlGaN layer of 20 sec etched sample. Moreover, the 40 sec etched sample exhibits a larger ON state current due to the contribution of electron currents. Figure 61 illustrates the current-voltage characteristics of the sample in logarithmic y-axis scale, showing that the 20 sec etched sample has a lower OFF state leakage current.
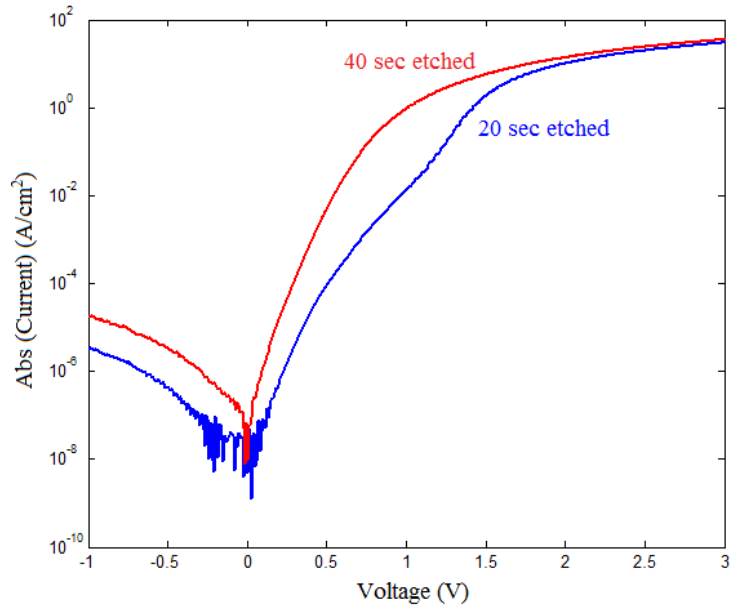
Figure 61. The logarithmic y-axis current-voltage characteristics of SBDs with 20 sec and 40 sec recess etches under Schottky contact.

The lower OFF state leakage current in 20 sec etched sample is due to the longer tunneling width because of the thicker AlGaN layer. As shown in this figure, the I-V characteristics start to deviate from the shape shown in Figure 59. However, for the 20 sec etched sample where the AlGaN thickness is 14 nm, a local drop in the current can still be seen in the plot. This shows that the electron current is still lower compared to the hole currents, meaning that the effect of electron tunneling is negligible at lower biases. Therefore, the Ni-AlGaN barrier height, ϕ_b, can be extracted by obtaining I_{S1} as shown in Figure 62 and using Eq.39.
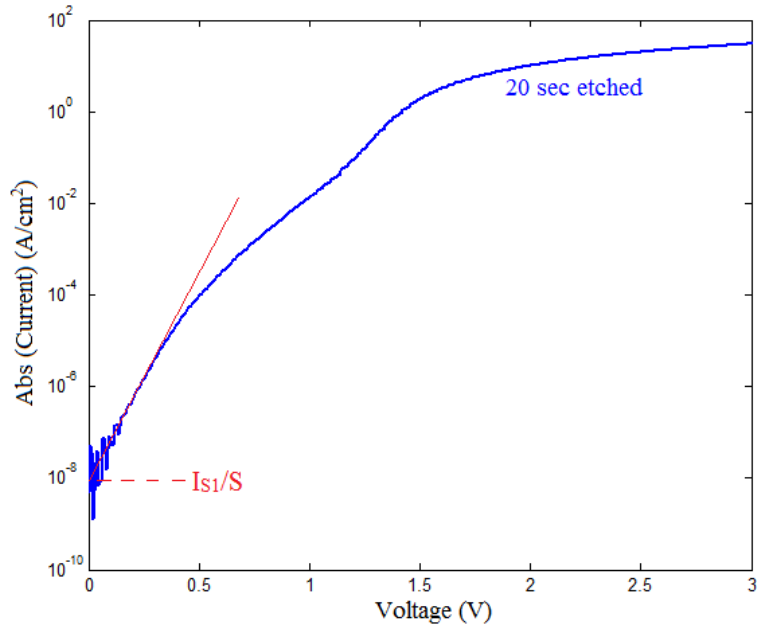
Figure 62. The logarithmic y-axis current-voltage characteristics of the SBD with 20 sec recess etch under Schottky contact and the way to extract I_{S1}/S value.

This leads to a ϕ_b value of 0.84 eV in our device. Knowing the conduction band offset at AlGaN/GaN interface through Eq.19 (ΔE_C) and the thickness of AlGaN layer (t_{AlGaN}), the zero-bias electric field in AlGaN is calculated as $E_{AlGaN} = (\phi_b - \Delta E_C) / t_{AlGaN}$.

The contribution of electron current increases by decreasing the thickness of the AlGaN layer. Figure 63 shows the conduction band diagram of an AlGaN/GaN SBD under the Schottky contact at different positive biases.
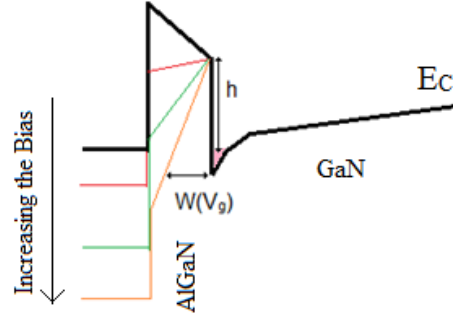
Figure 63. The conduction band diagram of the AlGaN/GaN SBD under the Schottky contact at different positive biases.

Several electron current mechanisms can be realized in AlGaN/GaN SBDs: Fowler-Nordheim (FN) Tunneling, Poole-Frenkle (PF) emission, Trap Assisted Tunneling (TAT) and Direct Tunneling (DT) [80].

For sufficiently large positive biases, the conduction band edge at AlGaN/metal interface gets aligned with the 2DEG or it lies below the GaN conduction band edge at AlGaN/GaN interface (Figure 63). In this case, the electrons from the 2DEG experience a triangular barrier and they can directly tunnel to the conduction band of AlGaN through a process called Fowler-Nordheim (FN) tunneling. The Fowler-Nordheim tunneling current density is written as [80]

$$J_{FN} = \frac{q^2}{8\pi h \phi_s} E_{AlGaN}^2 \exp[-\frac{8\pi\sqrt{2m^*q}}{3hE_{AlGaN}} \phi_B^{3/2})], \qquad (41)$$

in which ϕ_B is the barrier height at the emitting interface and m^* is the effective mass of the tunneling electron in AlGaN. Therefore, the linear portions of the $Ln(I/E^2_{AlGaN})$

versus $1/E_{AlGaN}$ are the regions where the total current is dominated by Fowler-Nordheim tunneling process.

To find the regions where the total current is dominated by Fowler-Nordheim mechanism, $Ln(I/E^2_{AlGaN})$ is sketched versus $1/E_{AlGaN}$ (Figure 64).
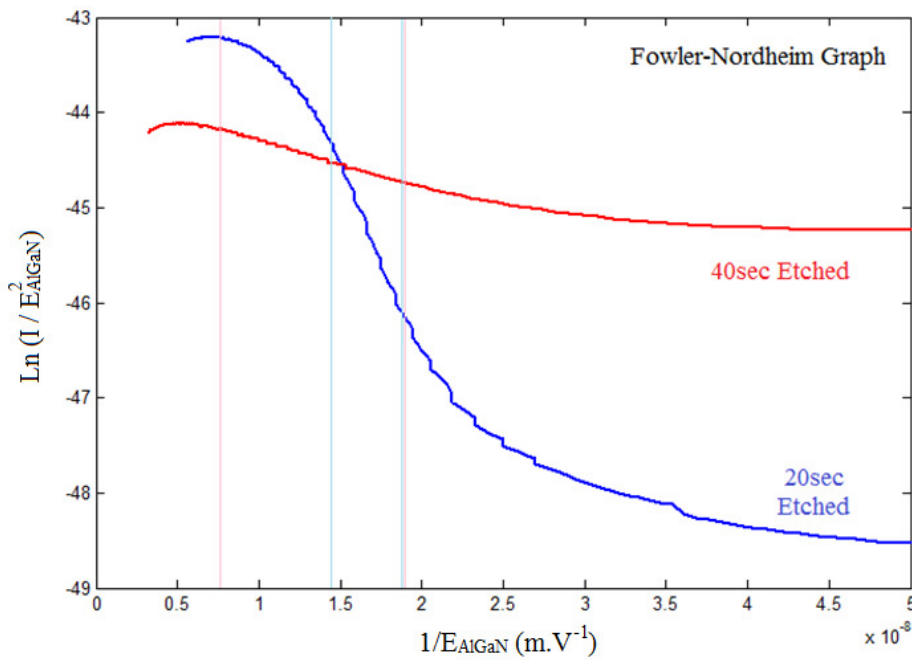
Figure 64. The plot of $Ln(I/E^2_{AlGaN})$ versus the $1/E_{AlGaN}$ for SBDs with 20 sec and 40 sec recess etches under Schottky contact to find the regions where the total current is dominated by Fowler-Nordheim tunneling process.

From Eq.41, it is inferred that the total current in regions of these plots that are linear and have the following slope are dominated by Fowler-Nordheim tunneling mechanism:

$$FN_{Slope} = -\frac{8\pi\sqrt{2m^*q}}{3hE_{AlGaN}}\phi_B^{3/2}. \tag{42}$$

Here, ϕ_B is the tunneling barrier or the conduction band offset at AlGaN/GaN interface represented by Eq.19. Since the Al mole fraction is 0.26 in our sample, ϕ_B is equal to 0.34 eV, allowing for the slope of the tangent line slope to Fowler-Nordheim plots to be calculated. The regions of I-V characteristics that are dominated by Fowler-Nordheim tunneling process are calculated and sketched in Figure 65.
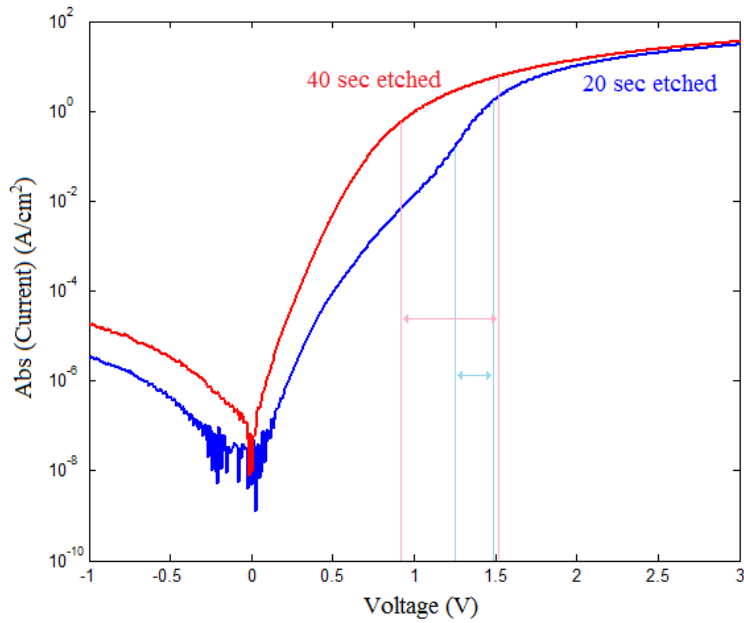
Figure 65. The logarithmic y-axis current-voltage characteristics of SBDs with 20 sec and 40 sec recess etches under Schottky contact and the regions where the total current is dominated by Fowler-Nordheim tunneling process.

As shown in this figure, the Fowler-Nordheim tunneling is dominant for a wider bias voltage range in 40 sec etched sample compared to the 20 sec etched sample. This is due to the thinner AlGaN layer of 40 sec etched sample which provides a shorter tunneling width, increasing the tunneling probability.

Poole-Frenkle emission of trapped electrons in AlGaN can also contribute to the total current [80]. The current due to Poole-Frenkle emission is proportional to [80]

$$J_{PF} \propto E_{AlGaN} \exp[-\frac{q}{kT}(\phi_t - \sqrt{qE_{AlGaN}/\pi\varepsilon_0\varepsilon_{AlGaN}})], \qquad (43)$$

in which ε_0 is the electric permittivity of vacuum and ε_{AlGaN} is the relative electric permittivity of AlGaN. Eq.43 implies that the linear portions of the plot of the $Ln(I/E_{AlGaN})$ versus $(E_{AlGaN})^{1/2}$ shows the regions where the total current is dominated by the Poole-Frenkle emission. The slope of the tangent line to find the regions where the total current is dominated by Poole-Frenkle emission is derived from Eq.43 as

$$PF_{Slope} = \frac{q}{kT}\sqrt{qE_{AlGaN}/\pi\varepsilon_0\varepsilon_{AlGaN}} . \qquad (44)$$

In order to find the regions where the total current is dominated by Poole-Frenkle emission, $Ln(1/E_{AlGaN})$ is sketched versus $E^{1/2}_{AlGaN}$ (Figure 66).
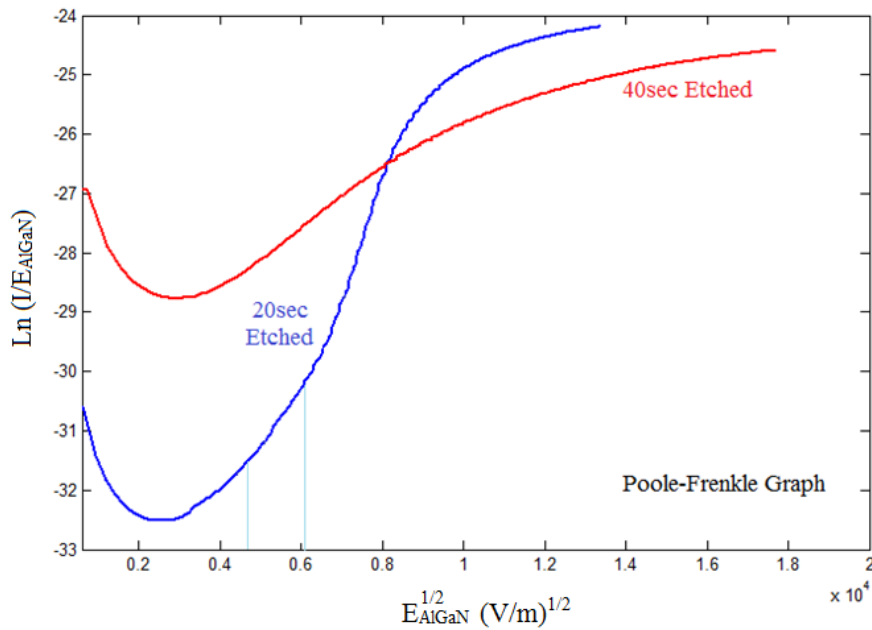
Figure 66. The plot of $Ln(I/E_{AlGaN})$ versus the square root of $E^{0.5}_{AlGaN}$ for SBDs with 20 sec and 40 sec recess etches under Schottky contact to find the regions where the total current is dominated Poole-Frenkle emission.

The 40 sec etched sample does not satisfy the slope requirement of Poole-Frenkle emission for positive biases and only the 20 sec etched sample satisfies the slope requirement.

From Figure 66, the voltage interval at which the total current is dominated by Poole-Frenkle emission is obtained as shown in Figure 67.
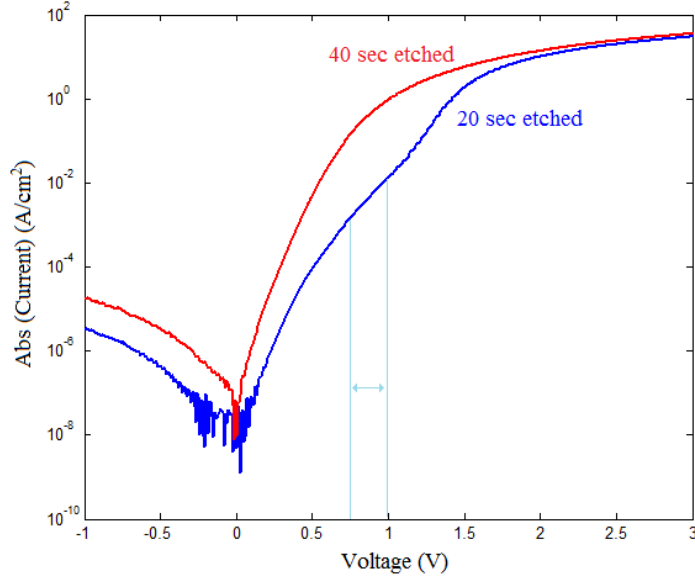
Figure 67. The logarithmic y-axis current-voltage characteristics of SBDs with 20 sec and 40 sec recess etches under Schottky contact and the region where the total current is dominated by Poole-Frenkle emission.

In addition to Poole-Frenkle emission and Fowler-Nordheim tunneling, there is the trap assisted tunneling which is a two-step tunneling process via traps in AlGaN. In this kind of tunneling, electrons from the 2DEG at AlGaN/GaN interface can tunnel into the traps in AlGaN at positive bias and then into the metal. The trap assisted tunneling current density is proportional to [80]

$$J_{TAT} \propto \exp(-\frac{8\pi\sqrt{2qm_{AlGaN}}}{3hE_{AlGaN}}\phi_t^{3/2}), \qquad (45)$$

where ϕ_t is the trap state energy, m_{AlGaN} is electron mass in AlGaN, h is the Plank constant, E_{AlGaN} is the electric field in AlGaN and q is the electron charge. The linear

90

portions of the plot of the *Ln(I)* versus *1/E$_{AlGaN}$* reflect the regions that the total current is dominated by trap assisted tunneling mechanism. The slope of the tangent line is derived from Eq.45 as

$$TAT_{Slope} = -\frac{8\pi\sqrt{2qm_{AlGaN}}}{3h}\phi_t^{3/2}. \tag{46}$$

In our sample, the trap state energy, ϕ_t, is varying as illustrated in Figure 57, providing various allowed TAT slopes. Figure 68 illustrates the plot of *Ln(I)* versus *1/E$_{AlGaN}$*.
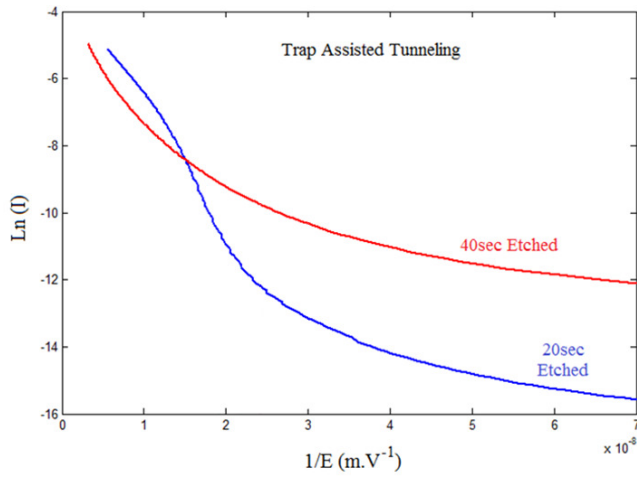
Figure 68. The plot of *Ln(I)* versus *1/E$_{AlGaN}$* for SBDs with 20 sec and 40 sec recess etches under Schottky contact to find the regions where the total current is dominated by trap-assisted tunneling process.

Since there are different allowed slopes for TAT graph, it is not possible to determine the regions dominated by this tunneling mechanism. Therefore, different current mechanisms for both samples are determined as illustrated in Figure 69.

91
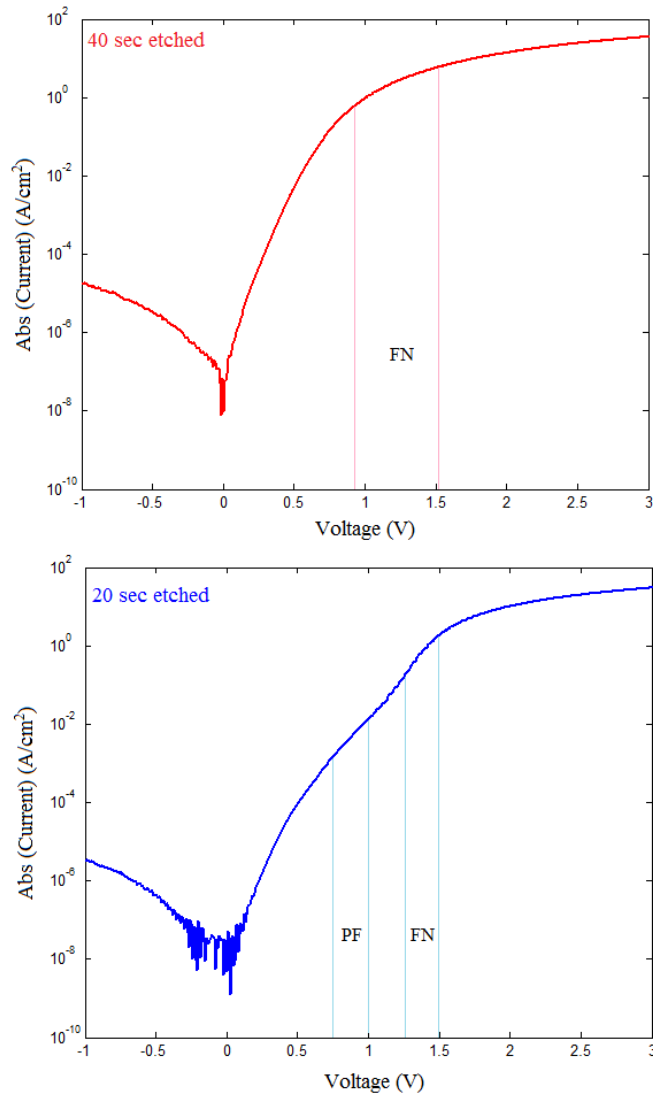
Figure 69. The logarithmic y-axis current-voltage characteristics of SBDs with 20 sec and 40 sec recess etches under Schottky contact and the regions where the total current is dominated by Fowler-Nordheim tunneling and Poole-Frenkle emission.

92

As illustrated in this figure, for the sample with thinner AlGaN (40 sec etched), the Fowler-Nordheim tunneling starts to get dominant at a lower bias. This is due to the shorter tunneling width of 40 sec etched sample which increases the tunneling probability. The current mechanisms in the negative regime have not been investigated because applying a negative bias partially or totally depletes the 2DEG underneath the Schottky contact. Therefore, it can not be assumed that the applied bias drops entirely across the AlGaN and there is a voltage drop across the depletion region that needs to be taken into account.

The Fowler-Nordheim tunneling process that has been characterized in both samples is occurring at the ON state of TMOSHFET. This is because the gate is positively biased at the ON state. Therefore, structure optimization to increase the amount of this current enhances the device switch ON speed and improves the device performance. This can be done by appropriate selection of AlGaN thickness and Al mole fraction underneath the gate.

CHAPTER VI

SUMMARY

In this dissertation, the Structure of Tunnel MOS Heterostructure FET (TMOSHFET) is introduced and its operation is analyzed. A model is developed to design the source and drain regions of AlGaN/GaN HEMTs and TMOSHFET taking into account the polarization electric fields and surface passivation effects. This model is verified by non-contact Hall 2DEG measurements of fabricated samples.

To form the source and drain contacts of TMOSHFET, the Ti/Al/Ni/Au Ohmic contacts to GaN are demonstrated and their current-voltage characteristics are characterized. A dry etching recipe to recess the gate region of TMOSHFET is implemented and its impacts on AlGaN trap density and time constant are characterized.

To understand different current mechanisms in the gate region of TMOSHFET, AlGaN/GaN Schottky Barrier Diodes (SBDs) with different recess etches under the Schottky contact are fabricated and their I-V plots are characterized.

REFERENCES

1. Burnham, S.D., et al., *Reliability of T-gate AlGaN/GaN HEMTs.* Physica Status Solidi (c), 2011. **8**(7-8): p. 2399-2403.

2. Gillespie, J., et al., *AlGaN/GaN ohmic contact resistance variations across epitaxial suppliers.* Solid-State Electronics, 2005. **49**(4): p. 670-672.

3. Ambacher, O., et al., *Two-dimensional electron gases induced by spontaneous and piezoelectric polarization charges in N- and Ga-face AlGaN/GaN heterostructures.* Journal of Applied Physics, 1999. **85**(6): p. 3222-3233.

4. Zhang, N., *High voltage GaN HEMTs with low on-resistance for switching applications.* PhD Dissertation UCSB, Santa Barbara, CA, 2006, p. 2.

5. Tipirneni, N., et al., *The 1.6-kV AlGaN/GaN HFETs.* Electron Device Letters, IEEE, 2006. **27**(9): p. 716-718.

6. Kao, T.T., et al., *2.5-ampere AlGaN/GaN HFETs on Si substrates with breakdown voltage >1,250V.* Proceedings of CS MANTECH Conference, Indian Wells, CA, 2011.

7. Zhang, N.Q., et al., *Kilovolt AlGaN/GaN HEMTs as switching devices.* Physica Status Solidi (a), 2001. **188**(1): p. 213-217.

8. Tipirneni, N., et al., *Silicon dioxide-encapsulated high-voltage AlGaN/GaN HFETs for power-switching applications.* Electron Device Letters, IEEE, 2007. **28**(9): p. 784-786.

9. Srivastava, P., et al., *Silicon substrate removal of GaN DHFETs for enhanced (<1100 V) breakdown voltage.* Electron Device Letters, IEEE, 2010. **31**(8): p. 851-853.

10. Bin, L. and T. Palacios, *High Breakdown (>1500V) AlGaN/GaN HEMTs by substrate-transfer technology.* Electron Device Letters, IEEE, 2010. **31**(9): p. 951-953.

11. Ikeda, N., et al. *High-power AlGaN/GaN MIS-HFETs with field-plates on Si substrates*. in Power Semiconductor Devices & IC's, 2009. ISPSD 2009. 21st International Symposium on., Barcelona, Spain, 2009: p. 251-254.

12. Arulkumaran, S., et al., *Improved ~~Power~~ power ~~Device~~ device ~~Figure~~figure-of-~~Merit~~merit (4.0×102 V^2.Ohms^{-1} cm^2) in AlGaN/GaN ~~High~~high-~~Electron~~electron-~~Mobility~~mobility ~~Transistors~~transistors on ~~High~~high-~~Resistivity~~resistivity 4-in. Si.* Appl. Phys. Express, 2011. **4**(8): p. 084101.

13. Huang, W., et al. *Lateral Implanted RESURF GaN MOSFETs with BV up to 2.5 kV*. in *Power Semiconductor Devices and IC's, 2008. ISPSD '08. 20th International Symposium on.*, Orlando, FL, 2008: p. 291-294.

14. Kuraguchi, M., et al., *High breakdown voltage AlGaN/GaN MIS-HFET with low leakage current.* ~~physica~~ Physica ~~status~~ Status ~~solidi~~ Solidi (c), 2005. **2**(7): p. 2647-2650.

15. Hikita, M., et al. *350V/150A AlGaN/GaN power HFET on silicon substrate with source-via grounding (SVG) structure*. in Electron Devices Meeting, 2004. IEDM Technical Digest. IEEE International., San Francisco, CA, 2004: p. 803-806.

16. Uemoto, Y., et al., *Recent advances of high voltage AlGaN/GaN power HFETs.* Proceedings of SPIE, San Jose, CA, 2009: p. 721606-721606.

17. Kuzmík, J., *InAlN/(In)GaN high electron mobility transistors: some aspects of the quantum well heterostructure proposal.* Semiconductor Science and Technology, 2002. **17**(6): p. 540.

18. Roberts, J.C., et al., *AlGaN ~~Transition~~ transition ~~Layers~~ layers on Si (111) ~~Substrates~~ substrates - ~~Observations~~observations of ~~Microstructure~~ microstructure and ~~Impact~~ impact on ~~Material~~ material ~~Quality~~quality.* MRS Online Proceedings Library, 2008. **1068**.

19. Ibbetson, J.P., et al., *Polarization effects, surface states, and the source of electrons in AlGaN/GaN heterostructure field effect transistors.* Applied Physics Letters, 2000. **77**(2): p. 250-252.

20. Smorchkova, I.P., et al., *Polarization-induced charge and electron mobility in AlGaN/GaN heterostructures grown by plasma-assisted molecular-beam epitaxy.* Journal of Applied Physics, 1999. **86**(8): p. 4520-4526.

21.   Lee, K.S., et al., *Self-consistent subband calculations of AlGaN/GaN single heterojunctions.* ETRI Journal, 2002. **24**: p. 270-279.

22.   Shi, C., P.M. Asbeck, and E.T. Yu, *Piezoelectric polarization associated with dislocations in wurtzite GaN.* Applied Physics Letters, 1999. **74**(4): p. 573-575.

23.   Ambacher, O., et al., *Two dimensional electron gases induced by spontaneous and piezoelectric polarization in undoped and doped AlGaN/GaN heterostructures.* Journal of Applied Physics, 2000. **87**(1): p. 334-344.

24.   Arulkumaran, S., et al., *Electrical characteristics of AlGaN/GaN HEMTs on 4-in diameter sapphire substrate.* Electron Device Letters, IEEE, 2003. **24**(8): p. 497-499.

25.   Aust, M.V., et al. *A ~~High~~ high ~~Efficiency~~ efficiency and ~~High~~ high ~~Linearity~~ linearity 20 GHz InP HBT ~~Monolithic~~ monolithic ~~Power~~ power ~~Amplifier~~ amplifier for ~~Phased~~ phased ~~Array~~ array ~~Applications~~applications.* in Microwave Symposium, 2007. IEEE/MTT-S International.~~,~~ Honolulu, HI, 2007: p. 809-812.

26.   Bae, C., et al., *Surface passivation of n-GaN by nitrided-thin-Ga_2O_3/SiO_2 and Si_3N_4 films.* Journal of Applied Physics, 2004. **96**(5): p. 2674-2680.

27.   Asbeck, P.M., et al., *Enhancement of base conductivity via the piezoelectric effect in AlGaN/GaN HBTs.* Solid-State Electronics, 2000. **44**(2): p. 211-219.

28.   Asbeck, P.M., et al., *Piezoelectric charge densities in AlGaN/GaN HFETs.* Electronics Letters, 1997. **33**(14): p. 1230-1231.

29.   Matthews, J.W. and A.E. Blakeslee, *Defects in epitaxial multilayers: III. Preparation of almost perfect multilayers.* Journal of Crystal Growth, 1976. **32**(2): p. 265-273.

30.   Bernardini, F., V. Fiorentini, and D. Vanderbilt, *Spontaneous polarization and piezoelectric constants of III-V nitrides.* Physical Review B, 1997. **56**(16): p. R10024-R10027.

31.   Suzuki, N. and N. Iizuka, *Effect of ~~Polarization~~ polarization ~~Field~~ field on ~~Intersubband~~ intersubband ~~Transition~~ transition in AlGaN/GaN ~~Quantum~~ quantum ~~Wells~~wells.* Jpn. J. Appl. Phys., 1999. **38**(Part 2, No. 4A): p. L363.

97

32. Park, S.-H. and S.-L. Chuang, *Spontaneous polarization effects in wurtzite GaN/AlGaN quantum wells and comparison with experiment.* Applied Physics Letters, 2000. **76**(15): p. 1981-1983.

33. Leroux, M., et al., *Barrier-width dependence of group-III nitrides quantum-well transition energies.* Physical Review B, 1999. **60**(3): p. 1496-1499.

34. Shealy, J.R., et al., *Growth and passivation of AlGaN/GaN heterostructures.* Journal of Crystal Growth, 2003. **250**(1–2): p. 7-13.

35. Prunty, T.R., et al. *Passivation of AlGaN/GaN heterostructures with silicon nitride for insulated gate transistors.* in High Performance Devices, 2000. Proceedings. 2000 IEEE/Cornell Conference on., Ithaca, NY, 2000: p. 208-214.

36. Byung-Hwan, C., et al., *Wireless ~~Detection~~ detection ~~System~~ system for ~~Glucose~~ glucose and pH ~~Sensing~~ sensing in ~~Exhaled~~ exhaled ~~Breath~~ breath ~~Condensate~~ condensate ~~Using~~ using AlGaN/GaN ~~High~~ high ~~Electron~~ electron ~~Mobility~~ mobility ~~Transistors~~ transistors.* Sensors Journal, IEEE, 2010. **10**(1): p. 64-70.

37. Chang, C.Y., et al., *CO2 detection using polyethylenimine/starch functionalized AlGaN/GaN high electron mobility transistors.* Applied Physics Letters, 2008. **92**(23): p. 232102-3.

38. Fitch, R., et al., *Effect of ~~Silicon~~ silicon ~~Nitride~~ nitride PECVD ~~Growth~~ growth on AlGaN/GaN HEMT ~~Dispersion~~ dispersion and ~~Breakdown~~ breakdown ~~Characteristics~~ characteristics.* Electrochemical Society Proceedings. **2004-6**: p. 459-465.

39. Karoutaa, F., et al., *Influence of the structural and compositional properties of PECVD silicon nitride layers on the passivation of AlGaN/GaN HEMTs.* ECS Transactions, 2008. **16**(7): p. 181-191.

40. Liu, Z.H., G.I. Ng, and S. Arulkumaran, *Mechanism of ~~Increased~~ increased ~~High~~ high-~~Frequency~~ frequency ~~Channel~~ channel ~~Noise~~ noise ~~With~~ with PECVD SiN ~~Passivation~~ passivation in AlGaN/GaN HEMTs.* Electron Device Letters, IEEE, 2009. **30**(11): p. 1122-1124.

41. Gatabi, I.R., et al., *PECVD ~~Silicon~~ silicon ~~Nitride~~ nitride ~~Passivation~~ passivation of AlGaN/GaN ~~Heterostructures~~ heterostructures.* Electron Devices, IEEE Transactions on, 2013. **60**(3): p. 1082-1087.

Formatted: Font: Not Italic

98

42.   Yu, L.S., et al., *Ni and Ti Schottky barriers on n-AlGaN grown on SiC substrates.* Applied Physics Letters, 1998. **73**(2): p. 238-240.

43.   Martin, G., et al., *Valence-band discontinuity between GaN and AlN measured by x-ray photoemission spectroscopy.* Applied Physics Letters, 1994. **65**(5): p. 610-612.

44.   Martin, G., et al., *Valence-band discontinuities of wurtzite GaN, AlN, and InN heterojunctions measured by x-ray photoemission spectroscopy.* Applied Physics Letters, 1996. **68**(18): p. 2541-2543.

45.   Asgari, A., M. Kalafi, and L. Faraone, *A quasi-two-dimensional charge transport model of AlGaN/GaN high electron mobility transistors (HEMTs).* Physica E: Low-dimensional Systems and Nanostructures, 2005. **28**(4): p. 491-499.

46.   Kudrawiec, R., et al., *Electromodulation spectroscopy of optical transitions and electric field distribution in GaN/AlGaN/GaN transistor heterostructures with various AlGaN layer thicknesses.* ~~physica~~ Physica ~~status~~ Status ~~solidi~~ Solidi (c), 2012. **9**(3-4): p. 1092-1095.

47.   Gladysiewicz, M. and R. Kudrawiec, *Distribution of built-in electric field in GaN(cap)/AlGaN/GaN(buffer) transistor heterostructures with various AlGaN thicknesses.* ~~physica~~ Physica ~~status~~ Status ~~solidi~~ Solidi (c), 2012. **9**(3-4): p. 883-886.

48.   Arulkumaran, S., G.I. Ng, and Z.H. Liu, *Effect of gate-source and gate-drain Si3N4 passivation on current collapse in AlGaN/GaN high-electron-mobility transistors on silicon.* Applied Physics Letters, 2007. **90**(17): p. 173504-3.

49.   Arulkumaran, S., et al., *Sheet carrier density enhancement by Si_3N_4 passivation on nonpolar a-plane (112-0) sapphire grown AlGaN/GaN heterostructures.* Applied Physics Letters, 2008. **92**(9): p. 092116-3.

50.   Wu, Y.Q., et al., *Photo-assisted capacitance-voltage characterization of high-quality atomic-layer-deposited Al_2O_3/GaN metal-oxide-semiconductor structures.* Applied Physics Letters, 2007. **90**(14): p. 143504-3.

51.   Ostermaier, C., et al., *Interface characterization of ALD deposited Al_2O_3 on GaN by CV method.* ~~physica~~ Physica ~~status~~ Status ~~solidi~~ Solidi (c), 2008. **5**(6): p. 1992-1994.

99

52.   Perez-Tomas, A., et al., *GaN metal-oxide-semiconductor field-effect transistor inversion channel mobility modeling.* Journal of Applied Physics, 2009. **105**(11): p. 114510-6.

53.   Baliga, B.J., *Semiconductors for high-voltage, vertical channel field-effect transistors.* Journal of Applied Physics, 1982. **53**(3): p. 1759-1764.

54.   Baliga, B.J., *Power semiconductor device figure of merit for high-frequency applications.* Electron Device Letters, IEEE, 1989. **10**(10): p. 455-457.

55.   Ikeda, N., et al., *GaN ~~Power~~ power ~~Transistors~~ transistors on Si ~~Substrates~~ substrates for ~~sS~~witching ~~Applications~~applications.* Proceedings of the IEEE, 2010. **98**(7): p. 1151-1161.

56.   Alekseev, E. and D. Pavlidis, *DC and high-frequency performance of AlGaN/GaN Heterojunction Bipolar Transistors.* Solid-State Electronics, 2000. **44**(2): p. 245-252.

57.   Piprek, J., *Nitride semiconductor devices: principles and simulations.* Wiley Publications, San Francisco, CA, 2007: Chapter 10, p. 222-224.

58.   Green, B.M., et al., *The effect of surface passivation on the microwave characteristics of undoped AlGaN/GaN HEMTs.* Electron Device Letters, IEEE, 2000. **21**(6): p. 268-270.

59.   Chung, S.K., *Analytic model for field-plate-edge breakdown of planar devices terminated with field plate and semiresistive layer.* Science, Measurement and Technology, IEE Proceedings -, 2004. **151**(1): p. 21-24.

60.   Saito, W., et al., *Influence of surface defect charge at AlGaN-GaN-HEMT upon Schottky gate leakage current and breakdown voltage.* Electron Devices, IEEE Transactions on, 2005. **52**(2): p. 159-164.

61.   Nishikawa, A., et al., *Critical electric fields of AlGaN in AlGaN-based vertical conducting diodes on -SiC substrates.* Superlattices and Microstructures, 2006. **40**(4–6): p. 332-337.

62.   Charfeddine, M., et al., *2-D theoretical model for current-voltage characteristics in AlGaN/GaN HEMT's.* Journal of Modern Physics, 2012. **3**: p. 881-886.

63.   Karmalkar, S. and U.K. Mishra, *Enhancement of breakdown voltage in AlGaN/GaN high electron mobility transistors using a field plate.* Electron Devices, IEEE Transactions on, 2001. **48**(8): p. 1515-1521.

64.   Palankovski, V., S. Vitanov, and R. Quay. *Field-~~Plate~~ plate ~~Optimization~~ optimization of AlGaN/GaN HEMTs.* in Compound Semiconductor Integrated Circuit Symposium, 2006. CSIC 2006. IEEE., San Antonio, TX, 2006: p. 107-110.

65.   Benbakhti, B., M. Rousseau, and J.C. De Jaeger. *Study of Field Plate AlGaN/GaN HEMTs by Means of a 2D-Hyrdynamic Model for Power Applications.* in *European Microwave Integrated Circuits Conference, 2006. The 1st.*, Manchester, UK, 2006: p. 363-366.

66.   Qin, Z.X., et al., *Study of Ti/Au, Ti/Al/Au, and Ti/Al/Ni/Au ohmic contacts to n-GaN.* Applied Physics A, 2004. **78**(5): p. 729-731.

67.   Papanicolaou, N.A., et al., *Reliable Ti/Al and Ti/Al/Ni/Au ohmic contacts to n-type GaN formed by vacuum annealing.* Journal of Vacuum Science & Technology B: Microelectronics and Nanometer Structures, 2001. **19**(1): p. 261-267.

68.   Jacobs, B., et al., *Optimisation of the Ti/Al/Ni/Au ohmic contact on AlGaN/GaN FET structures.* Journal of Crystal Growth, 2002. **241**(1–2): p. 15-18.

69.   Xin, H.P., et al., *Optimization of AlGaN/GaN HEMT ~~Ohmic~~ ohmic contacts for improved surface morphology with low contact resistance.* Proc. of CS MANTECH Conference, Portland, OR, 2010: p. 149-152.

70.   Sreenidhi, T., et al., *Reactive ion etching of GaN in $SF_6 + Ar$ and $SF_6 + N_2$ plasma.* Semiconductor Science and Technology, 2008. **23**(12): p. 125019.

71.   Cheung, R., et al., *Etch mechanism and etch-induced effects in the inductively coupled plasma etching of GaN.* Journal of Vacuum Science & Technology B: Microelectronics and Nanometer Structures, 2003. **21**(4): p. 1268-1272.

72.   Rong, B., et al. *Inductively coupled plasma etching of GaN and its effect on electrical characteristics.* Journal of Vacuum Science & Technology B: Microelectronics and Nanometer Structures, 2001. **19**(6): p. 2917-2920.~~2001. Washington, DC (USA): AVS~~.

73.   Basak, D., et al., *Reactive ion etching of GaN layers using SF₆.* Semiconductor
       Science and Technology, 1997. **12**(12): p. 1654.

74.   Stoklas, R., et al., *Investigation of trapping effects in AlGaN/GaN/Si field-effect
       transistors by frequency dependent capacitance and conductance analysis.*
       Applied Physics Letters, 2008. **93**(12): p. 124103-3.

75.   Kordos, P., et al., *Characterization of AlGaN/GaN metal-oxide-semiconductor
       field-effect transistors by frequency dependent conductance analysis.* Applied
       Physics Letters, 2009. **94**(22): p. 223512-3.

76.   Huang, W., T. Khan, and T. Paul Chow, *Comparison of MOS capacitors on n-
       and p-type GaN.* Journal of Electronic Materials, 2006. **35**(4): p. 726-732.

77.   Schroder, D.K., *Semiconductor material and device characterization.* Wiley
       Publications, San Francisco, CA, 2006: Chapter 6, p. 310-387.

78.   Li, B.K., et al., *Electroluminescence from a forward biased Ni/Au–AlGaN/GaN
       Schottky diode: evidence of Fermi level de-pinning at Ni/AlGaN interface.*
       physica Physica status Status solidi Solidi (c), 2010. **7**(7-8): p. 1961-1963.

79.   Lv, Y., et al., *Extraction of AlGaN/GaN heterostructure Schottky diode barrier
       heights from forward current-voltage characteristics.* Journal of Applied
       Physics, 2011. **109**(7): p. 074512-6.

80.   Chen, C.H., et al., *A new and simple model for GaAs heterojunction FET gate
       characteristics.* Electron Devices, IEEE Transactions on, 1988. **35**(5): p. 570-
       577.

103
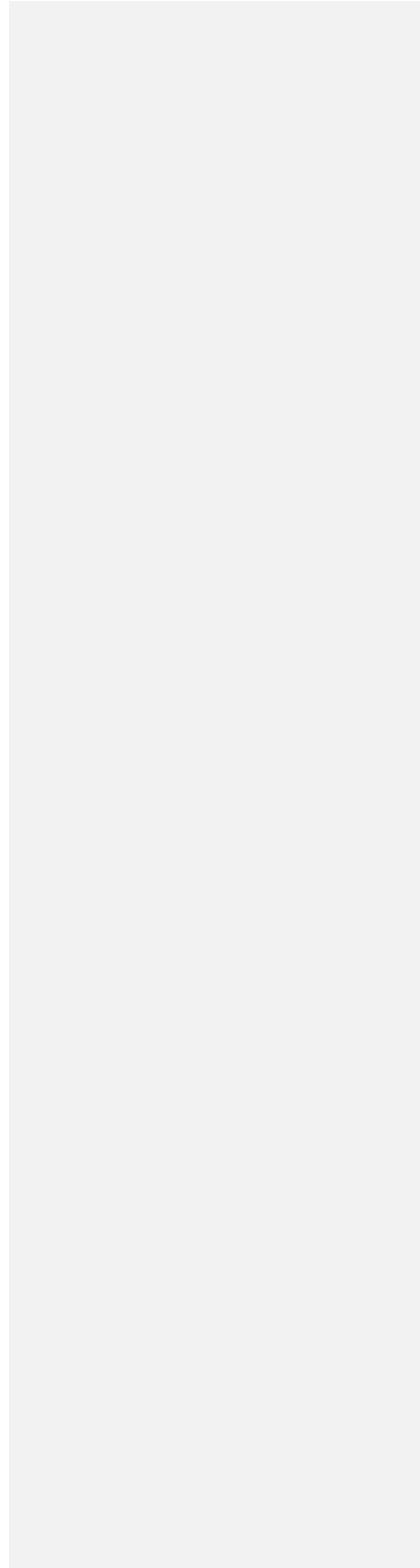
APPENDIX A

SENTAURUS MATERIAL PARAMETER FILE USED IN SIMULATIONS

Following material parameters are from the Synopsys-Sentaurus example files which are used in our simulations.

Material = "GaN" {

*************************** Dielectric Constant: *************************
Epsilon
{ * Ratio of the permittivities of material and vacuum

 * epsilon() = epsilon
      epsilon = 9.5
}

Epsilon_aniso
{ * Ratio of the permittivities of material and vacuum

 * epsilon() = epsilon
      epsilon = 10.4 # [1]
}

*************************** Lattice Heat Capacity: ***********************
LatticeHeatCapacity
{ * lumped electron-hole-lattice heat capacity
 * cv() = cv + cv_b * T + cv_c * T^2 + cv_d * T^3
      cv   = 3.0   # [J/(K cm^3)]
      cv_b   = 0.0000e+00   # [J/(K^2 cm^3)]
      cv_c   = 0.0000e+00   # [J/(K^3 cm^3)]
      cv_d   = 0.0000e+00   # [J/(K^4 cm^3)]
}

*************************** Thermal Conductivity: *************
Kappa
{ * Lattice thermal conductivity

 Formula = 1
 * Formula = 1:
 * kappa() = kappa + kappa_b * T + kappa_c * T^2
      kappa = 1.3   # [W/(K cm)]
      kappa_b   = 0.0000e+00   # [W/(K^2 cm)]
      kappa_c   = 0.0000e+00   # [W/(K^3 cm)]
                          104

}

************************** Hydro Parameters ***************
EnergyRelaxationTime
{ * Energy relaxation times in picoseconds
        Formula(tau_w)_ele = 3
        Spline(tau_w)_ele {
            0.0535   0.02921
            0.0600   0.02927
            0.0824   0.02941
            0.102   0.03051
            0.124   0.03179
            0.155   0.03533
            0.203   0.04224
            0.267   0.05133
            0.362   0.06543
            0.467   0.07951
            0.672   0.10620
            0.974   0.13855
            1.222   0.15871
            1.400   0.16764
            1.538   0.16912
            1.625   0.16697
            1.740   0.15494
            1.820   0.14296
            1.880   0.13077
            1.932   0.11952
            1.965   0.10944
            1.980   0.10027
            2.000   0.09286
            2.100   0.04000
            2.200   0.02000
            2.300   0.01200
            2.400   0.00800
            2.500   0.00600
        }
        (tau_w)_hol   = 0.2   # [ps]
}

EnergyFlux
{ * Coefficient in front of the energy flux equation
  * energy_flux_coef=0.6 corresponds to Stratton model
        energy_flux_coef_ele = 0.6   # [1]

105

```
        energy_flux_coef_hol = 0.6    # [1]
}


ThermalDiffusion
{ *  Thermal diffusion factor (0 <= td <= 1)
 *  td=0. corresponds to Stratton model
        td_n    = 0.0000e+00  # [1]
        td_p    = 0.0000e+00  # [1]
}


HeatFlux
{ *  Heat flux factor (0 <= hf <= 1)
 * Heat flux plays some role in the vertical reach of hot carriers.
 * The values of hf below are NOT calibrated
        hf_n    = 1.0    # [1]
        hf_p    = 1.0    # [1]
}


AvalancheFactors
{ *  Coefficientss for avalanche generation with hydro
 *  Factors n_l_f, p_l_f for energy relaxation length in the expressions
 *  for effective electric field for avalanche generation
 *  eEeff = eEeff / n_l_f  ( or b = b*n_l_f )
 *  hEeff = hEeff / p_l_f  ( or b = b*p_l_f )
 *  Additional coefficients n_gamma, p_gamma, n_delta, p_delta
        n_l_f   = 0.8                        # [1]
        p_l_f   = 0.8                        # [1]
        n_gamma     = 0.0000e+00             # [1]
        p_gamma     = 0.0000e+00             # [1]
        n_delta= 0.0000e+00              # [1]
        p_delta= 0.0000e+00              # [1]
}


*************************** Bandgap ********************************
Bandgap
{ * Eg = Eg0 + alpha Tpar2 / (beta + Tpar) - alpha T2 / (beta + T)
 * Parameter 'Tpar' specifies the value of lattice
 * temperature, at which parameters below are defined
 * Chi0 is electron affinity.
        Chi0    = 3.4                       # [eV]
        Bgn2Chi     = 0.5                       # [1]
        Eg0     = 3.47                      # [eV]
        alpha   = 7.40e-04                  # [eV K^-1]
        beta    = 6.00e+02                  # [K]
```

```
        Tpar    = 0.0000e+00                          # [K]
}


eDOSMass
{
 * For effective mass specificatition Formula1 (me approximation):
 * or Formula2 (Nc300) can be used :
        Formula      = 2      # [1]
 * Formula2:
 * me/m0 = (Nc300/2.540e19)2/3
 * Nc(T) = Nc300 * (T/300)3/2
        Nc300 = 2.65e18                          # [cm-3]
 * mass=0.222*mo
}

hDOSMass
{
 * For effective mass specificatition Formula1 (mh approximation):
 * or Formula2 (Nv300) can be used :
        Formula      = 2      # [1]
 * Formula2:
 * mh/m0 = (Nv300/2.540e19)2/3
 * Nv(T) = Nv300 * (T/300)3/2
        Nv300 = 2.5e19                          # [cm-3]
 *mass=1.0*mo
}

*************************** Mobility Models: *************************
* mu_lowfield^(-1) = mu_dop(mu_max)^(-1) + mu_Enorm^(-1) + mu_cc^(-1)
* Variable = electron value ,   hole value      # [units]
********************************************************************
ConstantMobility:
{ * mu_const = mumax (T/T0)^(-Exponent)
        mumax= 1200 ,       2.0000e+01            # [cm2/(Vs)]
        Exponent     = 1 ,   2.1                  # [1]
}

DopingDependence:
{
 * For doping dependent mobility model three formulas
 * can be used. Formula1 is based on Masetti et al. approximation.
 * Formula2 uses approximation, suggested by Arora.
        formula      = 1 ,   1                              # [1]
```

* If formula=1, model suggested by Masetti et al. is used:
* mu_dop = mumin1 exp(-Pc/N) + (mu_const - mumin2)/(1+(N/Cr)^alpha)
*   - mu1/(1+(Cs/N)^beta)
* with mu_const from ConstantMobility
```
      mumin1     = 85,   33                          # [cm2/Vs]
      mumin2     = 75,   0.00E+00                    # [cm2/Vs]
      mu1   = 50,   20                        # [cm2/Vs]
      Pc    = 6.50E+15,   5.00E+15          # [cm3]
      Cr    = 9.50E+16,   8.00E+16          # [cm3]
      Cs    = 7.20E+19,   8.00E+20          # [cm3]
      alpha = 0.55,        0.55       # [1]
      beta  = 0.75,        0.7             # [1]
```

* If formula=2, model suggested by Arora is used:
***** Not Callibrated *****
***** Parameters Below are for InN *****
* mu_dop = muminA + mudA/(1.+(N/N00)^AA),
* where muminA=Ar_mumin*(T/T0)^Ar_alm; mudA = Ar_mud*(T/T0)^Ar_ald
* N is net doping
* N00=Ar_N0*(T/T0)^Ar_alN; AA = Ar_a*(T/T0)^Ar_ala
}

HighFieldDependence:
{ * Caughey-Thomas model:
 * mu_highfield = mu_lowfield / (1 + (mu_lowfield E / vsat)^beta)1/beta
 * beta = beta0 (T/T0)^betaexp.
```
      beta0   = 1.7 , 1.7                          # [1]
      betaexp       = 0.0000e+00 ,        0.0000e+00         # [1]
```

 * Smoothing parameter for HydroHighField Caughey-Thomas model:
 * if Tl < Tc < (1+K_dT)*Tl, then smoothing between low field mobility
 * and HydroHighField mobility is used.
```
      K_dT   = 0.01 ,0.01                     # [1]
```
 * Transferred-Electron Effect:
 * mu_highfield = (mu_lowfield+(vsat/E)*(E/E0_TrEf)4)/(1+(E/E0_TrEf)4)
```
      E0_TrEf       = 1.5000e+05 ,        1.5000e+05         # [1]
      Ksmooth_TrEf       = 1 ,    1                     # [1]
```

* For vsat either Formula1 or Formula2 can be used.
```
      Vsat_Formula = 2 ,    2                  # [1]
```
* Formula2 for saturation velocity:
*   vsat = A_vsat - B_vsat*(T/T0)
* (Parameter Vsat_Formula has to be equal to 2):

* Obs: experiments seem to confirm a lower vsat for the 2D electron gas than bulk
        A_vsat = 1.5e7 ,   2.1000e+07   # [1]
        B_vsat = 0 ,   0   # [1]
        vsat_min   = 5.000e+05 , 5.000e+05   # [1]
}

****************** Recombination/Generation Models: **********************
* Variable = electron value ,   hole value   # [unit]
****
Scharfetter * relation and trap level for SRH recombination:
{ * tau = taumin + (taumax - taumin) / (1 + (N/Nref)^gamma
  * tau(T) = tau * ((T/300)^Talpha)   (TempDep)
  * tau(T) = tau * exp(Tcoeff * ((T/300)-1)) (ExpTempDep)
        taumin = 0.0000e+00 ,   0.0000e+00   # [s]
        taumax= 1.0000e-9 , 1.0000e-9   # [s]
        Nref   = 1.0000e+16 ,   1.0000e+16   # [cm^(-3)]
        gamma= 1 ,   1   # [1]
        Talpha = -1.5000e+00 ,   -1.5000e+00   # [1]
        Tcoeff = 2.55 ,   2.55   # [1]
        Etrap   = 0.0000e+00   # [eV]
}

vanOverstraetendeMan * Impact Ionization:
{ * G_impact = alpha_n n v_drift_n + alpha_p p v_drift_p
  * with alpha = gamma a exp(-b gamma/E) for E<E0 (low) and E>E0 (high)
   * with gamma = tanh(hbarOmega/(2kT0)) / tanh(hbarOmega/(2kT))
        a(low) = 2.9e+08 ,   1.3400e+08   # [1/cm]
        a(high)= 2.9e+08 ,   1.3400e+08   # [1/cm]
        b(low) = 3.4e+07 ,   2.0300e+07   # [V/cm]
        b(high)= 3.4e+07 ,   2.0300e+07   # [V/cm]
        E0   = 4.0000e+05 ,   4.0000e+05   # [V/cm]
        hbarOmega   = 0.035 ,   0.035   # [eV]
}

QuantumPotentialParameters
{ * gamma: weighting factor for quantum potential
  * theta: weight for quadratic term
  * xi: weight for quasi Fermi potential
  * eta: weight for electrostatic potential
        gamma= 1.41, 5.6   # [1]
        theta = 0.5 , 0.5   # [1]
        xi   = 1 ,   1   # [1]
        eta   = 1 ,   1   # [1]
}

```
*****************************************************************
Auger * coefficients:
{ * R_Auger = ( C_n n + C_p p ) ( n p - ni_eff^2)
 * with C_n,p = (A + B (T/T0) + C (T/T0)^2) (1 + H exp(-{n,p}/N0))
      A      = 1.0000e-30 , 1.0000e-30    # [cm^6/s]
      B      = 0.0000e+00 ,        0.0000e+00    # [cm^6/s]
      C      = 0.0000e+00 ,        0.0000e+00    # [cm^6/s]
      H      = 0.0000e+00 ,        0.0000e+00    # [1]
      N0     = 1.0000e+18 ,        1.0000e+18    # [cm^(-3)]
}

RadiativeRecombination * coefficients:
{ * R_Radiative = C (n p - ni_eff^2)
      C       = 2.0000e-10   # [cm^3/s]
}
}

Material = "AlGaN" {
*  Mole dependent material: AlGaN (x=0) = GaN
*  Mole dependent material: AlGaN (x=1) = AlN

* Not calibrated.
* No values available in the literature
EnergyRelaxationTime
{ *  Energy relaxation times in picoseconds
      (tau_w)_ele    = 0.05          # [ps]
      (tau_w)_hol    = 0.1           # [ps]
}

EnergyFlux
{ *  Coefficient in front of the energy flux equation
 *  energy_flux_coef=0.6 corresponds to Stratton model
      energy_flux_coef_ele = 0.6   # [1]
      energy_flux_coef_hol = 0.6   # [1]
}

ThermalDiffusion
{ *  Thermal diffusion factor (0 <= td <= 1)
 *  td=0. corresponds to Stratton model
      td_n    = 0.0000e+00 # [1]
      td_p    = 0.0000e+00 # [1]
}
```

HeatFlux
{ * Heat flux factor (0 <= hf <= 1)
      hf_n   = 1.0   # [1]
      hf_p   = 1.0   # [1]
}

QuantumPotentialParameters
{ * gamma: weighting factor for quantum potential
  * theta: weight for quadratic term
  * xi: weight for quasi Fermi potential
  * eta: weight for electrostatic potential
      gamma= 1.9 , 5.6   # [1]
      theta = 0.5 , 0.5   # [1]
      xi   = 1 ,   1   # [1]
      eta   = 1 ,   1   # [1]
}

****
Scharfetter * relation and trap level for SRH recombination:
{ * tau = taumin + (taumax - taumin) / (1 + (N/Nref)^gamma)
  * tau(T) = tau * ((T/300)^Talpha)   (TempDep)
  * tau(T) = tau * exp(Tcoeff * ((T/300)-1)) (ExpTempDep)
      taumin = 0.0000e+00 ,   0.0000e+00   # [s]
      taumax= 1.0000e-09 , 1.0000e-09   # [s]
      Nref   = 1.0000e+16 ,   1.0000e+16   # [cm^(-3)]
      gamma= 1 ,   1   # [1]
      Talpha = 0.0000e+00 ,   0.0000e+00   # [1]
      Tcoeff = 0.0000e+00 ,   0.0000e+00   # [1]
      Etrap   = 0.0000e+00 # [eV]
}

Auger * coefficients:
{ * R_Auger = (C_n n + C_p p) (n p - ni_eff^2)
  * with C_n,p = (A + B (T/T0) + C (T/T0)^2) (1 + H exp(-{n,p}/N0))
      A   = 1.0000e-30 , 1.0000e-30   # [cm^6/s]
      B   = 0.0000e+00 ,   0.0000e+00   # [cm^6/s]
      C   = 0.0000e+00 ,   0.0000e+00   # [cm^6/s]
      H   = 0.0000e+00 ,   0.0000e+00   # [1]
      N0   = 1.0000e+18 ,   1.0000e+18   # [cm^(-3)]
}

RadiativeRecombination * coefficients:
{ * R_Radiative = C (n p - ni_eff^2)
      C   = 2.0000e-10   # [cm^3/s]

111

}
}
Material = "AlN" {

*************************** Dielectric Constant: *************************
Epsilon
{ * Ratio of the permittivities of material and vacuum

 * epsilon() = epsilon
      epsilon = 8.5   # [1]
}

Epsilon_aniso
{ * Ratio of the permittivities of material and vacuum

 * epsilon() = epsilon
      epsilon = 10.7   # [1]
}

*************************** Lattice Heat Capacity: *************************

LatticeHeatCapacity
{ * lumped electron-hole-lattice heat capacity
 * cv() = cv + cv_b * T + cv_c * T^2 + cv_d * T^3
      cv   = 1.94   # [J/(K cm^3)]
      cv_b   = 0.0000e+00   # [J/(K^2 cm^3)]
      cv_c   = 0.0000e+00   # [J/(K^3 cm^3)]
      cv_d   = 0.0000e+00   # [J/(K^4 cm^3)]
}

*************************** Thermal Conductivity: ***********************
Kappa
{ * Lattice thermal conductivity

 Formula = 1
 * Formula = 1:
 * kappa() = kappa + kappa_b * T + kappa_c * T^2
      kappa = 2.85   # [W/(K cm)]
      kappa_b   = 0.0000e+00   # [W/(K^2 cm)]
      kappa_c   = 0.0000e+00   # [W/(K^3 cm)]
}

**************************** Hydro Parameters ***********************
112

EnergyRelaxationTime
{ * Energy relaxation times in picoseconds
      (tau_w)_ele   = 0.05   # [ps]
      (tau_w)_hol   = 0.1   # [ps]

}

EnergyFlux
{ * Coefficient in front of the energy flux equation
  * energy_flux_coef=0.6 corresponds to Stratton model
      energy_flux_coef_ele = 0.6   # [1]
      energy_flux_coef_hol = 0.6   # [1]
}

ThermalDiffusion
{ * Thermal diffusion factor (0 <= td <= 1)
  * td=0. corresponds to Stratton model
      td_n   = 0.0000e+00 # [1]
      td_p   = 0.0000e+00 # [1]
}

HeatFlux
{ * Heat flux factor (0 <= hf <= 1)
      hf_n   = 0.5   # [1]
      hf_p   = 0.5   # [1]
}

AvalancheFactors
{ * Coefficientss for avalanche generation with hydro
  * Factors n_l_f, p_l_f for energy relaxation length in the expressions
  * for effective electric field for avalanche generation
  * eEeff = eEeff / n_l_f (or b = b*n_l_f)
  * hEeff = hEeff / p_l_f (or b = b*p_l_f)
  * Additional coefficients n_gamma, p_gamma, n_delta, p_delta
      n_l_f   = 0.8   # [1]
      p_l_f   = 0.8   # [1]
      n_gamma   = 0.0000e+00   # [1]
      p_gamma   = 0.0000e+00   # [1]
      n_delta= 0.0000e+00   # [1]
      p_delta= 0.0000e+00   # [1]
}

*************************** Bandgap *******************************
Bandgap

113

```
{ * Eg = Eg0 + alpha Tpar2 / (beta + Tpar) - alpha T2 / (beta + T)
 * Parameter 'Tpar' specifies the value of lattice
 * temperature, at which parameters below are defined
 * Chi0 is electron affinity.
        Chi0   = 1.9                        # [eV]
        Eg0    = 6.2                        # [eV]
        alpha  = 1.7900e-03                 # [eV K^-1]
        beta   = 1.4620e+03                 # [K]
        Tpar   = 3.0000e+02                 # [K]
}

eDOSMass
{
 * For effective mass specificatition Formula1 (me approximation):
 * or Formula2 (Nc300) can be used :
        Formula      = 2                         # [1]
 * Formula2:
 * me/m0 = (Nc300/2.540e19)2/3  = 0.3
 * Nc(T) = Nc300 * (T/300)3/2
        a       = 0.1905                    # [1]
        ml      = 0.9163                    # [1]
        mm      = 0.0000e+00                # [1]
        Nc300 = 4.10e18                     # [cm-3]
}

hDOSMass
{
 * For effective mass specificatition Formula1 (mh approximation):
 * or Formula2 (Nv300) can be used :
        Formula      = 2      # [1]
 * Formula2:
 * mh/m0 = (Nv300/2.540e19)2/3  ~= 5.0
 * Nv(T) = Nv300 * (T/300)3/2
        a       = 0.443587                  # [1]
        b       = 3.6095e-03                # [K^-1]
        c       = 1.1735e-04                # [K^-2]
        d       = 1.2632e-06                # [K^-3]
        e       = 3.0256e-09                # [K^-4]
        f       = 4.6834e-03                # [K^-1]
        g       = 2.2869e-04                # [K^-2]
        h       = 7.4693e-07                # [K^-3]
        i       = 1.7275e-09                # [K^-4]
        mm      = 0.0000e+00                # [1]
        Nv300 = 2.8400e+20                  # [cm-3]
```

}

*************************** Mobility Models: **************************
* mu_lowfield^(-1) = mu_dop(mu_max)^(-1) + mu_Enorm^(-1) + mu_cc^(-1)   *
* Variable = electron value ,   hole value   # [units]   *
****
****
ConstantMobility:
{ * mu_const = mumax (T/T0)^(-Exponent)
       Exponent   = 1,   2.1   #[1]
       mumax= 300, 14   #[cm2/(Vs)]
}

DopingDependence:
{
 * For doping dependent mobility model three formulas
 * can be used. Formula1 is based on Masetti et al. approximation.
 * Formula2 uses approximation, suggested by Arora.
       formula   = 1 ,   1   # [1]
 * If formula=1, model suggested by Masetti et al. is used:
 * mu_dop = mumin1 exp(-Pc/N) + (mu_const - mumin2)/(1+(N/Cr)^alpha)
 *   - mu1/(1+(Cs/N)^beta)
 * with mu_const from ConstantMobility
       mumin1   = 20,   11   # [cm2/Vs]
       mumin2   = 65,   0.00E+00   # [cm2/Vs]
       mu1   = 20,   10   # [cm2/Vs]
       Pc   = 8.00E+17, 5.00E+18   # [cm3]
       Cr   = 7.00E+16, 8.00E+17   # [cm3]
       Cs   = 5.20E+17, 8.00E+18   # [cm3]
       alpha = 0.88,   1.05   # [1]
       beta   = 0.75,   0.75   # [1]

 * If formula=2, model suggested by Arora is used:
 ***** Not Callibrated *****
 ***** Parameters Below are for InN *****
 * mu_dop = muminA + mudA/(1.+(N/N00)^AA),
 * where muminA=Ar_mumin*(T/T0)^Ar_alm; mudA = Ar_mud*(T/T0)^Ar_ald
 * N is net doping
 * N00=Ar_N0*(T/T0)^Ar_alN; AA = Ar_a*(T/T0)^Ar_ala
}

HighFieldDependence:

115

{ * Caughey-Thomas model:
 * mu_highfield = mu_lowfield / (1 + (mu_lowfield E / vsat)^beta)1/beta
 * beta = beta0 (T/T0)^betaexp.
       beta0   = 2,   2   #[1]
       betaexp   = 0.0000e+00, 0.0000e+00   #[1]

 * Smoothing parameter for HydroHighField Caughey-Thomas model:
 * if Tl < Tc < (1+K_dT)*Tl, then smoothing between low field mobility
 * and HydroHighField mobility is used.
       K_dT = 0.01, 0.01   # [1]
 * Transferred-Electron Effect:
 * mu_highfield = (mu_lowfield+(vsat/E)*(E/E0_TrEf)4)/(1+(E/E0_TrEf)4)
       E0_TrEf   = 2.7000e+05 ,   2.7000e+05   # [1]
       Ksmooth_TrEf   = 1 ,   1   # [1]

 * For vsat either Formula1 or Formula2 can be used.
       Vsat_Formula = 2 ,   2   # [1]
 * Formula2 for saturation velocity:
 *   vsat = A_vsat - B_vsat*(T/T0)
 * (Parameter Vsat_Formula has to be equal to 2):
       A_vsat = 1.5000e+07, 1.5000e+07   #[cm/s]
       B_vsat = 0,   0   #[cm/s]
       vsat_min   = 5.0000e+06, 5.0000e+06   #[cm/s]
}

***************** Recombination/Generation Models: **********************
* Variable = electron value , hole value   # [units]   *
****
Scharfetter * relation and trap level for SRH recombination:
{ * tau = taumin + (taumax - taumin) / (1 + (N/Nref)^gamma
 * tau(T) = tau * ((T/300)^Talpha)   (TempDep)
 * tau(T) = tau * exp(Tcoeff * ((T/300)-1)) (ExpTempDep)
       taumin = 0.0000e+00 ,   0.0000e+00   # [s]
       taumax= 1.0000e-9 , 1.0000e-9   # [s]
       Nref   = 1.0000e+16 ,   1.0000e+16   # [cm^(-3)]
       gamma= 1 ,   1   # [1]
       Talpha = -1.5000e+00 ,   -1.5000e+00   # [1]
       Tcoeff = 2.55 ,   2.55   # [1]
       Etrap   = 0.0000e+00   # [eV]
}

vanOverstraetendeMan * Impact Ionization:
{ * G_impact = alpha_n n v_drift_n + alpha_p p v_drift_p
 * with alpha = gamma a exp(-b gamma/E) for E<E0 (low) and E>E0 (high)
116

```
 *  with gamma = tanh(hbarOmega/(2kT0)) / tanh(hbarOmega/(2kT))
      a(low) = 2.9e8 ,        1.3400e+07              # [1/cm]
      a(high)= 2.9e8 ,        1.3400e+07              # [1/cm]
      b(low) = 3.4e8 ,        2.0300e+08              # [V/cm]
      b(high)= 3.4e8 ,        2.0300e+08              # [V/cm]
      E0     = 4.0000e+05, 4.0000e+05                 #[V/cm]
      hbarOmega     = 0.035,          0.035           #[V/cm]
}


*******************************************************************
*  Parameters for the recombination models below were taken
*  from GaAs and require calibration for accurate simulations
*******************************************************************
Auger * coefficients:
{ * R_Auger = ( C_n n + C_p p ) ( n p - ni_eff^2)
 * with C_n,p = (A + B (T/T0) + C (T/T0)^2) (1 + H exp(-{n,p}/N0))
      A       = 1.0000e-30 , 1.0000e-30    # [cm^6/s]
      B       = 0.0000e+00 ,        0.0000e+00    # [cm^6/s]
      C       = 0.0000e+00 ,        0.0000e+00    # [cm^6/s]
      H       = 0.0000e+00 ,        0.0000e+00    # [1]
      N0      = 1.0000e+18 ,        1.0000e+18    # [cm^(-3)]
}

RadiativeRecombination * coefficients:
{ * R_Radiative = C (n p - ni_eff^2)
      C       = 2.0000e-10   # [cm^3/s]
}


}
```

117

APPENDIX B

SAMPLE SENTAURUS INPUT FILE FOR ALGAN/GAN HEMT SIMULATION

```
Electrode {
        { Name="gate"   Voltage= 0 Schottky Workfunction=3.8}
        { Name="source" Voltage= 0 }
        { Name="drain"  Voltage= 0 }
}

File {
        Grid= "strd20l20_msh.tdr"
        Parameter= "models.par"
        Current= "n3_des.plt"
        Plot= "plotd20l20vg-1.9t2.4.tdr"
        Output= "n3_des.log"
}

Physics {
        Hydrodynamic(eTemperature)
        Mobility(
                DopingDependence
                eHighfieldsaturation(GradQuasiFermi)
        )
        EffectiveIntrinsicDensity (Nobandgapnarrowing)
        Fermi
        Recombination(SRH)
        RecGenHeat
        Aniso(Poisson)
}

Physics (Material="GaN") {
        Traps (
                (Acceptor Level Conc= 5e17 EnergyMid= 1.0 EnergySig= 0 \
                FromMidBandGap  eXSection= 1e-15 hXSection= 1e-15)
        )
}

Physics (Material="AlGaN") {
        Traps (
                (Acceptor Level Conc= 5e17 EnergyMid= 1.0 EnergySig= 0 \
                FromMidBandGap  eXSection= 1e-15 hXSection= 1e-15)
        )
        MoleFraction(XFraction=0.2)
```

118

```
}

Physics (MaterialInterface="AlGaN/GaN") {
        Charge(Conc=8.25e+12
* This is pspalgan+ppealgan-pspgan
)
}

Physics (MaterialInterface="AlGaN/Si3N4") {
        Charge(Conc=-2.64e13
* This is the summation of piezoelectric and spontaneous polarization of AlGaN
)
        Traps (
                (Donor Level Conc= 2.4e13 EnergyMid= 1 FromCondBand)
        )
}

Plot {
        Potential Electricfield/Vector
        eDensity hDensity
        eCurrent/Vector hCurrent/Vector
        TotalCurrent/Vector
        SRH Auger Avalanche
        eMobility hMobility
        eQuasiFermi hQuasiFermi
        eGradQuasiFermi hGradQuasiFermi
        eEparallel hEparallel
        eMobility hMobility
        eVelocity hVelocity
        DonorConcentration Acceptorconcentration
        Doping SpaceCharge
        ConductionBand ValenceBand
        BandGap Affinity
        xMoleFraction
        eTemperature hTemperature
        eTrappedCharge hTrappedCharge
}

Math {
        Extrapolate
        Iterations= 16
        Digits= 6
        ErrRef(electron) = 1E5
        ErrRef(hole) = 1E3
```

```
        RHSmin= 1e-10
        RHSmax= 1e30
        CDensityMin= 1e-20
        DirectCurrentComputation
        RelTermMinDensity= 1e5
        eMobilityAveraging= ElementEdge
}

Solve {
        Coupled (Iterations= 100000 LinesearchDamping= 0.001)  {Poisson}
        Coupled (Iterations= 100) {Poisson Electron Hole}

        ************************************************************
        Plot(FilePrefix="n4_Zero_Bias")

        ************************************************************
        NewCurrentFile="IdVg _"

NewCurrentFile="currente1d20x0.2l20t2.4"

 Quasistationary (
   InitialStep=0.1 Increment=1.35
   MaxStep=0.5 Minstep=1.e-5
   Goal { Name="gate" Voltage=-3.57}
 ){ Coupled { Poisson Electron Hole } }

 Quasistationary (
   InitialStep=0.1 Increment=1.6
   MaxStep=0.5 Minstep=1.e-5
   Goal { Name="drain" Voltage=350}
 ){ Coupled { Poisson Electron Hole } }

 Plot(FilePrefix="l20e1d20x0.2vd350vg-1.9t2.4e13")

}
```

APPENDIX C

IMAN REZANEZHAD GATABI- PUBLICATIONS

1- Gatabi, I.R., et al., *PECVD silicon nitride passivation of AlGaN/GaN heterostructures.* Electron Devices, IEEE Transactions on, 2013. **60**(3): p. 1082-1087.

2- Coan, M.R., et al., *Band offset measurement of GaN/dielectric interfaces.* Journal of Applied Physics, 2012. **112**: p. 024508.

3- Gatabi, I.R., et al., *Performance simulation of three dimensional nano-scale field effect diode.* Semiconductor Science and Technology, 2011. **26**: p. 045014.

4- Gatabi, J.R., et al., *Auxiliary fluid flowmeter.* European Journal of Scientific Research, 2010. **42**: p. 84-92.

5- Forouzbakhsh, F., et al., *A new measurement method for ultrasonic surface roughness measurement.* Measurement, 2009. **32**(5): p. 702-705.

6- Forouzbakhsh, F., et al., *Design considerations to enhance the modulation efficiency and cutoff frequency of AlGaN/InGaN/GaN HEMTs.* Proc. of 8th IEEE Int. Conf. on Design and Technology of Integrated Systems in Nanoscale Era, Abu Dhabi, UAE, 2013: p. 47-52.

7- Gatabi, I.R., et al., *Single-photon X-ray detector using AlGaN/GaN heterostructure.* Joint Fall 2012 Meeting of the Texas Sections of the American Physical Society, AAPT, and Zone 13 of the SPS, Lubbock, TX, 2012.

8- Woo, J.H., et al., *Energy efficient tunnel transistors using dielectric-gated band engineered tunnel junctions.* Joint Fall 2012 Meeting of the Texas Sections of the American Physical Society, AAPT, and Zone 13 of the SPS, Lubbock, TX, 2012.

9- Karaoglan, G., et al., *Photoluminescence investigation of oxidation on GaN.* Joint Fall 2012 Meeting of the Texas Sections of the American Physical Society, AAPT, and Zone 13 of the SPS, Lubbock, TX, 2012.

10- Purahmad, M., et al., *Design of an organic pixel addressing circuit for active-matrix OLED displays.* Proc. of ASME MicroNano 2008 Conference, Kowloon, Hong Kong, 2008: p. 727-730.

11- Sendi, M.S.E., et al., *Improved low voltage all cascode current source using the DC level shifter.* Proc. of 50th IEEE Midwest Symposium on Circuits & Systems, Montreal, Canada, 2007: p. 171-172.

12- Gatabi, J.R., et al., *A novel Doppler-based ultrasonic surface roughness measurement.* Proc. of 2005 IEEE Int. Ultrasonics Symposium, Rotterdam, Netherlands, 2005: p. 1460-1463.